UNIVERSITY OF ROCHESTER
LABORATORY FOR LASER ENERGETICS

Volume 63
April–June 1995
DOE/SF/19460-91

LLE Review

Quarterly Report

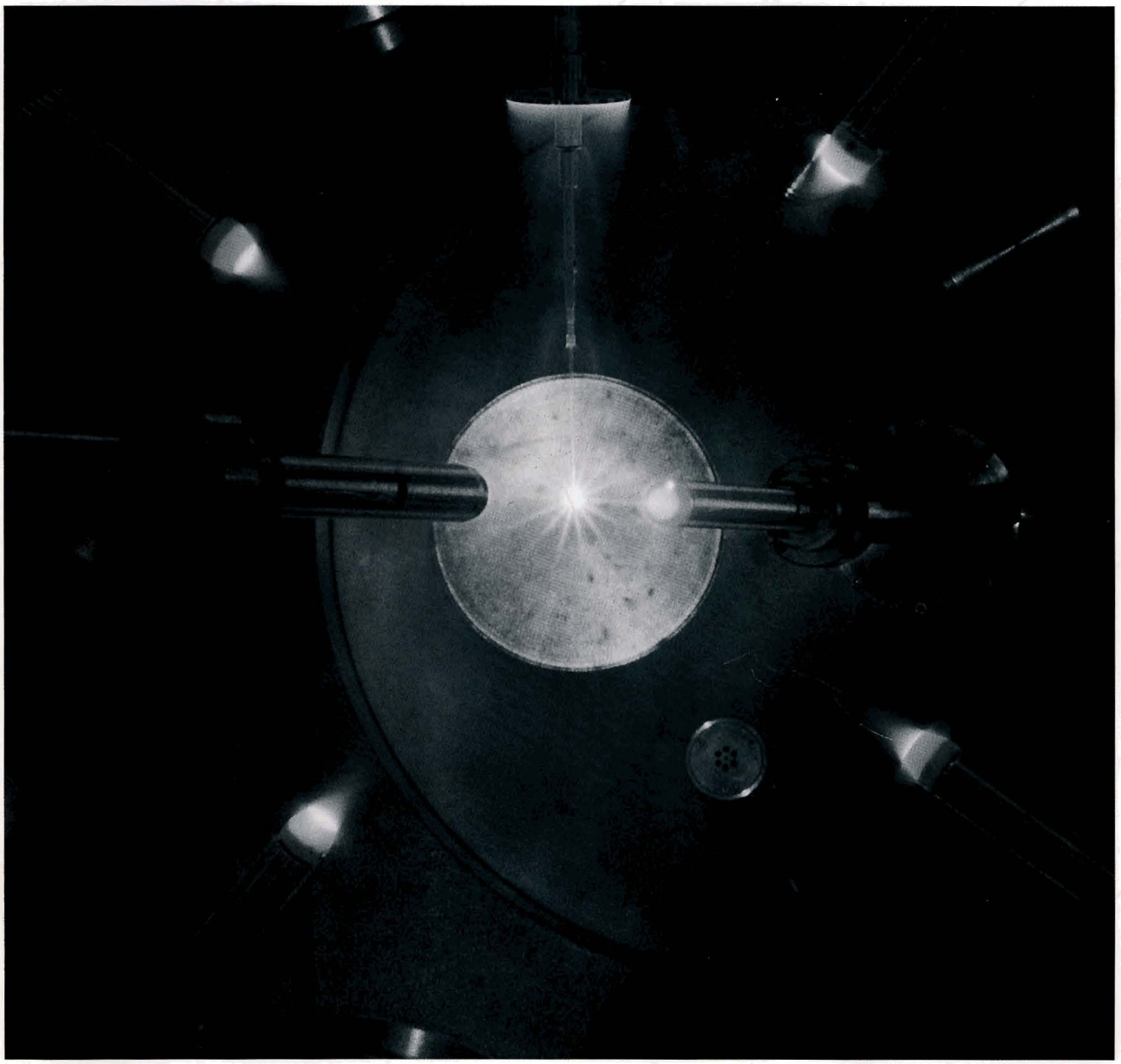

About the Cover:

The cover photograph shows the inside of the OMEGA target chamber during one of the first shots in which all 60 beams were used to irradiate a target. The photograph shows the target positioner (top) and the six pinhole cameras, identical and equidistant from the target, used to diagnose the beam positioning. The bright circle surrounding the target is a flange on the opposing diagnostic port illuminated with visible light from the target plasma. The diagnostic near 5 o'clock is a plasma calorimeter. This shot was one of a series used to demonstrate that the upgraded OMEGA system exceeded its performance goals.

The work described in this volume includes current research at the Laboratory for Laser Energetics, which is supported by New York State Energy Research and Development Authority, the University of Rochester, the U.S. Department of Energy Office of Inertial Confinement Fusion under Cooperative Agreement No. DE-FC03-92SF19460, and other agencies.

Printed in the United States of America
Available from

National Technical Information Services
U.S. Department of Commerce
5285 Port Royal Road
Springfield, VA 22161

Price codes: Printed Copy A04
Microfiche A01

For questions or comments, contact R. Stephen Craxton, Editor, Laboratory for Laser Energetics, 250 East River Road, Rochester, NY 14623-1299, (716) 275-5467.

UNIVERSITY OF ROCHESTER
LABORATORY FOR LASER ENERGETICS

Volume 63
April–June 1995
DOE/SF/19460-91

LLE Review

Quarterly Report

UR LLE

Contents

In Brief

This volume of the LLE Review, covering the period of April–June 1995, includes a description of the initial performance results of the upgraded OMEGA laser system. A series of acceptance tests were completed, demonstrating that all 60 beams can irradiate targets with more energy and better beam balance than was required by the Department of Energy's acceptance criteria. Other articles in this volume include a description of a novel energy measurement system used to diagnose all 60 OMEGA beams; a theoretical calculation of the cutoff wave number of the ablative Rayleigh-Taylor instability, applicable to both direct and indirect drive; a description of a new algorithm used for designing distributed phase plates that will produce super-Gaussian focal-plane irradiance profiles; a study of the photoresponse of high-T_c YBCO thin films; and a description of magnetorheological finishing, a new process for optics polishing.

Highlights of the research presented in this issue are

- The upgraded OMEGA laser system has irradiated targets with UV energies up to 37 kJ, a beam-to-beam energy balance better than 8%, and overall frequency-conversion efficiencies of 75%. The system performs as designed and in accordance with modeling.

- A novel beam-energy diagnostic system, based on optical fibers, has been implemented on OMEGA. It can measure the UV energy and the residual green and IR energies of all 60 beams with a relative, beam-to-beam accuracy of a fraction of a percent.

- A new analytic model is presented for calculating the cutoff wave number of the ablative Rayleigh-Taylor instability. This is valid for an arbitrary power-law dependence of the electron thermal conductivity and is applicable to both direct and indirect drive.

- A new algorithm is presented for designing phase plates that will produce nearly flat super-Gaussian irradiation distributions on target. These phase plates have continuous surfaces and thus minimize scattering losses.

- Electro-optic sampling has been used for the first time to study the photoresponse of YBCO thin films. Electrical transients as short as 1.5 ps have been observed and are the fastest photoresponse signals reported to date from YBCO thin films.

- A description is given of magnetorheological finishing, a new method for the finish polishing of optics in which the polishing is performed using a fluid suspension stiffened by a magnetic field. This method is being studied using a pre-prototype machine located at the Center for Optics Manufacturing.

R. Stephen Craxton
Editor

Initial Performance Results of the OMEGA Laser System

An important step in the U.S. inertial fusion effort toward demonstrating ignition and modest gain in the laboratory is the validation of high-performance direct-drive fusion capsules. The scientific program at UR/LLE[1] is aimed at studying near-ignition conditions in direct-drive capsules that achieve ion temperatures of 2 to 3 keV and fuel areal densities of 0.2 g/cm^2. Such capsules are expected to achieve convergence ratios greater than 20 and experience Rayleigh-Taylor (R-T) growth factors in excess of 500. The OMEGA laser system has been upgraded to demonstrate these near-ignition conditions. The system has now produced up to 37 kJ of UV energy on target in 60 beams. Ultimately, the system will provide versatile pulse shapes and produce high irradiation uniformity (1%–2%) on the capsule.

The preliminary design[2] for the upgraded OMEGA system was completed in October 1989. Detailed design commenced in October 1990. In December 1992, the 24-beam OMEGA laser fired its last shot before being decommissioned to allow for the construction of the upgraded system. Ten months later, the building modifications were completed and laser construction began. In January 1994, the pulse generation room (PGR) began operations, and, in April 1994, the entire driver was activated. The first full OMEGA beamline was completed in December 1994 and produced 800 J in the IR and 606 J in the UV. In February 1995, a single UV beam irradiated a target. In March, the first 60-beam laser shot was fired, and in April, all 60 beams irradiated a target. The final acceptance tests for the system were performed on 2 May 1995.

The acceptance criteria for the upgraded system were the demonstration of target irradiation with 30 kJ of UV energy in 60 beams with ~750-ps Gaussian pulses and the achievement of a beam-to-beam energy balance of 10% rms. This article provides a brief description of the laser system and then presents the initial system performance results that met and exceeded the acceptance criteria. Specifically, targets were irradiated with UV energies up to 37 kJ, and the beam-to-beam energy balance was better than 8%. Overall frequency-conversion efficiencies of 75% were routinely obtained. The full laser system was operated for 15 shots with a 1-h shot cycle, including nine consecutive target shots.

OMEGA is a Nd:glass laser in the master oscillator–power amplifier (MOPA) configuration (see Fig. 63.1). It uses rod amplifiers up to a beam diameter of 9 cm, followed by disk amplifiers up to an output aperture of 20 cm in the IR. Each amplifier is followed by a spatial filter. The 60 IR beams are expanded in the final spatial filters to a 28-cm aperture and converted to 351 nm using KDP crystals in the type II/type II polarization-mismatch frequency-tripling configuration developed at LLE.[3,4] The beams are uniformly distributed around a 3.3-m-diam target chamber and focused onto target with *f*/6 lenses. (The effective *f* number based on the beam diameter is approximately 6.7.) Details of the design and configuration of the laser system can be found in other LLE Review articles. In Ref. 5, an updated description of the system included design changes since the preliminary design.[2] More details were given in Ref. 6 (laser drivers and laser amplifiers), Ref. 7 (power conditioning, control systems, optomechanical systems, major structures, and the target area), Ref. 8 [the large-aperture ring amplifiers (LARA's)], and Ref. 9 (the final design review prepared for the Department of Energy). This article presents performance results for the driver, the power amplifiers, frequency conversion, the harmonic energy diagnostic system, the temporal laser pulse shape, and the target-bay alignment and pointing systems.

Driver

The OMEGA driver generates optical pulses that are amplified, frequency converted, and eventually irradiate the target. To provide precise control of the on-target irradiation for fusion experiments, the driver must provide a beam that is stable and appropriately shaped in space, time, and frequency. In the acceptance tests the amplitude stability of the OMEGA driver was demonstrated to be better than 2% rms.

Figure 63.2 depicts the configuration of the driver, which begins with a master oscillator that produces ~10-nJ, 80-ps Gaussian pulses at a rate of ~76 MHz. These pulses seed

feedback-stabilized regenerative amplifiers (regens), which produce ~0.5 mJ per pulse with a pulse width ranging from 0.5 ns to 5 ns. A pulse-shaping system, not yet implemented and not shown in Fig. 63.2, will temporally shape the master-oscillator pulses before injection into these regens. It will be possible to inject independent pulse shapes into each of the three regens (main pulse, foot pulse, and backlighter). For the acceptance tests described here, a Gaussian pulse of ~800-ps duration was produced using an etalon in the main-pulse regen. The pulse-shaping system and the foot-pulse and backlighter beams were not required.

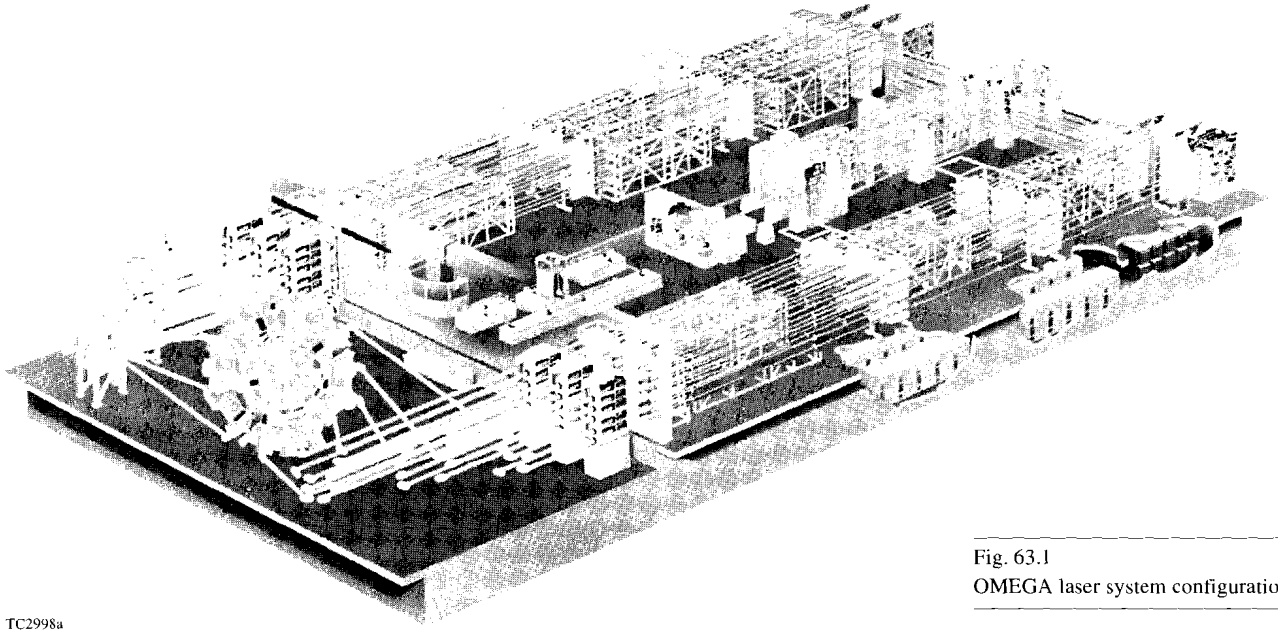

TC2998a

Fig. 63.1
OMEGA laser system configuration.

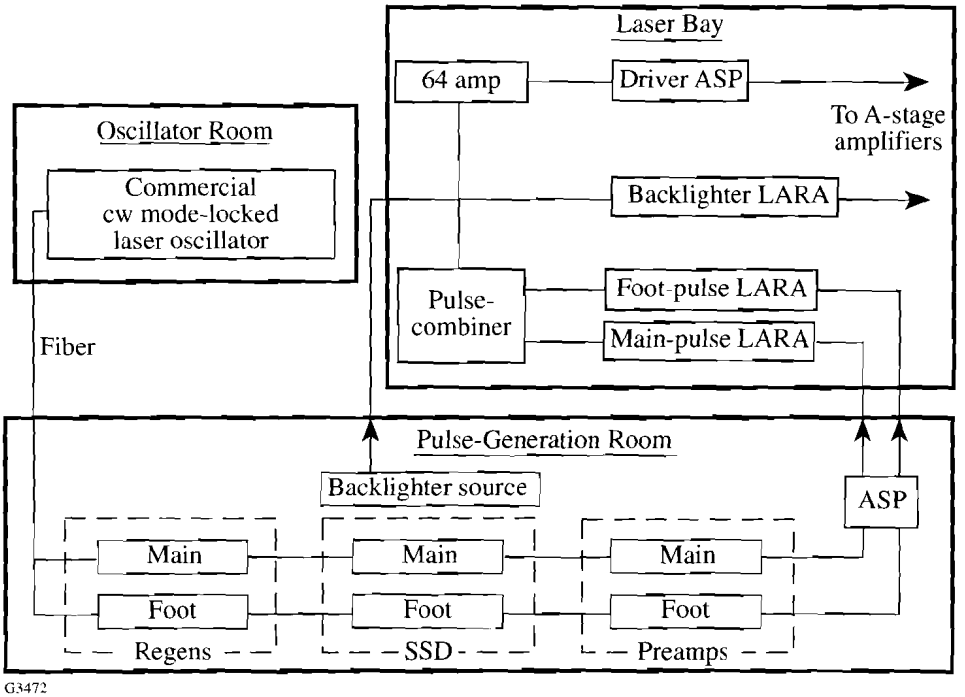

G3472

Fig. 63.2
Driver configuration for the OMEGA laser as used during the performance tests. Three optical pulses of independent temporal shapes (main, foot, and backlighter) can be generated in each of three separate drivers and subsequently amplified in three large-aperture ring amplifiers (LARA's).

The regens largely dictate the stability and reproducibility of the driver, which is why an amplitude feedback mechanism was implemented. This approach to stabilization has produced output pulses that have amplitudes and pulse widths with shot-to-shot variations of ≲1.5% rms. In addition, the time jitter between pulses from separate oscillators has been measured to be ≲30 ps rms. This low jitter permits the operation of synchronized oscillators for the main, foot, and backlighter pulses as well as ancillary oscillators/amplifiers to drive fiducials and probe beams needed for the diagnosis of fusion experiments. The wavelength of the pulses is monitored on every shot using Fabry-Perot interferometers that provide 0.05-Å wavelength resolution; care is taken to ensure that the wavelength remains constant to that accuracy so as not to compromise the frequency-conversion crystal (FCC) alignment.

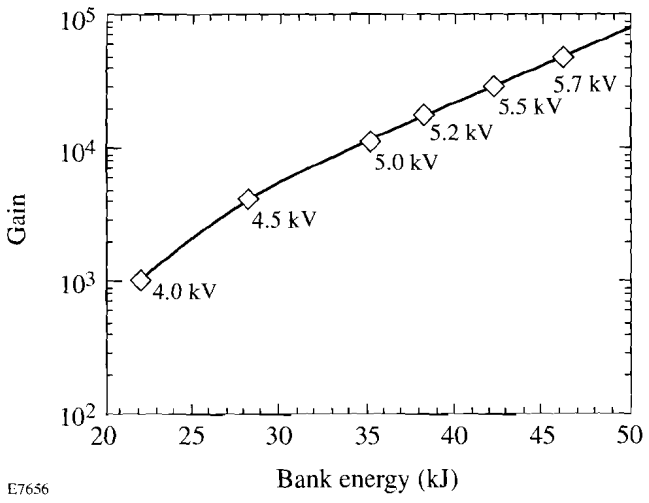

Fig. 63.3
Performance results for the main-pulse LARA. The gain is given as a function of bank energy for four-pass operation. The bank energy is determined from the charging voltage indicated.

To conserve space in the laser bay and enhance performance reliability, most of the driver gain is provided by a large-aperture ring amplifier (LARA). For the acceptance tests, LARA amplified the regen output from <1 mJ to ~1 J and a single-pass, 64-mm amplifier then amplified the pulse to ~5 J. LARA is a 40-mm, four-pass, imaging ring amplifier capable of producing energies ≳15 J in 1 ns. LARA is compact and fits easily on a 5-ft × 10-ft optical table. Figure 63.3 demonstrates the LARA gain performance in its four-pass configuration. Gains of up to ~4×10^4 have been achieved. This performance largely exceeds current requirements and thus ensures that schemes to improve the irradiation uniformity, which require additional driver gain, can be accommodated without compromising the full output-energy performance of the system. The high quality of the output beam from LARA is clearly demonstrated by the near-field image and interferogram (Fig. 63.4) obtained during tests at full aperture (37 mm) for a pulse width of ~1 ns. The peak-to-valley phase distortion [Fig. 63.4(b)] was measured to be less than one wave at $\lambda = 1$ μm, while random intensity fluctuations were ≲10% rms. Under normal operating conditions on OMEGA, only the ~20-mm central region of the LARA aperture is used, resulting in ≲$\lambda/4$ phase error (peak to valley). The slight edge enhancement of the near-field image is due to the input beam apodizer that was designed for a lower output energy.

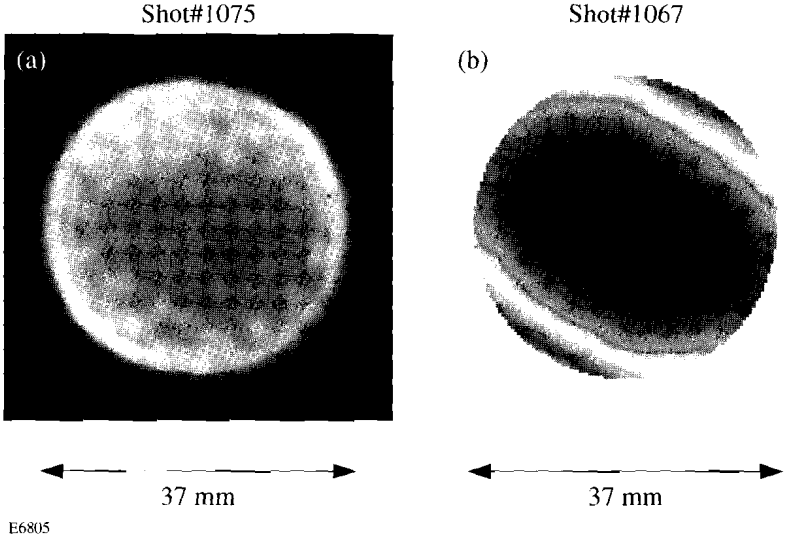

Fig. 63.4
(a) Near-field image and (b) interferogram of 37-mm-diam beams at the LARA output. The beam energy was 13.7 J in (a) and 17.8 J in (b).

The OMEGA driver is used to shape the output spatial profile of the laser (see Fig. 63.5). This is characterized by two features: the intensity profile and the location of the outer "edge" of the beam. (To maintain alignment and prevent modulations due to vignetting of the beam, an edge is needed to define the beam.) Each of these features is determined by the profile at an image plane in the driver that is relayed through the system by the spatial filters. To ensure high extraction efficiency in the disk amplifiers and high frequency-conversion efficiency, it is important that the output spatial profile of the laser be flat. The input beam profile must therefore compensate for the radial gain variation exhibited by the rod amplifiers of the system (stages A through D). This is done by placing a serrated apodizer[10] at the input to LARA and irradiating it with an appropriately sized beam from the PGR. Using a laser propagation code (*RAINBOW*) and the measured radial-gain profiles of each class of amplifier (40, 64, and 90 mm), the apodizer transmittance and input beam size have been designed to produce the desired beam intensity profile at the output of the system (the solid line of Fig. 63.5). For the tests reported here, the apodizer was used to shape the spatially Gaussian beam from the PGR. The beam edge is set entirely by the transmittance of the apodizer. The LARA spatial filter removes the high spatial frequencies created by the serrations while preserving the desired low-frequency beam shape. As a consequence, the pinhole in this filter is the tightest in the whole laser system—just five times the diffraction-limited size for its 2.0-cm beam.

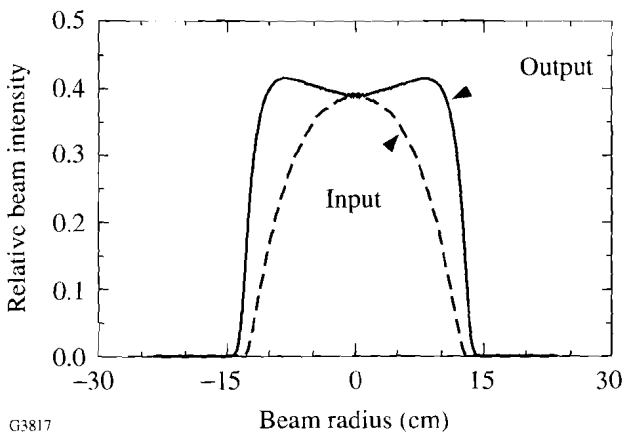

Fig.63.5
One-dimensional lineouts of the IR spatial intensity profile at the input to the amplifier chain (dashed line, scaled with the beamline paraxial magnification) and at the output of the final (stage-F) spatial filter (solid line). The input profile is strongly center-peaked to compensate for the radial gain profiles in the rod amplifiers.

Power Amplifiers

The OMEGA system has been designed to propagate the complex temporal pulse shapes required for direct-drive targets.[11] The system is staged for equivalent Gaussian pulse widths in the range of 0.5–3.0 ns. The 0.5-ns pulses are sufficiently short that it has been necessary to emphasize high gain in order to minimize B-integral effects.[12] For 3.0-ns pulses, on the other hand, the performance is limited by the damage fluences.

A staging diagram of the OMEGA laser is shown in Fig. 63.6. Values are given for the energy, fluence, and accumulated B-integral at various points for a 750-ps, temporal-Gaussian, spatially flat-topped pulse. Circular polarization is propagated through all of the 64- and 90-mm rod amplifiers to reduce non-azimuthally symmetric (i.e., "Maltese cross") beam modulation due to component birefringence (particularly in the rods), to reduce the B-integral in the rods,[13] and to reject retroreflections from optical components at the circular polarizers.[14] The laser performance used for the acceptance tests was approximately as shown in Fig. 63.6.

The beam splitting necessary to produce the requisite 60 beams is performed using a combination of wave plates and polarizing beam splitters. The first split is the stage-A split, in which the driver is split into three beams before the A amplifiers. The other splits are similar, except for the number of output beams, and will not be described in detail. The input to the stage-A splitter is first repolarized by a liquid-crystal circular polarizer[14] to eliminate changes in the split ratio in the event that the input polarization were to change. The input beam is then converted to linear polarization by an adjustable quarter-wave plate followed by a polarizing beam splitter that divides the beam into a high-contrast p-polarized beam and an s-polarized beam containing a small amount (<4% of the input intensity) of residual p-polarization. The p-polarized beam constitutes one of the three split outputs. The s-polarized beam passes through an adjustable half-wave plate and is split two ways by another polarizing beam splitter, forming the remaining two output beams. Each of the three output beams is reconverted to circular polarization by a rotatable quarter-wave plate and repolarized by another circular polarizer before leaving the split. The optical paths in the legs of the split are equalized to maintain relative beam timing. All mirror and beam-splitter reflections are kept in the same plane.

For the acceptance tests, the input energy to the A split was ~5 J. Each of the resulting three beams was amplified by a

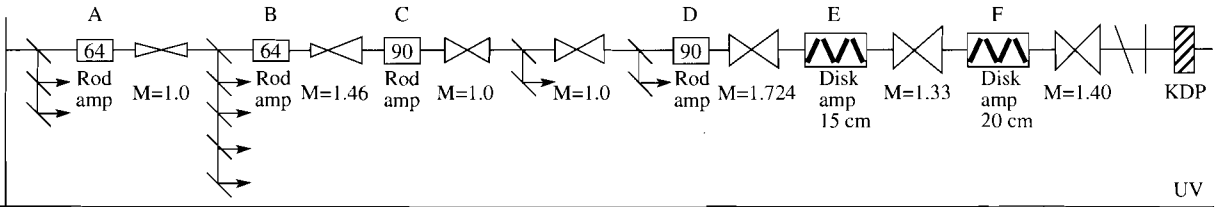

Energy (J)	1.1	12.0	11.7	2.0	21.2	20.7	103	99.4	48.2	47	22.0	124	118	402	398	1040	978	750
Avg. fluence (J/cm^2)	0.1	0.87	0.85	0.15	1.3	0.56	2.3	2.2	1.1	1.0	0.48	2.3	0.71	2.5	1.35	3.5	1.7	1.4
B-integral (radians)	0.26	0.46	0.5	0.5	0.79	0.83	1.5	1.7	1.7	1.8	1.9	2.5	2.6	2.9	3.0	3.5	3.8	----

G3578

Fig. 63.6
Staging diagram of an OMEGA beamline through stages A–F (not to scale) for an input Gaussian pulse of 0.82-ns FWHM.

factor of 10 by a 64-mm-diam, stage-A rod amplifier (with a 61-mm clear aperture). After spatial filtering, each of these beams was split vertically into five beams in the stage-B split, for a total of 15 beams with ~3 J per beam. This provided adequate drive for the subsequent 64-mm and 90-mm rod-amplifier combination (stages B and C) located in each of the 15 beamlines to produce ~100 J at the final, four-way, stage-C split. (This is essentially identical to a beamline of the old OMEGA system where a 2-J drive in each of 24 beamlines produced just over 100 J at the output.) The final three amplifiers in each beamline in the upgraded system (the stage-D rods and the disk amplifiers of stages E and F) generate 97% of the system output energy for a 0.7-ns pulse. A drive of 22 J at the stage-D rod produces over 1 kJ of IR energy at the output of the stage-F amplifier.

Frequency Conversion

The IR output of OMEGA is frequency tripled to 351 nm using two type-II KDP crystals per beam.[3,4] To guarantee high harmonic conversion it is necessary to maintain the proper phase-matching angles in the crystals. This requires precise control of the crystal orientation, the beam wavelength, and the crystal temperature. In addition, to ensure the optimum ratio of fundamental and second harmonic in the second (tripler) crystal, high-contrast linear polarization is required at the input to the first (doubler) crystal. For this reason a large-aperture polarizer is placed in each beam just before the crystals. The wavelength of the driver is constantly monitored by diagnostics with 0.05-Å resolution, and care is taken to maintain a constant wavelength. The crystals are maintained at the ambient temperature of the laser bay, which is nominally controlled to ±0.5°F. Variations in crystal temperature will be actively compensated for by using empirical temperature-tuning curves, although this has not yet proven necessary.

Prior to the installation of the crystals, the peaks of the angle-tuning curves for the doublers and triplers were found by using an off-line tuning procedure that used one of the remaining two OMEGA drivers not required for system activation. Configured to produce 100-ps, 2-mJ pulses at 5 Hz, this driver irradiated frequency-conversion cells (including the doubler and tripler) with a weakly converging beam of about 1 cm in diameter [see Fig. 63.7(a)]. This produced a spread of angles that included the optimum phase-matching angle for each of the crystals.[15] By properly referencing the experimental setup, the tuning peaks and thus the correct orientations for the doubler and tripler crystals could easily be determined in a single 20-shot (4-s) exposure of a CCD camera. Figure 63.7(b) shows one such exposure. The central lobes of the characteristic $\text{sinc}^2(x)$ intensity distributions for the green from the doubler (band AB) and the UV from the tripler (band CD) intersect at the optimum tuning position (marked with an "x"). The other broad band across the image (EF) is produced by rays that are phase matched for doubling in the tripler. The broadness of the second-harmonic (green) bands results from the relative insensitivity of doubling to changes in the ray angle along the *o* axis of each crystal. The CCD image is produced by a combination of all three wavelengths, with greatest sensitivity to the UV. Thus, there are many bands parallel to AB corresponding to green side lobes in the doubler, mostly imperceptible in the image; however, whenever these lobes intersect the line CD, i.e., are phase-matched for tripling, the UV generated is evident as a series of elliptical images. These images are narrower in the tripler tuning direction (parallel to AB) than in

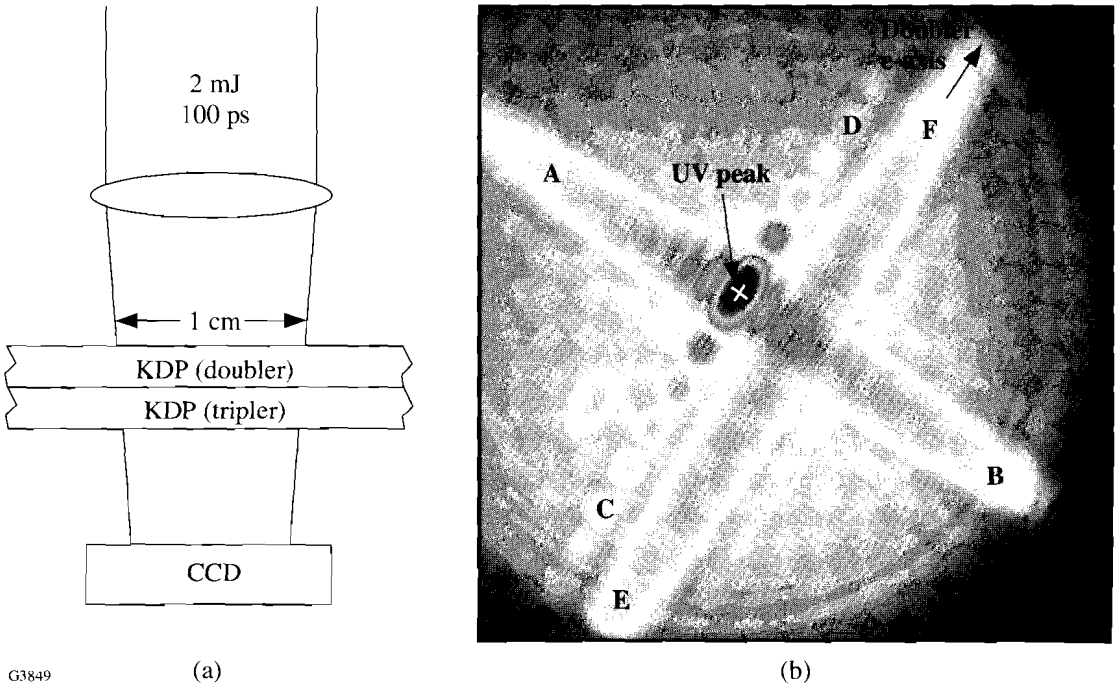

Fig. 63.7
(a) Off-line tuning technique for the frequency-conversion crystals (FCC's). A small-aperture (1-cm) beam is weakly focused through the FCC's onto a CCD camera; (b) resulting spatial pattern on the CCD. By identifying the ray in the converging beam that generates optimum UV, indicated by an "x," the necessary angle tilts of the FCC assembly in each of the two orthogonal directions may be determined. The arrow indicates the *e* axis of the doubler and the *o* axis of the tripler.

the doubler tuning direction (parallel to the arrow) because of the greater sensitivity of the tripler to the detuning angle.

The crystals were installed in the OMEGA system at the peak position as determined by the off-line tuning system. High-power angle-tuning scans were then performed about that position at 30% beam energy (300 J IR) with just three shots each for the doubler and tripler. In this procedure the doubling and tripling conversion efficiencies are fitted to the respective theoretical tuning curves, which are well represented as quadratic. The peak tuning positions were determined with a precision of ±50 μrad. The differences between the high-power peak tuning positions and those found from the off-line procedure were less than 125 μrad rms. This difference was presumed to be due mainly to a temperature differential between the off-line tuning setup and the location of the crystals in the OMEGA system. Even though no temperature compensation was applied to the crystal positions during high-power tuning, remarkably stable frequency-conversion efficiencies (70%–75%) were routinely achieved over a two-week period of activation shots. These results demonstrate the stability of the opto-mechanical alignment and the temperature control in the OMEGA facility.

Figure 63.8 is a plot of the 3ω conversion efficiency versus the IR intensity incident on the crystals. The conversion efficiency is defined as the UV energy output from the crystals divided by the IR energy input to the crystals. The incident intensity is calculated using the input IR energy inferred from the energy measurement system, the IR beam profile shown in Fig. 63.5 (which has a nominal diameter of 27 cm), and the measured IR pulse width of 725 ps at the input to the crystals.

The achievement of frequency-conversion efficiencies greater than 70% is the result of a concerted effort to produce input IR beams that are highly suited for conversion. The beams have nearly flat intensity profiles with fill factors of ~90%. [The fill factor is the ratio of the integral of the actual beam shape to that of a flat (i.e., ideal) beam filling the clear aperture.] The intrinsic polarization purity of the disk amplifi-

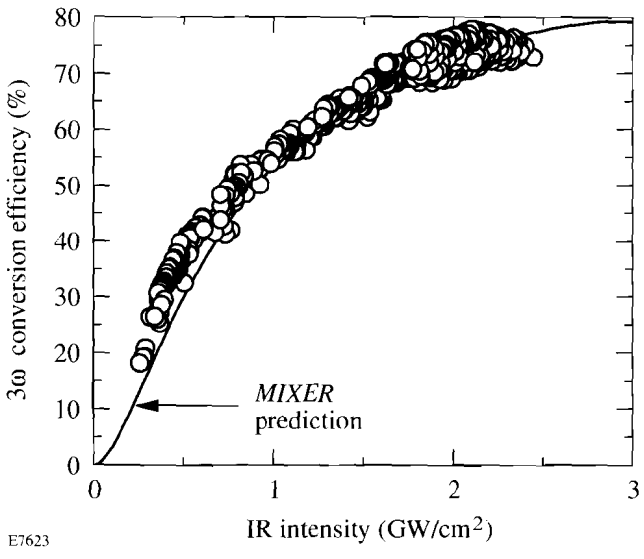

Fig. 63.8
Measured and predicted 3ω energy conversion efficiency as a function of input IR intensity. The predictions take into account the experimental spatial profile of Fig. 63.5.

ers (depolarization <1% at any point in the clear aperture) and the low stress birefringence induced in the spatial-filter lenses produce beams that contain pure linear polarization with a contrast greater than 100:1 at all points in the clear aperture. The high-contrast linear polarizers (contrast of ~500:1) then produce beams that have a very high resultant contrast at the input to the crystals. Also, the laser was designed to produce high wavefront quality: in each beamline the accumulated B-integral is less than 4 radians (at 1 ns), and the optical tolerances are consistent with beams that are <1.4 times diffraction limited at 351 nm. (Measurements of the optical wavefront quality of OMEGA beamlines are planned for early FY96.)

The measured conversion efficiencies shown in Fig. 63.8 are generally in good agreement with predictions of the code *MIXER*.[4] However, some differences may be noted. In particular, the system seems to generate slightly more UV than predicted, especially at the lower intensities. One possible explanation is that the nonlinear coefficient d_{36}/ε_0 used in the code for Fig. 63.8 is a little too low. The value used for both crystals, $d_{36}/\varepsilon_0 = 0.39$ pm/V, is the same as that inferred from the experiments of Ref. 3 and subsequently accepted as standard.[16] (This value is quoted according to the now-agreed definition of Ref. 16, which is a factor of 2 lower than the definition used in Ref. 4, where d_{36}/ε_0 was quoted as 0.78 pm/V.) A higher value of d_{36} in the tripler, which could be within the measurement error bounds of Ref. 3, would have the effect of shifting the theoretical curve to the left. The scatter in the experimental data probably reflects variations in the crystal temperatures, which were not compensated for during the acceptance tests, so it is the upper envelope of data points that should be compared with the theory. Also, variations in the laser spatial profile at differing input intensities and during the laser pulse have not been included. Additional experiments are needed to resolve the (minor) differences between prediction and experiment.

System Output Energy

To ensure optimal performance, the energy at the crystal output is measured at all three harmonic wavelengths—IR, green, and UV. This is performed with the harmonic energy diagnostics (HED's). The output (stage-F) alignment sensor package (F-ASP) for each beamline contains an optical pickoff that directs a fraction of the beamline energy (at all three wavelengths) to an integrating sphere for that beam. A single fiber optic samples the energy in the sphere and transports that signal to one of two HED's, where imaging spectrometers separate the three signals by wavelength. Each HED diagnoses 30 beams. In each HED, the 30 fibers are arranged such that, after dispersion, they form three 10×3 arrays, i.e., an image of every fiber in the IR, green, and UV. Figure 63.9 is a composite of the images from the two HED's for a single shot. Each of the beamlines, arranged in six ten-beam clusters, produces three images. The spatially integrated signal for each individual beam image is used as a measure of the energy in the beam at each wavelength. The HED's are calibrated by a full-aperture calorimeter located directly behind the F-ASP optical pickoff and at present provide energy measurements with an absolute accuracy (one standard deviation) of 2% and a relative accuracy of 1.9%. The relative accuracy is expected to improve to <1% in the near future. This system is described in detail in the following article.

The HED's were used to diagnose the beamline energy and overall beam balance for the acceptance tests. The system output energy was measured on numerous 60-beam shots, some of which were target shots. The system consistently produced >30 kJ with typical beam balances of 6%–8%. Figure 63.10 is a plot of the UV output energy versus the beamline IR energy at the crystal, including data for all beamlines for more than 20 shots. The data included some lower-energy shots produced during calibration and energy ramp-up procedures. The highest-energy 60-beam shot produced over 40 kJ of UV, and tests on an individual beam demonstrated that a beamline energy of 1 kJ IR can produce 750 J of UV. This is equivalent to a full-system output of 45 kJ UV, which, at 660 ps, corresponds to 68 TW.

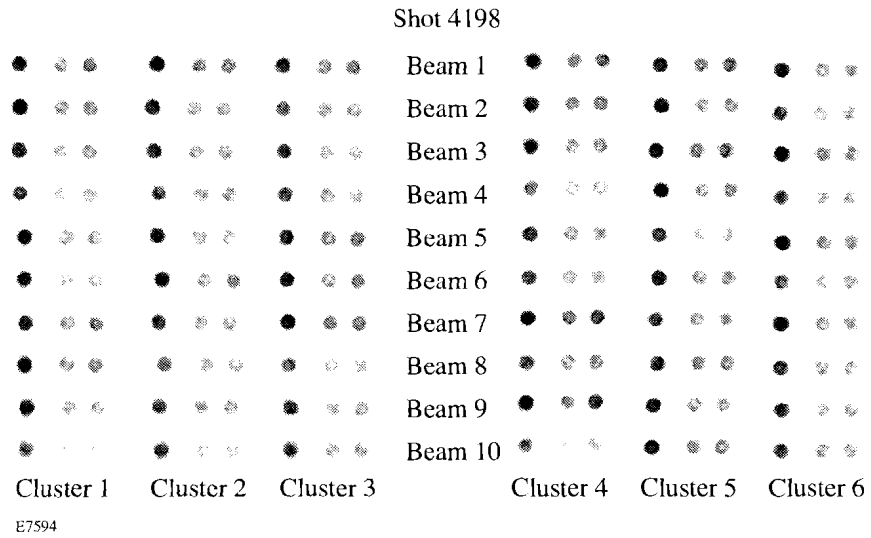

Fig. 63.9
Output of the harmonic energy diagnostic (HED) system. This produces images indicating the output energy at each of the UV, green, and IR wavelengths (from left to right) for each beam. A shot with the crystals detuned was used to illustrate the capability of the HED system—normally, very little signal is seen in the IR and green images.

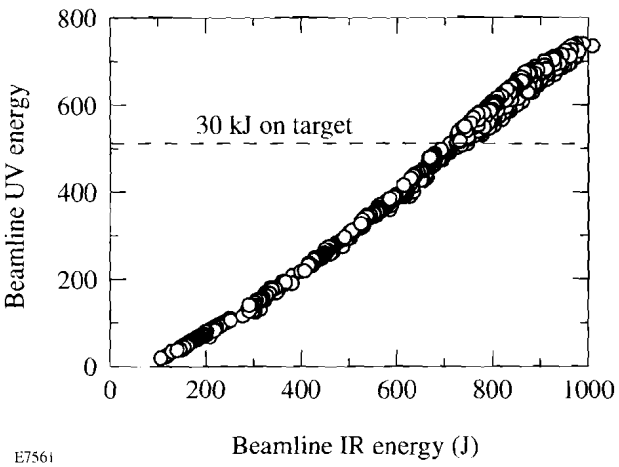

Fig. 63.10
Energy performance of the OMEGA laser. The UV energy at the FCC output is plotted against the IR energy at the FCC input for individual beams. The horizontal dashed line indicates the individual beam output energy required to produce a total energy on target of 30 kJ, taking into account transport losses from the FCC's to the target.

Temporal Pulse Shape

Figure 63.11 shows the temporal histories of the IR pulse at the input to the driver line and the output UV pulse measured on beam 45 on a shot in which 750 J of IR was produced at the input to the crystals. The steepened rise and slower falloff of the output pulse (compared with the input pulse) are caused by saturation effects in the amplifiers. The intensity dependence of frequency conversion results in the FWHM of the UV output pulse being shortened by about 10% with respect to the IR pulse at the input to the crystals. (At high conversion efficiency, the change in FWHM due to frequency conversion is minimal.) For a near-Gaussian pulse shape at the driver input, a 0.82-ns (FWHM) pulse is shortened to about 0.73 ns in the IR at the output of the last amplifier and to 0.66 ns in the UV.

The dashed curve in Fig. 63.11 is the predicted pulse shape from the laser propagation code *RAINBOW* when the measured input pulse shape is used as input to the code. This agreement indicates that the system meets the design specifications and performs as expected. Proper characterization of the system and normalization of the analysis tools are important for control of the on-target pulse shapes. Eventually, the laser propagation code will be used to propagate the desired on-target pulse shape backward through the system to determine the requisite driver pulse shape that must be produced by the pulse-shaping system. The good agreement seen in Fig. 63.11 provides confidence that accurate control of the on-target UV pulse shape will be possible.

Further verification of the accuracy of the code was provided by measurement of the pulse shape of the residual IR on a shot where the crystals were tuned (see Fig. 63.12). One curve is the signal as measured with a fast photodiode and oscilloscope, while the other is the residual IR predicted by the energy

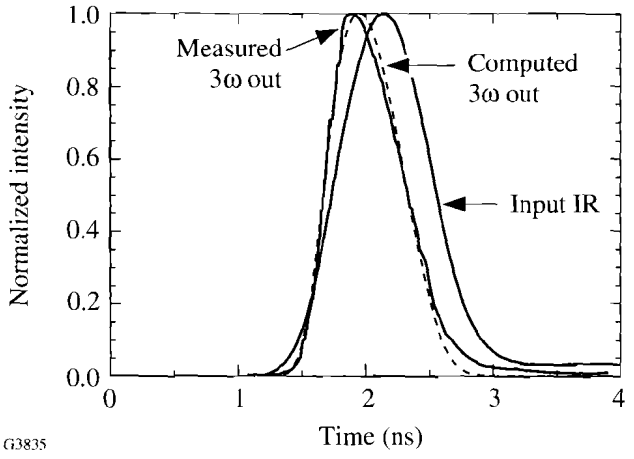

Fig. 63.11
Temporal pulse shapes measured at the input to the driver line and at the output of the FCC's. The measured output pulse shape is very close to that calculated by the propagation code *RAINBOW* (dashed curve).

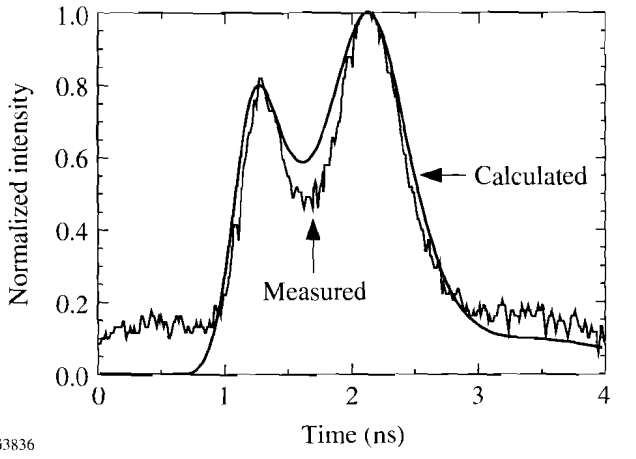

Fig. 63.12
Measured and predicted temporal pulse shape of the residual IR from a high-conversion shot, with 600 J of IR at the input to the FCC's. The *RAINBOW* prediction is shown as the smooth curve. The two peaks in time are associated with the intensity dependence of frequency conversion: maximum conversion, and thus a minimum in the residual IR, occurs at the peak of the pulse. The maximum residual IR intensity is ~13% of the maximum input IR intensity.

transport code *RAINBOW*. The two curves were normalized to match at the peak. The measured pulse shape has not been smoothed or had its pedestal removed. The predicted pulse shape was calculated by propagating the IR temporal pulse shape, measured at the input to the driver, through the driver, the system, and the frequency-conversion crystals. The calculated residual red output was then convolved with a falling-exponential (simple RC) approximation to the impulse response of the measurement's fast photodiode and oscilloscope to obtain the second plot. Even using this simple approximation, the major features of the data are replicated by the prediction. The central dip is due to the higher conversion efficiency at the center of the pulse, where conversion is maximum. The first peak is narrower than the second due to the steeper rise of the input IR pulse in comparison with its slower fall. The increased steepness of the leading edge is due to both a temporal asymmetry of the input to the driver and further steepening due to gain saturation. Since the conversion process responds essentially instantaneously for these time scales, the amplitudes of the two peaks are expected to be equal. Approximately 5% of the observed inequality is due to a change in the spatial pulse shape from early in the pulse to later times. The remainder is due to the convolution with the 180-ps impulse response of the diode and oscilloscope. The long, low intensity tail appearing in the calculation is due to an instrumental tail on the measured pulse shape used as the input to the code; its apparent agreement with the late-time background of the measured signal is fortuitous and of no significance.

Target Irradiation Tests

Each of the 60 UV output beams from the laser is transported to the target chamber using two high-reflection UV mirrors, and then focused onto target with an *f*/6.4 aspheric lens. The beams are symmetrically distributed around the target chamber in the stretched soccer-ball geometry[2] with the beams located at the vertices of the hexagons and pentagons.

For the acceptance tests, large, gold-coated CH targets were irradiated with 60 beams. The targets were 1600-μm-diam solid plastic spheres, coated with 0.4 μm of gold, with an outer 4-μm layer of CH to reduce the x-ray flux. The resulting x rays were viewed with six pinhole cameras to provide verification of the positioning of all beams on target. Figure 63.13 shows two such images, viewing the target from opposing directions. The focus lenses were set to the surface-focus position, resulting in the relatively small spot sizes (<150-μm diameter).

The hexagonal/pentagonal configuration can be seen in Fig. 63.13. For this shot the pointing accuracy was 26 μm rms, dominated by a few beams with significant pointing errors. This result was achieved using only the cw alignment system; i.e., no adjustment of the beam alignment based on these x-ray pinhole images was performed during the acceptance tests.

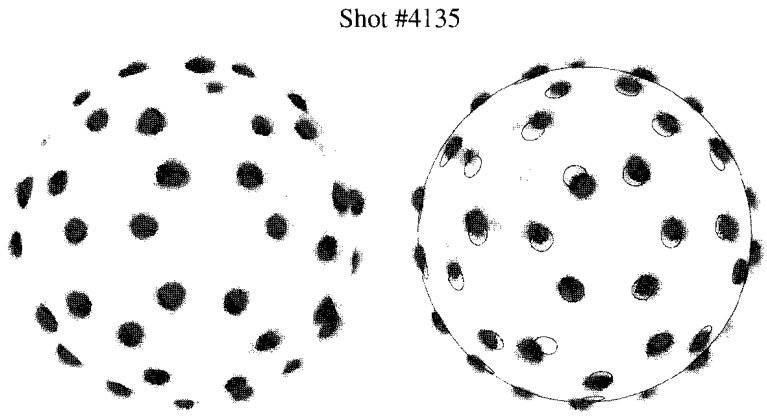

Fig. 63.13
Opposing x-ray pinhole images of a 1.6-mm-diam gold-coated target irradiated with 37 kJ in 60 tightly focused UV beams. The pentagonal and hexagonal patterns characteristic of the soccer-ball irradiation geometry are easily seen.

Significantly better pointing accuracy is expected when the alignment system is fully calibrated and between-shot feedback iterations are performed. Once calibrated, the maximum pointing error of any beam is expected to be less than 20 μm, which corresponds to 5% of the radius of a typical target. This accuracy will be more than sufficient for precision laser-fusion experiments, both direct drive and indirect drive.

Future Work

The project to upgrade the OMEGA laser system was aimed at creating a system that can be enhanced in various stages to meet the progressively more stringent demands of the planned fusion experiments. The achievement of 40 kJ of UV at ~7% beam balance, while exceeding system acceptance criteria, is only part of what will enhance the probability of success of the LLE experimental plan.[1] This plan calls for distributed phase plates (DPP's), two-dimensional smoothing by spectral dispersion (SSD), and initial pulse shaping (at ~20:1 contrast) to be implemented during FY96. These enhancements are expected to produce on-target irradiation with (rms) nonuniformities below ~5%. Ultimately, high-contrast pulse shaping (400:1), power balance control, and additional uniformity enhancements are needed to reduce nonuniformities below 2%, to enable OMEGA to be used for the implosion of high-performance capsules under near-ignition conditions.

Conclusions

The acceptance tests for OMEGA have demonstrated performance results that exceed requirements. The driver produces output pulses that are highly stable in amplitude, pulse width, and wavelength, resulting in stable and predictable performance of the entire laser system. Separate tests have also shown that the driver has the excess gain capability necessary for the future implementation of SSD and pulse shaping.

The OMEGA laser has produced over 40 kJ in the UV and has irradiated targets with up to 37 kJ with <8% rms imbalance in the energies of the 60 beams. The consistent achievement of high frequency-conversion efficiency (~75%) is indicative of good beam quality and control of the various beam and crystal parameters. The consistency of this performance over many days of operation is proof of the overall optomechanical stability of the system. Also, a 15-shot series including nine consecutive target shots has demonstrated the 1-h shot cycle that is necessary for a productive experimental program.

OMEGA is now a well-characterized system that performs above specifications. Once the planned enhancements for the control of pulse shape and uniformity are in place, the system will be uniquely capable of conducting precision direct- and indirect-drive fusion experiments.

ACKNOWLEDGMENT

This work was supported by the U.S. Department of Energy Office of Inertial Confinement Fusion under Cooperative Agreement No. DE-FC03-92SF19460, the University of Rochester, and the New York State Energy Research and Development Authority. The support of DOE does not constitute an endorsement by DOE of the views expressed in this article.

REFERENCES

1. OMEGA Upgrade Program Plan, University of Rochester, Laboratory for Laser Energetics (May 1994).
2. R. S. Craxton, ed., *OMEGA Upgrade Preliminary Design*, Laboratory for Laser Energetics Report DOE/DP 40200-101, University of Rochester (1989).
3. W. Seka, S. D. Jacobs, J. E. Rizzo, R. Boni, and R. S. Craxton, Opt. Commun. **34**, 469 (1980).
4. R. S. Craxton, IEEE J. Quantum Electron. **QE-17**, 1771 (1981).

5. Laboratory for Laser Energetics LLE Review **55**, NTIS document No. DOE/DP/40200-257, 1993 (unpublished), p. 178.

6. Laboratory for Laser Energetics LLE Review **56**, NTIS document No. DOE/DP/40200-277, 1993 (unpublished), p. 225.

7. Laboratory for Laser Energetics LLE Review **57**, NTIS document No. DOE/SF/19460-02, 1993 (unpublished), p. 32.

8. Laboratory for Laser Energetics LLE Review **58**, NTIS document No. DOE/SF/19460-17, 1994 (unpublished), p. 90.

9. T. R. Boehly, Ed., *OMEGA Upgrade Project Final Design Review* (KD3′), September 1993.

10. D. R. Speck, Lawrence Livermore National Laboratory Laser Program Annual Report 1988/89, UCRL-50021-88/89 (1993), pp. 4-10–4-12.

11. Proposal for Renewal Award for Cooperative Agreement DE-FC03-85-DP402000 (US DOE/LLE, October 1991), pp. 2.70–2.84.

12. D. C. Brown, in *High-Peak-Power Nd:Glass Laser Systems* (Springer-Verlag, New York, 1981), Vol. 7.7, pp. 227–235.

13. D. C. Brown, op. cit., p. 43.

14. S. D. Jacobs, K. A. Cerqua, T. J. Kessler, W. Seka, and R. Bahr, in *Laser Induced Damage in Optical Materials: 1984*, Nat. Bur. Stand. (U.S.) Spec. Publ. 727 (U.S. Government Printing Office, Washington, DC, 1984), p. 15.

15. W. L. Smith and T. F. Deaton, Lawrence Livermore National Laboratory Laser Program Annual Report 1979, UCRL-50021-79 (1980), p. 2-209.

16. D. Eimerl, Ferroelectrics **72**, 95 (1987).

A Novel Energy Measurement System for the OMEGA Laser

Target experiments conducted using the OMEGA laser system will require an on-target, beam-to-beam UV energy balance of 3%–4%. As a prerequisite, we have implemented an accurate beam-energy diagnostic system. This system is capable of measuring the UV laser energy and the residual green and IR energies of all 60 beams with a relative beam-to-beam accuracy of a fraction of a percent.

Overview of the Harmonic Energy Diagnostic (HED)

The stringent requirements imposed on the harmonic energy diagnostic (HED) system stimulated the adoption of a novel approach that is fundamentally different from the system implemented previously on the 24-beam OMEGA laser (see Fig. 63.14). The only common element is the use of integrating spheres that sample fractions of all three wavelengths emerging from the frequency-conversion crystals. The previous system [Fig. 63.14(a)] used discrete PIN diode detectors, with colored glass filter stacks, to isolate and sample the wavelengths of interest. The electrical signals generated by these detectors were carried by long triax cables to a central diagnostic location where they were digitized and processed by a computer. It was generally accepted that this measurement technique would be too expensive and not sufficiently precise for the 60-beam system. In the new approach [Fig. 63.14(b)] a fiber-optic delivery system coupled to a CCD detector array is used. Fibers carry the light at all three wavelengths from the integrating spheres, one per beamline, to a common location for measurement. By separating each wavelength at the output end of these fibers, only one fiber is required for each sphere, thus reducing the number of components. Furthermore, by separating the wavelengths for all the fiber-optic outputs simultaneously, the fiber outputs can be optically coupled to a

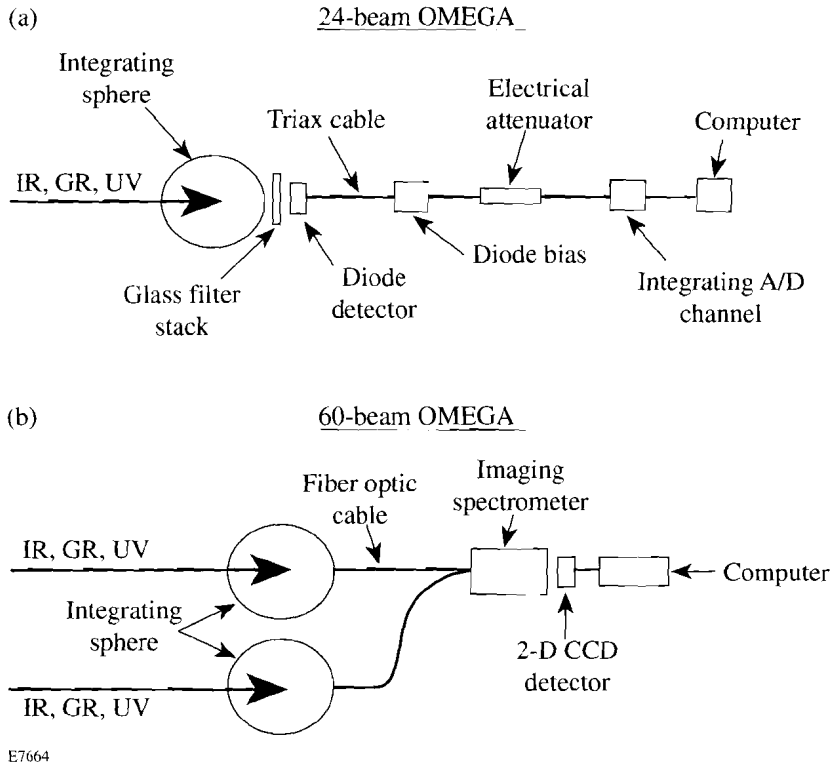

Fig. 63.14
Techniques used for laser-energy measurement on (a) the original, 24-beam OMEGA system and (b) the upgraded, 60-beam system. In the original system PIN photodiode detectors looked into an integrating sphere through three filter stacks, one for each wavelength (IR, green, and UV), and the signals were transmitted electrically to a computer. In the new system, a 300-μm-diam optical fiber samples the three wavelengths at each integrating sphere and is connected to one of two imaging spectrometers. The images are read out by a CCD detector.

single, large-format, two-dimensional CCD array detector. This architecture eliminates the need for individual detectors and acquisition channels.

Within each stage-F alignment sensor package (F-ASP) there is a three-wavelength energy pickoff, one for each beamline. The optical system is shown schematically in Fig. 63.15. The pickoff is a wedged, full-aperture piece of fused silica that is tilted at 5° to the incoming beam. The surfaces of the pickoff are curved, with radii chosen to produce a net optical power of zero in transmission. The first surface is uncoated and provides a Fresnel reflection of ~4% for each of the three wavelengths. The second surface is antireflection coated; approximately 0.5% of the beam energy is reflected from this surface but, because of the wedge, this reflection is prevented from entering the integrating sphere (see below). A second ~4% reflection occurs from a 5-in.-diam flat wedge, also made of fused silica and also tilted at 5°. The beam then passes through a window into a vacuum tube, through focus, and through a lens that recollimates it at a diameter of 36 mm before it enters the integrating sphere. A 2-in. disk of Spectralon™[1] (sintered Teflon, a highly diffusing material with a high damage threshold) is placed in the directly irradiated portion of the integrating sphere. The remainder of the sphere is painted on the inside with $BaSO_4$.

The second wedge is uncoated and serves two purposes. First, it attenuates the beam energy to 0.16% of its initial value to avoid damaging the inside of the integrating sphere. Second, it is tilted in the orthogonal plane to that of the first wedge so that the net attenuation of both wedges is the same for both "*s*" and "*p*" polarizations; this is important because the polarization of the residual IR is indeterminate. The vacuum tube is used to avoid air breakdown in the vicinity of focus, where a knife edge eliminates reflections off the second surface of each wedge. (Both wedges are in the same plane.) Laser energy transmitted through the second wedge is absorbed by a piece of 19-mm-thick filter glass. The optical design ensures that the integrating sphere is located at a system image relay plane. Thus, if co-propagation[2] is added to the system, the main and foot pulses will be spatially separated at the rear of the integrating sphere. A second sphere will then be added to diagnose the foot pulse.

The energy in each integrating sphere is sampled using a large-core, 300-μm-diam, silica optical fiber. These fibers are routed through dedicated fiber-optic conduits that protect the fibers and make them less susceptible to bending-radius changes caused by incidental touching or bumping during routine system maintenance. (Changing the bending radius changes the transmission through the optical fiber.[3]) The fibers are bundled in an ordered array of rows and columns and connected to the input of the HED measurement system. This is a spectrometer that images the output ends of all fibers onto a single CCD detector. The dispersion of the spectrometer provides for the formation of three discrete images of each fiber, one for each wavelength (see Fig. 63.16). The integrated intensity of each image is proportional to the energy in the associated beamline at the selected wavelength. The constant of proportionality is obtained from cross-calibration with conventional full-energy, full-aperture absorption calorimeters. These calorimeters are located at the output of the F-ASP structures and are rotated into the beamlines when recalibration is required. These calorimeters provide absolute energy calibration at each wavelength for each beamline.

Integrating Sphere

Significant measurement errors due to speckle can result when sampling coherent light from an integrating sphere. These errors originate from natural shot-to-shot pointing and wavefront variations in the laser output and occur when the number of speckles incident on the detector, or fiber in this

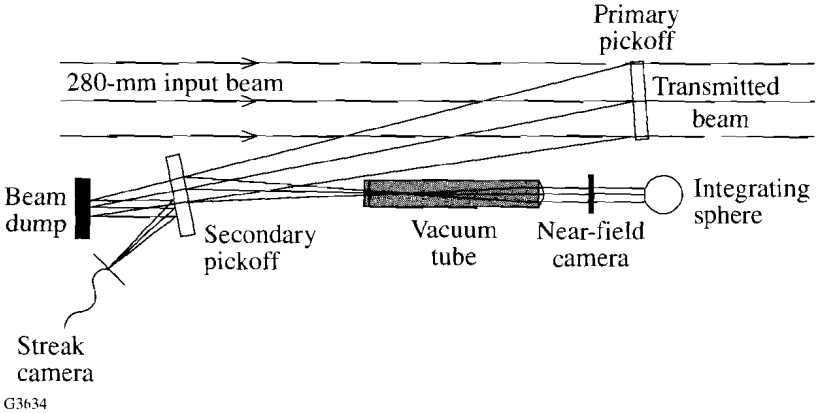

Fig. 63.15
Optical layout within the stage-F alignment sensor package (F-ASP). A small fraction of the energy in each beam is split off by the combination of a curved primary pickoff and a flat, wedged secondary pickoff and down-collimated to a 6-in.-diam integrating sphere.

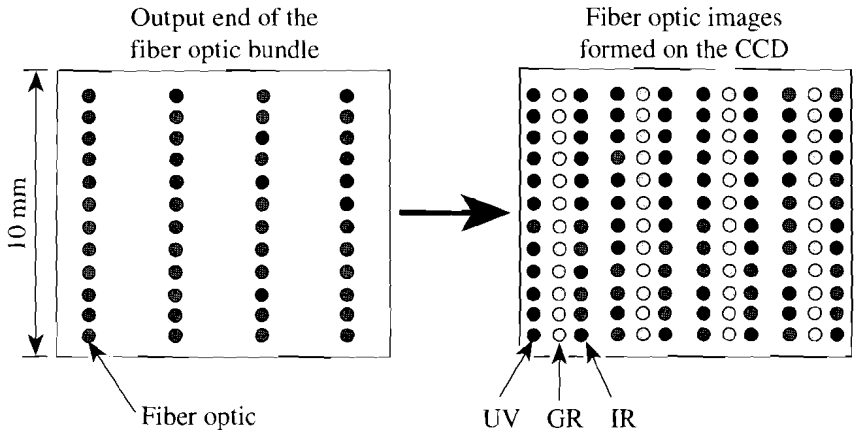

Fig. 63.16
Schematic of the output end of one of the two fiber-optic bundles (left). Each 300-μm fiber is shown as a dark circle. The spectrometer images this 10-mm-square bundle onto the CCD array as shown on the right, creating three images of each fiber, one for each wavelength. There are 96 inputs for each spectrometer. Of the 48 inputs shown, 30 are used for beam-energy measurements.

case, is small enough to produce poor sampling statistics. In the HED implementation, the 300-μm-diam fiber was tested to determine if it was compatible with the performance requirements of this instrument. A prototype integrating sphere and fiber-optic system were set up for this purpose. Two fibers were attached at different points to this sphere and imaged onto a single CCD detector (see Fig. 63.17). The sphere was illuminated with coherent light from a pulsed laser system, and the ratio of the signals from the fiber images on the CCD was recorded. The ratio of the two CCD signals remained constant, indicating that the detection system was insensitive to changes in the speckle pattern.

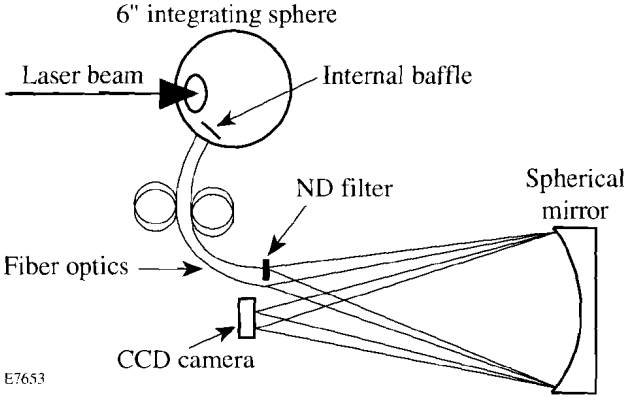

Fig. 63.17
Setup for determining the energy measurement sensitivity to speckle. Two fibers are linked to one integrating sphere and imaged onto the same CCD array. The ratio of the two CCD images remains constant from shot to shot, indicating insensitivity to changing speckle patterns.

CCD Detector

Considerable testing of the detection system (integrating sphere, fiber, spectrometer, and CCD array) was carried out to establish its efficacy in terms of both performance and cost. The linearity of the CCD detector response was tested over four orders of magnitude for short-pulse (<1-ns) signals in the IR, the green, and the UV. The same setup as Fig. 63.17 was used for this purpose, with one of the two fiber outputs attenuated by a factor of 5 relative to the other fiber using neutral density filters at the output of the fiber. The intensity ratio of the two images remained constant within a small but measurable deviation (see Fig. 63.18). A better fit was obtained by assuming that the CCD signal S was of the form $S = aE + bE^2$, where E is the optical input signal. Best fits for the coefficients a and b were found for the operating range of interest (a relative input signal in the range of 0.1–1.0) as

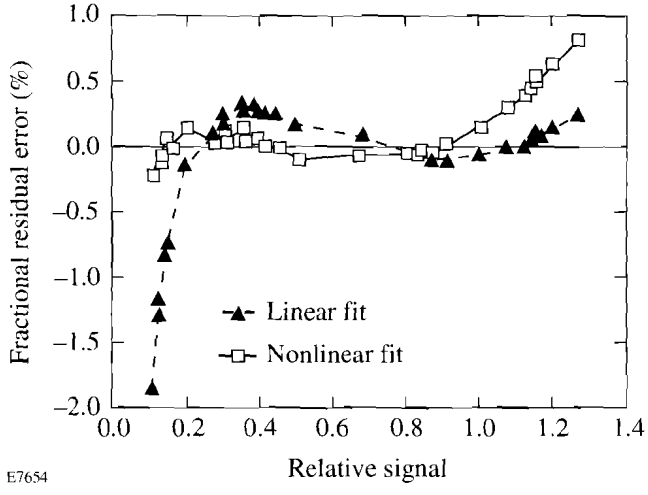

Fig. 63.18
Results from a linearity test on the CCD array. Two signals were imaged onto the CCD array, as in Fig. 63.17, but with one signal attenuated by a factor of 5. Deviations of the ratio of measured signals from this factor are plotted on the vertical axis assuming a linear fit (dashed curve) and a nonlinear fit that corrects for deviations from linearity using a small quadratic term (solid curve). The quadratic term is a fraction 0.027 of the linear term at a relative signal of 1.0. The nonlinear fit is optimized for relative signals in the range 0.1–1.0.

shown in Fig. 63.18, which illustrates the linear and nonlinear fits for the UV wavelength. The residual error corresponding to the nonlinear fit represented a very small (~0.2%) overall measurement error that can remain uncorrected. The nonlinear correction is in fact not strictly necessary for beam energy balance since all beams are equally affected by the small nonlinearity, which is only 2.7% at the maximum optical energy E (i.e., $bE/a = 0.027$ at this point). Figure 63.18 also validates the speckle-insensitive nature of the HED detection system.

Optical Design of the HED Spectrometer

The spectrometer for the HED energy measurement system is designed to match the characteristics of the fiber-optic input bundle, the CCD array, and the imaging system. The HED system is a low-dispersion instrument with fast (*f*/1.6) optics that match the numerical aperture of the fibers in the ultraviolet for maximum collection efficiency. The fiber-optic bundle does not need to be imaged near the diffraction limit of the *f*/1.6 system since it is sufficient for the light from each fiber in the bundle to be collected and concentrated into a confined spot. In fact, 50 times diffraction-limited performance (50 XDL) is sufficient to concentrate all the light into a circle of diameter less than 500 μm at the detector, allowing large amounts of astigmatism, coma, and field curvature to be tolerated. This permitted a cost-effective, all-reflective spectrometer design using parabolic mirrors. An on-axis Pfund[4] parabolic system using flat mirrors with central holes in combination with the parabolic mirrors was selected (Fig. 63.19). The parabolic mirrors were diamond turned to a figure tolerance of half a wave and then post-polished to remove the grooves. After post-polishing, the final figure of the parabolas deviated by as much as two waves, which was well within the specifications for the HED application. This loose surface figure specification made the post-polishing step easy and cost effective. Additionally, the post-polishing ensured a final surface roughness of less than 5 Å rms. All mirror surfaces have protected, enhanced UV aluminum coatings with insignificant reflective losses. Scattered light due to the central hole in the flat pickoff mirrors is minimal. Ray-trace evaluation determined that the fiber images, although heavily aberrated, especially at the edge of the field, concentrated the light into well-defined regions on the detector. An example of a digitized CCD image of a single fiber is shown in Fig. 63.20.

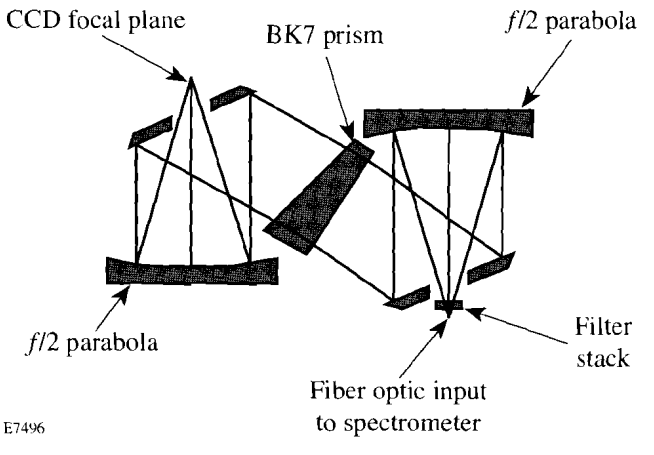

Fig. 63.19
Optical design of the HED spectrometer. This is based on Pfund's use of plane mirrors with central openings to avoid astigmatism when using parabolic collimating and focusing elements. A BK7 prism is used as the dispersive element. A single glass filter stack is used at the input to attenuate the IR, green, and UV light from each fiber.

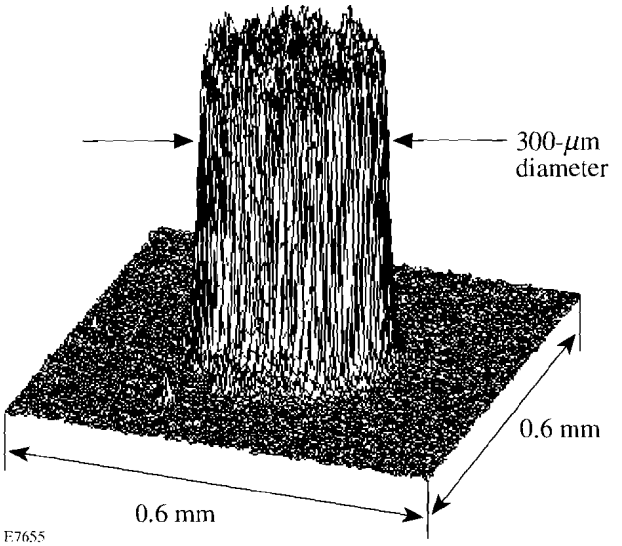

Fig. 63.20
Isometric view of a digitized CCD image of a single fiber from the multifiber bundle as imaged by the spectrometer. The fiber image is well confined within a square region of the array.

The dispersive element chosen for the HED is a single-pass, uncoated, 6° BK7 glass prism, which provides the required dispersion of ~400 nm/mm. Ray-trace analysis determined that multiple-order surface reflections from the prism faces and other reflective surfaces do not reach the detector plane.

To ensure adequate performance of the HED system it was essential to remove the vacuum window from the CCD camera. This was done primarily because this window created a serious reflected-light problem at the detector surface (see Fig. 63.21). The CCD array surface is reflective, allowing the converging light cone that focuses on this surface to be reflected back to the input vacuum window. This reflection, which is now diverg-

ing, is reflected back to the CCD detector surface by the window, showing up as a halo of light around the initial focal spot. The multiple reflections supported by this geometry result in the signal being spread for several millimeters across the detector surface. A three-wavelength antireflection coating for the window would have at best a reflectivity of a few tenths of 1% from each surface, and the image quality would still be spoiled. Tilting the window enough to walk the reflections off the array would introduce significant astigmatism. Operating the CCD camera without a vacuum window requires purging of the spectrometer with dry nitrogen (at 1 psi above ambient pressure) to protect the cooled CCD array from the condensation of atmospheric moisture. This requirement significantly affected the mechanical design of the spectrometer housing.

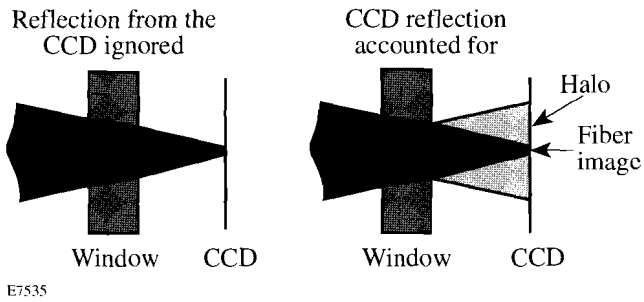

Fig. 63.21
Influence of the CCD camera window on image quality. The converging cone of light rays is focused on the CCD plane (left). With a window, some light is reflected from the CCD surface (right) and back from the window onto the CCD, leading to a halo around the image and errors in the energy measurement.

Mechanical Design of the HED Spectrometer

The primary considerations for the HED spectrometer enclosure were mechanical stability, operational simplicity, and nitrogen purging. These considerations ruled out some designs found in several commercially available spectrometers. For example, some larger spectrometers used a thick, flat mounting plate for the optical elements and a light-tight, sheet-metal cover, but this design would have been hard to seal and maintain at a positive pressure. Ray-trace analysis showed that the 50 XDL imaging requirement results in tolerances in the range of milliradians and hundreds of microns. Thus it was sufficient to machine optical mounting stations directly into the spectrometer housing without any positioning adjustments, allowing the spectrometer housing to be fabricated from solid blocks of aluminum. The housing is rigid and stable and contains the HED optics folded into a compact 20-in. × 16-in. × 9-in. package. A photograph of the spectrometer is shown in Fig. 63.22. The only adjustable component in the system is the mount for the fiber-optic bundle. This mount allows for x, y, z, and θ motion for proper centering, focusing, and angular orientation of the images on the CCD. O-ring gaskets are used to seal the spectrometer, allowing for the 1-psi overpressure and a small flow of dry nitrogen.

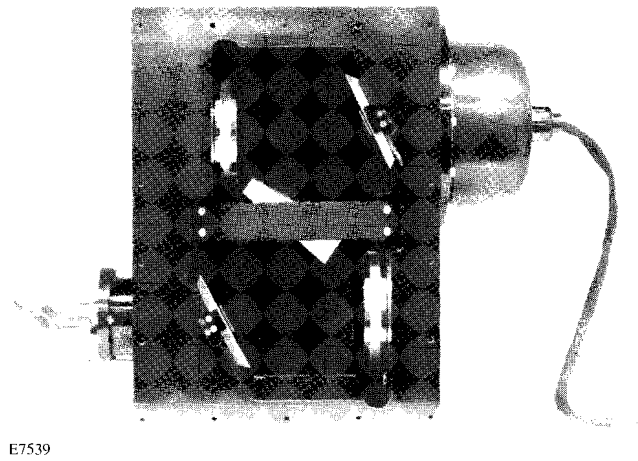

Fig. 63.22
View of the imaging spectrometer, showing the interior cavity that has been hollowed out from a solid block of aluminum. The optical elements (two parabolic mirrors, two flat mirrors, and a prism) are viewed edge-on. The fiber-optic bundle is inserted into the port on the upper right side. The CCD camera is mounted on the lower left side with the array behind the flat mirror. A gasketed plate is used to cover the front.

Multichannel Fiber-Optic Input Bundle

Fabrication of the 96-fiber bundle (300-μm core diameter) presented some challenge. This number of fibers was needed to accommodate 30 (three-color) input channels for UV conversion measurements, 30 channels for passive IR beam-balance measurements (taken from flip-in pickoffs in the final, stage-F spatial filters), and several spare channels. At the other end of the bundle each fiber terminates with a fiber-optic patch panel. Each fiber in the bundle is 1 m long.

The fiber-bundle array facing the HED spectrometer is arranged in eight columns of 12 fibers (see Fig. 63.23). Each fiber must be held at a precise transverse location within the bundle. Only the rotation of the fiber-optic core relative to the optical axis of the fiber is uncontrolled—and unimportant. To ensure that the image of each fiber optic reaches the CCD detector within a few pixels of the desired location, the horizontal and vertical position tolerance of each fiber within the

bundle is 50 μm. The tip-tilt angle of the fiber relative to the output surface normal is held to better than 2 mrad to prevent signal loss and unnecessary scattering of light due to miscentering on the clear aperture of the spectrometer imaging optics. Finally, all fibers must be in the same plane to within 25 μm to ensure that the image from each fiber is focused at the detector surface.

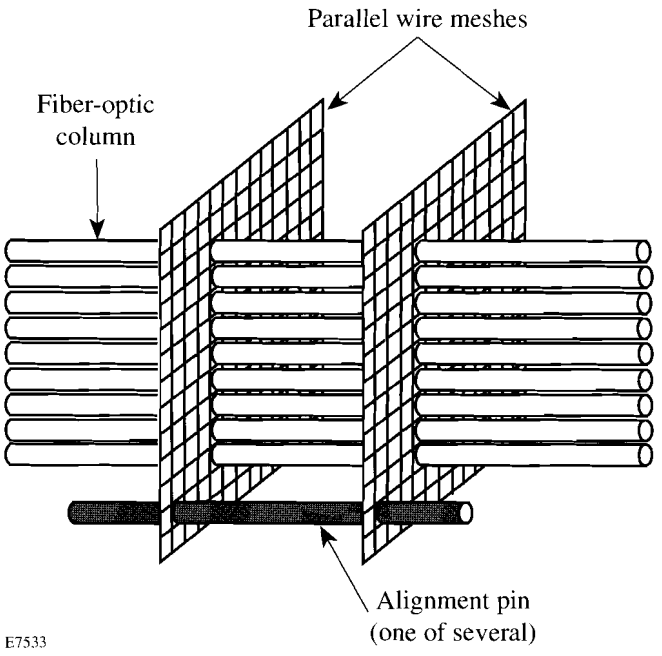

Fig. 63.23
Wire meshes used to hold the fiber bundle in position. Metal alignment pins around the perimeter (one shown) support the meshes. Nine fibers from a column are shown; the mesh holds 96 fibers in total (8 columns of 12).

This precision is achieved using two parallel wire meshes spaced 8 mm apart (Fig. 63.23). The wire meshes are coated with 5 to 10 μm of parylene prior to insertion of the fibers to prevent scratching of the fibers. The pitch and wire diameter of the mesh are selected such that the outer diameter of the fiber-optic plastic buffer fits tightly into the mesh opening. The wire meshes are cut into 25-mm squares and secured with several pins around the perimeter. Before inserting the fibers into the mesh assembly, a 10-mm length of the plastic buffer is removed (to prevent interference with the subsequent polishing operation), exposing the glass-clad core of the fiber.

During the assembly process, each fiber is inserted such that the plastic buffer extends a few millimeters beyond the second mesh. After insertion, each column of 12 fibers is held in position with a small amount of fast-curing epoxy. After all eight columns are in place, an enclosure around the fibers and the supporting mesh is filled with epoxy. The selected epoxy is one that cures with minimal shrinkage, is opaque from the IR to the UV, and can be coarse ground and polished. In addition, it has a low viscosity and is slow curing in order to fill in the spaces between the fibers and the supporting mesh and allow trapped air to escape. Once the epoxy is fully cured, the forms are removed and the exposed epoxy block is ground into a 1-in.-long, 5/8-in.-diam, cylindrical shape. The fiber output end is then coarse ground until all 96 fibers are exposed. A 3/4-in.-diam stainless steel tube with 1/32-in.-thick walls is slid over this epoxy rod such that the output end of the epoxy assembly extends about 1/8 in. beyond the end of the stainless steel tube. Additional epoxy is used to fill the gap between the epoxy rod and the stainless steel tube. Once cured, the output end of this assembly is fine ground and polished. A 3-in.-diam, 1/2-in.-thick aluminum disk with a 3/4-in.-diam hole for the bundle to slide into ensures that the output face of the bundle is ground flat. All work is done using a figure-eight rubbing motion under a steady stream of cold water. Approximately two hours of polishing with abrasive grit sizes ranging from 30 μm to 0.3 μm produces a polished bundle free of any scratched or cracked fiber-optic ends when viewed under an optical microscope.

Installation of the HED System

Fully assembled, each HED spectrometer, together with its supporting electronics and utilities, weighs about 300 lbs. Half the weight is due to the spectrometer housing, with the remaining weight due to the steel enclosure, power supplies, and CCD cooling units. Each system is housed in an EMI-shielded rack and placed on top of an F-ASP structure (see Fig. 63.24). The optical fibers from the integrating spheres are connected to the patch panels on the enclosures. A 70-psi dry nitrogen line, a fiber-optic communications connection to the remote computer network, a 120-V ac power feed, and an RG58 coax cable from the timing system are all connected to the HED unit. A trigger signal is provided by the timing system 10 s before the laser system fires so the HED can initiate internal preshot preparations. These preparations include blanking the CCD array to ensure that any residual charge has been cleared from each pixel before new data is taken. The spectrometer shutter is opened from 25 ms prior to a laser shot to 25 ms after the shot to ensure capture of the images on the CCD array. The CCD frame is later transferred from the HED unit via a computer network to the data acquisition, analysis and archiving computers. These computers reduce the data to determine the energies and conversion efficiencies and the beam-to-beam energy balance.

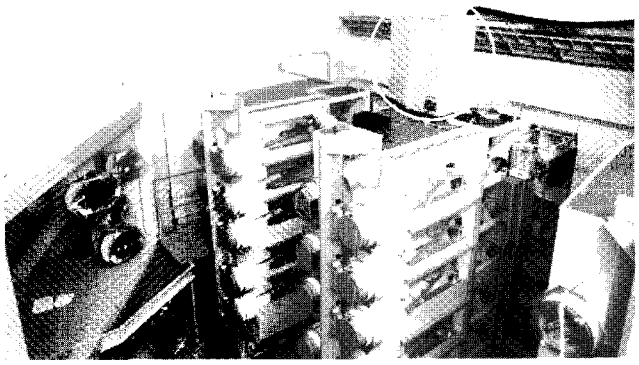

E7540

Fig. 63.24
HED enclosure shown inside the white circle on top of the F-ASP structure. The fiber optics are routed from each integrating sphere, through the square conduits, to the back of the HED rack.

Conclusion

The harmonic energy diagnostic (HED) is now an integral part of the OMEGA laser system. Data collected by the HED has been used to perform on-line, high-power, fine tuning of the frequency-conversion crystals for the 60-beam system. In addition, the HED system has provided the energy measurements used to confirm that the laser system meets its output-energy and beam-to-beam energy-balance acceptance specifications. In the future the HED, together with other instrumentation, will provide crucial measurements needed to improve the on-target energy balance.

ACKNOWLEDGMENT

This work was supported by the U.S. Department of Energy Office of Inertial Confinement Fusion under Cooperative Agreement No. DE-FC03-92SF19460, the University of Rochester, and the New York State Energy Research and Development Authority. The support of DOE does not constitute an endorsement by DOE of the views expressed in this article.

REFERENCES

1. "Spectralon" is a proprietary product available from Labsphere, N. Sutton, NH 03260.
2. R. S. Craxton, ed., *OMEGA Upgrade Preliminary Design*, Laboratory for Laser Energetics Report DOE/DP 40200-101, University of Rochester (1989).
3. A. A. P. Boechat *et al.*, Appl. Opt. **30**, 321 (1991).
4. R. A. Sawyer, *Experimental Spectroscopy*, 3rd ed. (Dover Publications, NY, 1963).

Self-Consistent Cutoff Wave Number of the Ablative Rayleigh-Taylor Instability

The Rayleigh-Taylor instability occurs at the interface between heavy and light fluids when the heavy fluid is accelerated by the light fluid. The classical treatment[1] of a sharp interface shows that a small perturbation at this boundary will grow as $e^{\gamma t}$, where $\gamma = \sqrt{A_T kg}$ is the linear growth rate, k is the mode wave number, g is the acceleration, and

$$A_T = (\rho_h - \rho_l)/(\rho_h + \rho_l)$$

is the Atwood number (ρ_h and ρ_l are the heavy- and light-fluid densities, respectively). The ablation front of an inertial-confinement-fusion (ICF) imploding target is subject to this instability because the compressed target is accelerated by the low-density ablating plasma. If small perturbations caused by either target imperfections or illumination nonuniformity grew classically, they would grow to sufficient amplitude to destroy the shell of the target and degrade the performance of the implosion. However, because the shell material is ablated by the laser, the growth is reduced with respect to the classical value and, for sufficiently short wavelengths, the instability is suppressed.[2–12] Thus, only those modes with wave number k smaller than a critical value ($k < k_c$, where k_c is the cutoff wave number) are unstable.

The calculation of the cutoff wave number of the unstable spectrum has been previously attempted by several authors.[7,8,10] The most common analytic models of the Rayleigh-Taylor instability of laser-illuminated pellets consider inviscid and incompressible fluids. The incompressible model[7,8] is not self-consistent as the equilibrium and the perturbations are described by different equations. In this model, the equilibrium flow is compressible $(\nabla \cdot \mathbf{U} \neq 0)$, but the perturbation is assumed to be divergence-free $(\nabla \cdot \tilde{\mathbf{v}} = 0)$. The incompressibility condition leads to a fourth-order differential equation for the perturbation that can be analytically solved. In other models,[5,6] the assumption of a divergence-free perturbation has been removed by retaining the effects of finite thermal conductivity. However, because of the difficulties in determining the analytic solutions, a sharp-boundary model has been used in representing the equilibrium.[5] Such an approximation to the equilibrium is not self-consistent since the plasma density in the blowoff region cannot be approximated by a flat profile. Subsequently, the growth rate has been calculated using a sharp-boundary model for the perturbations and a diffuse density profile for the equilibrium.[11] The density jump across the ablation front is calculated by retaining the thermal conductivity, and the derived growth rate is in good agreement with Takabe's numerical results.[1] Nevertheless, such a model is still not self-consistent since the equilibrium and perturbed quantities satisfy different equations. A more accurate treatment of the effect of finite thermal conductivity in a diffuse density profile can be found in Ref. 9, where the growth rate of the instability is calculated semi-analytically by matching the analytic solution in the overdense region with the numerical solution in the blowoff region. The first truly analytical estimate of the cutoff wave number for direct-drive ICF without radiation effects ($\nu = 2.5$), including the effects of finite thermal conductivity, is derived in Ref. 10. In that work, the Wentzel-Kramers-Brillouin (WKB) approximation is used to determine the solution in the downstream region assuming that the mode wavelength is smaller than the density-gradient scale length and the cutoff wave number is derived by connecting that solution with the one in the upstream region.

It is noteworthy that numerical simulations of indirect-drive ICF capsule implosions have shown a different growth rate of the instability in comparison with direct drive. We attribute this difference to the mechanism of energy transfer that, in indirect-drive ICF, is dominated by radiation transport over electronic thermal conduction. According to the simple model of Ref. 13, the heat flux transported by radiation heat conduction is

$$\mathbf{q} = -(lc/3)\nabla U_p = -(lc/3)\nabla\left(4\sigma T^4/c\right),$$

where $U_p = 4\sigma T^4/c$ is the equilibrium radiation energy density and l is the Rosseland mean free path. The energy flux can be written in terms of the gradient of temperature and an effective radiation thermal conductivity $K = 16\sigma T^3 l/c$, where the radiation mean free path l is assumed to be proportional to some power of the temperature and density. Since the pressure-

gradient scale length is much larger than the density and temperature gradient scale length in the ablation front ($p \simeq$ const), the radiation heat conduction has a strong dependence on the temperature. Thus, it became clear that a cutoff wave number formula valid for a general thermal conduction law was needed. In this article, the formula for the cutoff is derived for an arbitrary power-law dependence of the thermal conductivity ($K \sim T^{\nu}$) with $\nu > 1$, and it can be applied to a wide class of equilibria described by different values of ν. The corresponding eigenfunction is found by performing a "boundary layer" analysis of the solution in different regions of the density profile. The asymptotic matching of the eigenfunction through the boundary layers leads to an eigenvalue equation for the cutoff wave number. The analytically derived formula for the cutoff wave number is in excellent agreement with the numerical results of Ref. 6 for $\nu > 1$.

The Model

We consider an ablatively accelerated fluid in steady state. In the frame of reference of the ablation front, the evolution of the mass density ρ and the velocity $\mathbf{v}$ are described by the isobaric model of Kull and Anisimov[5]

$$\frac{\partial \rho}{\partial t} + \nabla \cdot \rho \mathbf{v} = 0 \tag{1}$$

$$\rho\left(\frac{\partial \mathbf{v}}{\partial t} + \mathbf{v} \cdot \nabla \mathbf{v}\right) = -\nabla p + \rho g \tag{2}$$

$$\nabla \cdot \left(\mathbf{v} + L_0 V_a \frac{\nabla \xi}{\xi^{\nu+2}}\right) = 0, \tag{3}$$

where $\mathbf{g} = g\mathbf{e}_y (g < 0)$, $\xi = \rho/\rho_a$ is the density normalized to its peak value ρ_a, and L_0 is the typical length of the ablation front

$$L_0 \equiv \frac{\gamma_h - 1}{\gamma_h} \frac{AK_a}{\rho_a V_a}. \tag{4}$$

Here, K_a is the thermal conductivity at the peak density, $A = m_i/(1 + Z)$ is the average particle mass, and γ_h is the ratio of specific heats. The parameter L_0 can be related to the density-gradient scale length $L = \rho(d\rho/dy)^{-1}$. Following Ref. 6, the equilibrium density profile can be obtained by combining Eqs. (1) and (3) into a single first-order differential equation

$$\frac{d\xi}{dy} = \frac{1}{L_0} \xi^{\nu+1}(1 - \xi) \tag{5}$$

with the boundary condition $\xi(y \to \infty) = 1$. Equation (5) yields the density-gradient scale length $L = L_0/\left[\xi^{\nu}(1-\xi)\right]$, and its minimum value[6] is proportional to

$$L_0\left(L_{\min} = \left[(\nu + 1)^{\nu+1}/\nu^{\nu}\right]L_0\right).$$

Although Eq. (5) cannot be solved analytically, an approximate solution can be found in the proximity of the peak density ($\xi \approx 1$ or overdense region) and the blowoff region ($\xi << 1$):

$$\xi^{\text{heavy}} \approx 1 - e^{-y/L_0} \qquad \xi^{\text{blowoff}} \approx \left(\frac{-L_0}{\nu y}\right)^{1/\nu}. \tag{6}$$

Equation (6) shows that the density gradient is sharp near the peak density where $L \simeq L_0$ and becomes smooth in the blowoff region where $L \simeq -\nu y$ and $-y >> L_0$. It is important to observe that the density-gradient scale length is determined by the thermal conductivity coefficient, the mass ablation rate, and the exponent ν. The density profile becomes smoother as K_a or ν increases.

Linear Stability Analysis

Since the equilibrium depends on the spatial coordinate y only, the perturbation can be Fourier decomposed in the x direction; i.e. $Q_1 = \tilde{Q}(y) \exp(ikx + \gamma t)$ where $\gamma \to 0^+$ for wave numbers approaching the cutoff $\left(k \to k_c^-\right)$. The linearized conservation equations can be written in the following dimensionless form:

$$\left(\Gamma_a \xi + \partial_{\hat{y}}\right)\tilde{n} + \frac{\tilde{u}_y}{\hat{L}} \frac{\xi}{\epsilon_c} + \xi \hat{\nabla} \cdot \tilde{\mathbf{u}} = 0 \tag{7a}$$

$$\tilde{\pi} - i\left(\Gamma_a \xi + \partial_{\hat{y}}\right)\tilde{u}_x = 0 \tag{7b}$$

$$\left(\Gamma_a \xi + \partial_{\hat{y}} - \frac{1}{\epsilon_c \hat{L}}\right)\tilde{u}_y + \partial_{\hat{y}} \tilde{\pi} + \tilde{n}\left(\frac{\xi}{\epsilon_c Fr} - \frac{1}{\epsilon_c \hat{L}\xi}\right) = 0 \tag{7c}$$

$$\hat{\nabla} \cdot \tilde{u} - \epsilon_c \tilde{\nabla}^2 \tilde{\Phi} = 0, \tag{7d}$$

where

$Fr = V_a^2/|g|L_0$ is the Froude number, $\hat{y} = ky$, $\Gamma_a = -\gamma/kV_a$, $\hat{\nabla} = k^{-1}\nabla$, $\epsilon_c = k_c L_0$ (k_c is the cutoff wave number), $\hat{L} = L/L_0$, and

$$\tilde{n} = \frac{\tilde{\rho}}{\rho}; \quad \tilde{\mathbf{u}} = -\frac{\tilde{\mathbf{v}}}{V_a}; \quad \tilde{\pi} = \frac{\tilde{p}}{\rho_a V_a^2}; \quad \tilde{\Phi} = \frac{\tilde{\rho}}{\xi^{\nu+2}}. \tag{7e}$$

Equations (7a)–(7d) can be easily combined into a single fifth-order differential equation for the density perturbation:

$$\left[\partial_{\hat{y}}\left(\Gamma_a\xi + \partial_{\hat{y}}\right)\partial_{\hat{y}} - \left(\Gamma_a\xi + \partial_{\hat{y}}\right)\right]\epsilon_c \hat{L}$$

$$\left[\left(\Gamma_a\xi + \partial_{\hat{y}}\right)\tilde{\Phi}\xi^{\nu} + \epsilon_c \hat{\nabla}^2\tilde{\Phi}\right]$$

$$+ \partial_{\hat{y}}\left(\Gamma_a\xi + \partial_{\hat{y}}\right)\left[\partial_{\hat{y}}\tilde{\Phi}\xi^{\nu} + \epsilon_c \hat{\nabla}^2\tilde{\Phi}\right]$$

$$+ \epsilon_c \hat{\nabla}^2\tilde{\Phi} + \tilde{\Phi}\frac{\xi^{\nu+2}}{\epsilon_c Fr} = 0. \tag{8}$$

Here, $V_a > 0$ and $\Gamma_a \to 0^-$. Equation (8) is an eigenvalue equation for the cutoff wave number $k_c(\epsilon_c = k_c L_0)$. We focus on equilibria characterized by $Fr > 1$, $\nu > 1$, and we order $\epsilon_c \sim Fr^{\nu/1-\nu}$. The validity of this assumption will be verified later by the matching conditions for the eigenfunction. In ICF, the Froude number varies significantly according to the target acceleration and the thermal conduction law. For the set of equilibria parameters considered in Ref. 4, $5 < Fr < g$, and it can be significantly lower for the equilibria considered in Ref. 14. The eigenfunction must satisfy the boundary conditions of vanishing perturbation at infinity; i.e., $\tilde{\mathbf{v}}(\pm\infty) = 0$, $\tilde{p}(\pm\infty) = 0$, and $\tilde{\rho}(\pm\infty) = 0$. Because of the variable scale length of the eigenfunction, three regions have been identified (Fig. 63.25): the overdense region (heavy fluid), the ablation front, and the blowoff region.

1. The Overdense Region

In ICF capsule implosions, the overdense portion of the shell represents the heavy-fluid region where $\hat{y} \sim 1$, $\rho \simeq \rho_a$, $\xi = 1 - \exp(-\hat{y}/\epsilon_c) + O\left[\exp(-2\hat{y}/\epsilon_c)\right]$, and $L >> L_0$. In this region and to lowest order in $\exp(-\hat{y}/\epsilon_c)$, Eq. (8) reduces to a constant-coefficient fifth-order differential equation

$$\left(\partial_{\hat{y}}^2 - 1\right)\left(\Gamma_a + \partial_{\hat{y}}\right)$$

$$\left(\epsilon_c\,\partial_{\hat{y}}^2 - \partial_{\hat{y}} + \Gamma_a - \epsilon_c\right)\tilde{\Phi}^h \exp(\hat{y}/\epsilon_c) = 0, \tag{9}$$

where $\Gamma_a \to 0^-$ and the superscript h denotes the heavy-fluid region. The solution of Eq. (9) can be written in the following form:

$$\tilde{\Phi}^h = \left(a^h e^{-\hat{y}} + b^h e^{\alpha^-\hat{y}} + c^h e^{\hat{y}} + d^h e^{-\Gamma_a\hat{y}} + q^h e^{\alpha^+\hat{y}}\right)e^{-\hat{y}/\epsilon_c}, \tag{10}$$

where a^h, b^h, c^h, d^h, q^h are integration constants and

$$\alpha^{\pm} = \left[1 \pm \sqrt{1 + 4\,\epsilon\left(\epsilon - \Gamma_a\right)}\right]\Big/2\epsilon.$$

To satisfy the boundary conditions of vanishing perturbation for $\hat{y} \to +\infty$, $c_h = d_h = q_h = 0$ and Eq. (10) reduces to the simple form

$$\tilde{\Phi}^h = \left[a^h e^{-\hat{y}} + b^h e^{\left(1-\sqrt{1+4\epsilon_c^2}\right)\hat{y}}\right]e^{-\hat{y}/\epsilon_c}. \tag{11}$$

It is important to observe that the incompressible theory $(\nabla\cdot\tilde{\mathbf{v}} = 0)$ yields only the sonic solution

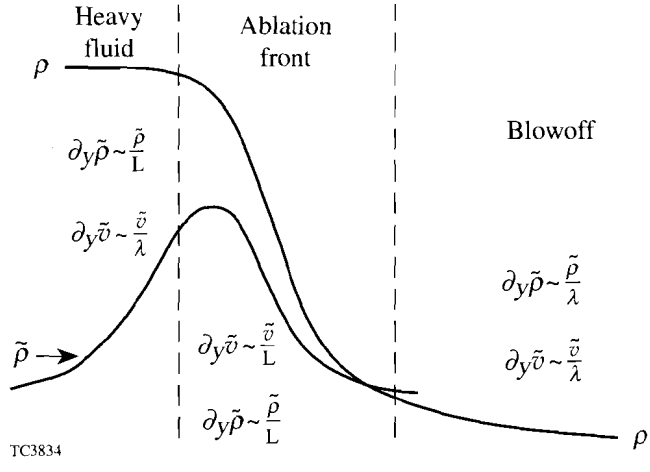

Fig. 63.25
Density profile with regions of different scale length of the perturbations. Here λ is the mode wavelength.

$$\tilde{\rho}^{\text{sonic}} \sim \exp\left[-\hat{y} - \hat{y}/\epsilon\right].$$

Equation (11) shows that a new solution is introduced by the finite thermal conductivity. Because of the diffusive character of thermal conduction, we denote the second term in Eq. (11) as the diffusion or entropy solution. Since the mode amplitude is arbitrary, we set $a_h + b_h = 1$, define the ablation front variable $z = \hat{y}/\epsilon_c$, and expand the solution for $z \sim 1$ and $\epsilon_c << 1$. A short calculation yields

$$\tilde{\Phi}^h = e^{-z}\left\{1-\left(1-b^h\right)\left[\epsilon_c\, z - \epsilon_c^2\,\frac{z^2}{2} + \epsilon_c^3\,\frac{z^3}{6} + O\left(\epsilon_c^4\right)\right] - \epsilon_c^2\, b^h z\right\}. \tag{12}$$

Each power of z in Eq. (12) needs to be matched to the ablation front solution.

2. The Ablation Front Region

The ablation front is the region where the density, velocity, and temperature profiles undergo a sharp variation. In this region, $\hat{y} \sim \epsilon_c$, $L \sim L_0$, and $\xi \sim 1$. Since $\xi \sim 1$, Eq. (5) cannot be solved in this region, and an explicit expression for the spatial dependence of the density profile cannot be found. Thus, it is more convenient to use ξ as the independent variable. By denoting with $\tilde{\Phi}^a$ the solution in the ablation region and after some straightforward manipulations, Eq. (8) can be rewritten in the following operator form:

$$\left(\mathcal{L}_0 + \epsilon_c^2\,\mathcal{L}_2 + \epsilon_c^3\,\mathcal{L}_3 + \epsilon_c^4\,\mathcal{L}_4\right)\tilde{\Phi}^a = 0, \tag{13}$$

where

$$\mathcal{L}_0 = \partial_z^3\left(\hat{L}\,\partial_z + 1\right)\left(\xi^\nu + \partial_z\right) \tag{13a}$$

$$\mathcal{L}_2 = -\partial_z^3\hat{L} - \partial_z\hat{L}\left(\partial_z\xi^\nu + \partial_z^2\right) \tag{13b}$$

$$\mathcal{L}_3 = \frac{\xi^{\nu+2}}{\epsilon_c\, Fr} \tag{13c}$$

$$\mathcal{L}_4 = \partial_z\hat{L} - 1. \tag{13d}$$

Here, $\partial_z = \xi^{\nu+1}(1-\xi)\partial_\xi$, $\hat{L} = \xi^{-\nu}/(1-\xi)$, and $z = \hat{y}/\epsilon_c$ is the ablation front coordinate ($z \sim 1$ in the ablation front region). We look for a solution of Eq. (13) in the form of an ϵ_c– series $\left(\hat{\Phi}^a = \sum_{j=0}^{\infty}\hat{\Phi}_j^a\,\epsilon_c^j\right)$, and we calculate all the terms up to third order in ϵ_c:

$$\mathcal{L}_0\hat{\Phi}_0^a = 0 \tag{14a}$$

$$\mathcal{L}_0\hat{\Phi}_1^a = 0 \tag{14b}$$

$$\mathcal{L}_0\hat{\Phi}_2^a = -\mathcal{L}_2\hat{\Phi}_0^a \tag{14c}$$

$$\mathcal{L}_0\hat{\Phi}_3^a = -\mathcal{L}_2\hat{\Phi}_1^a - \mathcal{L}_3\hat{\Phi}_0^a. \tag{14d}$$

Equation (14a) yields the following five homogeneous solutions:

$$\Psi_0 = \frac{1-\xi}{\xi} \qquad \Psi_1 = \frac{1-\xi}{\xi}z(\xi) \tag{15a}$$

$$\Psi_2 = \frac{1-\xi}{\xi}\left[\frac{z^2}{2} + \frac{1}{\nu}\int_1^\xi \frac{1+\nu\eta^\nu(\eta-1)-\eta^\nu}{\eta^{2\nu+1}(1-\eta)^2}\,d\eta\right] \tag{15b}$$

$$\Psi_3 = \frac{1-\xi}{\xi}\left[\frac{z^3}{6} - \int_1^\xi \frac{d\eta}{\eta^{\nu+1}(1-\eta)^2}\int_1^\eta z(\theta)\,\frac{1-\theta^{\nu+1}}{\theta^{\nu+1}}\,d\theta\right] \tag{15c}$$

$$\Psi_4 = \frac{1-\xi}{\xi}\int_{\xi_0}^\xi \frac{d\eta}{\eta^{\nu+1}(1-\eta)^2}, \tag{15d}$$

where the function $z(\xi)$ is derived from Eq. (5):

$$z(\xi) = \int_{\xi_0}^\xi \frac{d\tau}{\tau^{\nu+1}(1-\tau)} \tag{16}$$

(ξ_0 is the density at $z = 0$). Matching the zeroth and first-order solutions with the heavy-fluid solution yields $\tilde{\Phi}_0^a = \Psi_0$ and $\tilde{\Phi}_1^a = -\left(1-b^h\right)\Psi_1$. The second- and third-order equations [Eqs. (14c) and (14d)] are not homogeneous and require a combination of homogeneous and particular solutions to match the heavy-fluid solution. A long calculation leads to the following form of $\tilde{\Phi}_2^a$ and $\tilde{\Phi}_3^a$:

$$\tilde{\Phi}_2^a = \frac{1-\xi}{\xi}\frac{z^2}{2} - b^h\left(\Psi_1 + \Psi_2\right) \tag{17a}$$

$$\tilde{\Phi}_3^a = -\frac{1-\xi}{\xi}\left(1-b^h\right)\frac{z^3}{6} - \frac{1-\xi}{\xi}\int_1^\xi \frac{d\theta}{\theta^{\nu+1}(1-\theta)^2}\int_1^\theta ds$$

$$\times \int_1^s dx\, \frac{1-x^\nu}{x^{2\nu+1}(1-x)}\left[\frac{1}{\nu\,\epsilon_c\, Fr} + \frac{1-b^h}{\nu+1}\frac{1}{x}\right]. \tag{17b}$$

3. The Blowoff Region

The light-fluid or blowoff region is located downstream with respect to the ablation front. In this region, $-\hat{y} \sim 1$, $L >> L_0$, and $\xi \simeq \left(-L_0/\nu y\right)^{1/\nu} << 1$. The analysis can be simplified by introducing the new variable $\varsigma = \epsilon_c/\nu\,\xi^\nu$ and rewriting Eq. (8) in the following form:

$$M\tilde{\Phi}^l = 0, \tag{18a}$$

where

$$M = \partial_{\hat{y}}^4 + \partial_{\hat{y}}^3\frac{1}{\nu\varsigma} - 1 + \partial_{\hat{y}}\hat{\nabla}^2\frac{\nu\varsigma}{1-\xi}\left(\partial_{\hat{y}}\frac{1}{\nu\varsigma} + \hat{\nabla}^2\right) + \frac{1}{\nu\,\epsilon_c\, Fr}\left(\frac{\epsilon_c}{\nu}\right)^{2/\nu}\frac{1}{\varsigma^{1+2/\nu}}. \tag{18b}$$

Here, $\partial_{\hat{y}} = -\left(1-\xi\right)\partial_\varsigma$ and $\xi = \left(\epsilon_c/\nu\varsigma\right)^{1/\nu}$. Equation (18a) cannot be analytically solved for arbitrary ν. However, since $\nu > 1$ for both direct- and indirect-drive ICF, one could attempt to solve Eq. (18a) by performing a $1/\nu$ expansion of the operator and eigenfunction. Such an approach is reasonable for radiation-dominated transport in a fully ionized plasma as described in Ref. 13 ($\nu \sim 5$–8) but less convincing for electronic transport with $\nu = 2.5$. Thus, to check the validity of the expansion, we compare the analytical solution with the numerical results for $\nu = 2.5$. Based on that comparison, we deduce whether or not the $1/\nu$ expansion is a valid approach to the solution of Eq. (18a) in the regimes of interest for direct-drive ICF.

The next step is to rewrite the operator M and the eigenfunction $\tilde{\Phi}^l$ as power series in $1/\nu$:

$$M = \sum_{n=0}^{\infty} M_n\left(\frac{1}{\nu}\right)^{n-1} \tag{19}$$

$$\tilde{\Phi}^l = \sum_{n=0}^{\infty} \tilde{\Phi}_n^l\left(\hat{y}\right)\left(\frac{1}{\nu}\right)^n. \tag{20}$$

Substituting Eqs. (19) and (20) into Eq. (18a) and collecting terms up to the first two orders in $1/\nu$ leads to the following equations:

$$\partial_{\hat{y}}\left(\partial_{\hat{y}}^2 - 1\right)\varsigma\left(\partial_{\hat{y}}^2 - 1\right)\tilde{\Phi}_0^l = 0 \tag{21a}$$

$$\partial_{\hat{y}}\left(\partial_{\hat{y}}^2 - 1\right)\varsigma\left(\partial_{\hat{y}}^2 - 1\right)\tilde{\Phi}_1^l + \left[\left(1-\delta\right)\left(\partial_{\hat{y}}^4 - 1\right) + \partial_{\hat{y}}\left(\partial_{\hat{y}}^2 - 1\right)\varsigma\partial_{\hat{y}}\frac{1}{\varsigma} - \frac{\delta}{1-\delta}\partial_{\hat{y}}\left(\partial_{\hat{y}}^2 - 1\right)\varsigma\ln\varsigma\left(\partial_{\hat{y}}^2 - 1\right)\right]\tilde{\Phi}_0^l = 0, \tag{21b}$$

where $\delta = \left(\epsilon_c/\nu\right)^{1/\nu}$. We first solve the lowest-order equation [Eq. (21a)]. The solution of Eq. (21a) that satisfies the boundary conditions of vanishing perturbations at infinity can be written as a linear combination $\left[\tilde{\Phi}_0^l = A^l\tilde{\Phi}_A^l + B^l\tilde{\Phi}_B^l + C^l\tilde{\Phi}_C^l\right]$ of the following homogeneous decaying solutions:

$$\tilde{\Phi}_A^l = e^{\hat{y}} \qquad \tilde{\Phi}_B^l = e^{-\hat{y}}\int_{-\infty}^{\hat{y}} dx e^{2x}\int^x \frac{d\eta}{\varsigma(\eta)} \tag{22a}$$

$$\tilde{\Phi}_C^l = e^{\hat{y}}\int_o^{\hat{y}} dx e^{-2x}\int_{-\infty}^x d\eta\,\frac{e^{2\eta} - e^{\eta}}{\varsigma(\eta)}. \tag{22b}$$

(Note that in the light-fluid region $-\infty < \hat{y} < 0$.) To determine the constants of integration (A^l, B^l, C^l), the solution in the ablation front must be asymptotically matched to the solution in the light-fluid region. To perform the matching of the eigenfunction, it is necessary to expand the ablation front solution in powers of ($1/\nu$). A short calculation yields

$$\tilde{\Phi}^a = \frac{1-\delta}{\delta} + \frac{1}{\nu}\frac{\ln\varsigma}{\delta} + \frac{\varsigma}{\delta}\left(1-b^h\right)\left[1+\frac{1}{\nu}\left(\ln\varsigma + \frac{\delta}{1-\delta}\right)\right]$$

$$+ \frac{\varsigma^2}{2(1-\delta)^2}\left\{\frac{1-\delta}{\delta} + \frac{1}{\nu}\left[2-b^h + \left(\frac{1}{\delta}-2\right)\ln\varsigma\right]\right\}$$

$$+ \frac{\varsigma^3\left(1-b^h\right)}{6\delta(1-\delta)^2}\left\{1+\frac{1}{\nu}\left[\frac{1+5\delta+2\ln\varsigma(1-3\delta)}{2(1-\delta)}\right.\right.$$

$$\left.\left. + \frac{\delta\left(1-b^h\right)^{-1}}{2\,\epsilon_c\, Fr}\right]\right\} + O\left(\frac{1}{\nu^2}\right). \qquad (23)$$

Matching the lowest power of $1/\nu$ yields $A^l = (1-\delta)/\delta$, $B^l = 0$, and $C^l = 0$. The next step is to determine the first-order correction to $\tilde{\Phi}^l$ by substituting $\tilde{\Phi}_0^l$ into Eq. (21b) and solving for $\tilde{\Phi}_1^l$. Combining $\tilde{\Phi}_0^l$ and $\tilde{\Phi}_1^l$ gives the solution of the light-fluid equation up to first order in $1/\nu$:

$$\tilde{\Phi}^l \simeq \frac{1-\delta}{\delta} e^{\hat{y}}\left(1+\frac{1}{\nu}\frac{\ln\varsigma}{1-\delta}\right) + \frac{1-\delta}{\nu} C_1^l \tilde{\Phi}_C^l, \qquad (24)$$

where C_1^l is determined by matching Eq. (24) with the ablation front solution [Eq. (23)]. To perform the matching, we rewrite $\tilde{\Phi}^l$ for $\varsigma \to 0$:

$$\tilde{\Phi}^l(\varsigma\to 0) \simeq \frac{1-\delta}{\delta} + \frac{1}{\nu}\frac{\ln\varsigma}{\delta}$$

$$- \frac{\varsigma}{\delta}\left\{1+\frac{1}{\nu}\left[\ln\varsigma + \frac{\delta}{1-\delta}\left(1-C_1^l\ln 2\right)\right]\right\}$$

$$+ \frac{\varsigma^2}{2(1-\delta)^2}\left\{\frac{1-\delta}{\delta}\right.$$

$$\left. + \frac{1}{\nu}\left[1-C_1^l + \left(\frac{1}{\delta}-2\right)\ln\varsigma\right]\right\}$$

$$+ \frac{\varsigma^3}{6(1-\delta)^3}\left\{-\frac{1-\delta}{\delta} + \frac{1}{\nu}\left[C_1^l\left(\ln 2 + \frac{1}{2}\right) - 3\right.\right.$$

$$\left.\left. + \left(3-\frac{1}{\delta}\right)\ln\varsigma\right]\right\} + O\left(\varsigma^4\right). \qquad (25)$$

Matching equal powers of $1/\nu$ in Eqs. (23) and (25) leads to the following relations:

$$C_1^l = b^h = 2\left(1 - \frac{\ln 2}{\nu}\frac{\delta}{1-\delta}\right) \qquad (26)$$

$$\frac{1}{\epsilon_c\, Fr} \simeq \left(\frac{\epsilon_c}{\nu}\right)^{-1/\nu} + 2\left[1-\left(\frac{\epsilon_c}{\nu}\right)^{1/\nu}\right]^{-1}. \qquad (27)$$

In Eq. (27) all the terms up to first order in $1/\nu$ are retained. Higher-order terms in $1/\nu$ can be derived by solving Eq. (18a) to next order in $1/\nu$ and matching the solution with the $1/\nu$ expansion of the ablation front solution.[15] Using the results of Ref. 15, Eq. (27) can be rewritten in the following form:

$$\epsilon_c = \frac{\mu_0(\nu)}{Fr}\epsilon_c^{1/\nu} A_T(\epsilon_c) \qquad A_T(\epsilon_c) = \frac{1-\mu_0(\nu)\epsilon_c^{1/\nu}}{1+\mu_0(\nu)\epsilon_c^{1/\nu}}. \qquad (28)$$

Here, $\mu_0(\nu) = (2/\nu)^{1/\nu}/\Gamma(1+1/\nu)$, $\epsilon_c = k_c L_0$, and A_T is an effective Atwood number depending on the mode wavelength.

Discussion

The physical interpretation of the Atwood number in Eq. (28) is straightforward and may help to resolve the controversy about the right value of A_T to be used in the growth rate formulas. The classical definition of the Atwood number for a heavy fluid of constant density ρ_h superimposed on a light fluid of constant density ρ_l is $A_T = (\rho_h - \rho_l)/(\rho_h + \rho_l)$. However, for a monotonic diffuse density profile, the appropriate definition is $A_T = (\rho^+ - \rho^-)/(\rho^+ + \rho^-)$, where ρ^+ and ρ^- are the fluid densities calculated at some points where the eigenfunction is evanescent. For long-wavelength modes ($\epsilon_c = k_c L_0 << 1$), the eigenfunction for $\tilde{v}$ decays exponentially $\tilde{v} \sim e^{-k|y|}$ and becomes evanescent at a distance d of some wavelengths λ from the peak $y = 0$ ($d = \theta\lambda$, where θ is a constant of order unity). Thus, the Atwood number should be defined by setting $\rho^+ = \rho(d)$ and $\rho^- = \rho(-d)$. Using the equilibrium density profile $\rho = \xi\rho_a$ yields

$$\rho(d) = \rho_a + O\left(e^{-1/\epsilon_c}\right)$$

and

$$\rho(-d) \simeq \rho_a(\epsilon_c/\nu)^{1/\nu}/(2\pi\theta)^{1/\nu},$$

and the Atwood number of Eq. (28) is recovered by choosing $\theta = 1/2\pi\nu\mu_0^{\nu}$. It is important to observe that Eq. (28) can also be obtained by balancing the classical growth rate $\gamma_{cl} = \sqrt{A_T(\in)kg}$ with an effective ablation damping $\gamma_{ab} = -kV_{\text{eff}}$, where V_{eff} is the geometric average of the ablation velocity evaluated at distances d and $-d$ from the peak of the eigenfunction, $V_{\text{eff}} = \sqrt{V(d)V(-d)}$. Setting $\gamma = \gamma_{cl} + \gamma_{ab} = 0$ yields Eq. (28) for the cutoff wave number.

To test the validity of the $1/\nu$ expansion, we compare the cutoff wave number obtained by solving Eq. (28) with the numerical results available in the literature. Figure 63.26 shows a plot of the normalized cutoff wave number $k_c V_a^2/g$ versus the inverse Froude number. The solid line represents the solution of Eq. (28), and the dashed-dotted line represents the numerical results of Ref. 6 for $\nu = 2.5$. The remarkable agreement shown in Fig. 63.26 implies that the $1/\nu$ expansion is quite accurate even for $\nu = 2.5$. The disagreement in the regime of $Fr << 1$ is due to higher-order $\in_c$ corrections that become important for modes with wavelength shorter than the thickness of the ablation front. Figure 63.27 shows a plot of the normalized cutoff wave number versus ν for $Fr = 5$. The solid line represents the solution of Eq. (28) and the dots are the numerical results of Ref. 6. Observe the excellent agreement between the analytic and numerical results even in the region $\nu \sim 1$.

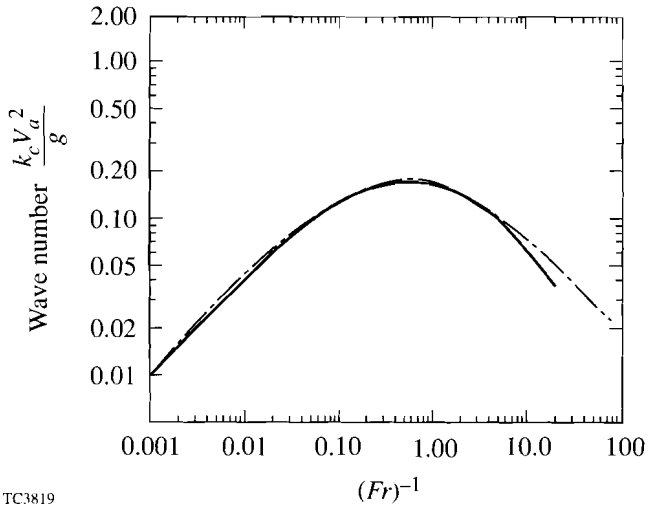

Fig. 63.26
Comparison of the normalized cutoff wave number $(k_c V_a^2/g)$ obtained from Eq. (28) (solid line) with the numerical results of Ref. 6 (dashed-dotted line).

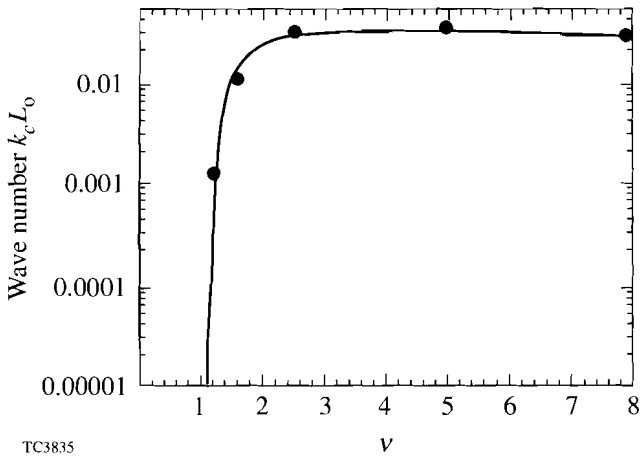

Fig. 63.27
Plot of normalized cutoff wave number $k_c L_0$ versus ν for $Fr = 5$. The solid line represents the solution of Eq. (28) and the dots are the numerical results of Ref. 6.

For electronic thermal conduction $\nu = 2.5$ and Eq. (28) can be compared with the analytic estimate of Ref. 10 that can be written in the following form:

$$\in_c = \frac{\in_c^{2/5}}{Fr}\,\frac{1-\in_c^{2/5}}{1+\in_c^{2/5}}. \tag{29}$$

Observe that Eq. (29) differs from Eq. (28) by terms $\mu_0(2.5)$. Since $\mu_0(2.5) = 1.03$, Eqs. (28)–(29) yield very similar results for electronic heat conduction. However, when diffusive radiation transport[13] dominates over electronic heat conduction, the thermal conductivity has a strong dependence on the temperature ($\nu \sim 5$–8) and Eq. (29) is not valid. In this case, the general formula (valid for arbitrary $\nu > 1$) derived in this article must be used to calculate the cutoff wave number. According to Ref. 13, $\nu = 6.5$ for a fully ionized gas; Fig. 63.28 shows the corresponding normalized cutoff wave number as a function of the inverse Froude number obtained by solving Eq. (28). We recognize that an accurate estimate of the cutoff wave number requires a more complete model of thermal conduction than the one described here. A multigroup treatment of the diffusive transport, as adopted in sophisticated codes such as *LASNEX*,[16] would probably lead to a more accurate result than the one of Eq. (28). Nevertheless, by judiciously choosing the values of ν and L_0, it is possible to fit

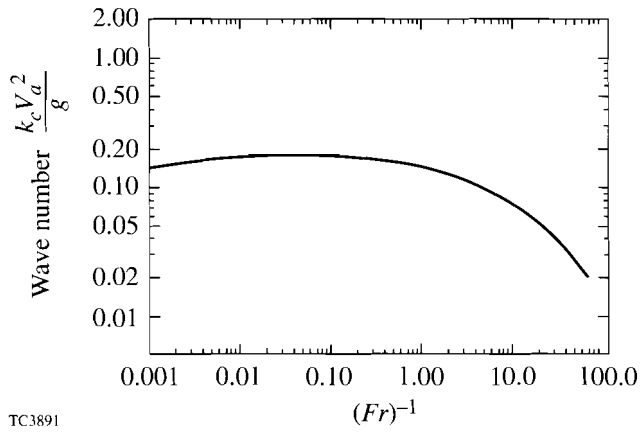

Fig. 63.28
Plot of the normalized cutoff wave number $\left(k_c V_a^2/g\right)$ obtained from Eq. (28) for $\nu = 6.5$ as a function of the inverse Froud number.

the equilibrium density profile obtained in the numerical simulations with the solution of Eq. (5). Obviously, different equilibria require different values of ν and L_0. Using such values in Eq. (28) should produce a reliable formula for the cutoff wave number with the appropriate values of the Atwood number and the ablative stabilization term.

To simplify the use of Eq. (28), the scale length L_0 is related to the distance L_e between the peak density and the $1/e$ point. The latter is the characteristic scale length widely reported in the literature. The isobaric model used here does not produce a maximum in the density and, in the overdense region, the density profile approaches the maximum value at infinity. Nevertheless, one can define an equivalent length as the distance between the point where the density is $\xi = 1/e$ and the point where the density is $\xi = \xi_0$, where $\xi_0 = 0.95$. A different choice of ξ_0 such as $\xi_0 = 0.99$ or $\xi_0 = 0.999$ would only slightly change the results as the density becomes exponentially flat in the overdense region. To determine L_e, the density profile is implicitly calculated by using Eq. (16), where $z = y/L_0$ and $\xi_0 = 0.95$. The integration in Eq. (16) can be carried out for integer or half-integer values of ν. A short calculation yields

$$\frac{L_e}{L_0} = z\left(\frac{1}{e}\right) = \sum_{i=0}^{m} \frac{e^{\nu-i}}{\nu-i}$$

$$+\ln\frac{\sqrt{\xi_0}\left(\sqrt{e}-1\right)}{\left(1-\sqrt{\xi_0}\right)} \qquad (\nu = n,\ m = n-1); \qquad (30)$$

$$\frac{L_e}{L_0} = z\left(\frac{1}{e}\right) = \sum_{i=0}^{m} \frac{e^{\nu-i}}{\nu-i}$$

$$+\ln\frac{2\sqrt{\xi_0}\left(\sqrt{e}-1\right)}{\left(\sqrt{e}+1\right)\left(1-\sqrt{\xi_0}\right)} \qquad (\nu = n+1\ 2, m = n). \qquad (31)$$

Equation (31) yields $L_e \simeq 14\ L_0$ and $L_e \simeq 190\ L_0$ for $\nu = 2.5$ and $\nu = 6.5$, respectively. Lastly, we compare the cutoff wave number derived here with the one produced by the incompressible theory of long-wavelength modes ($kL << 1$) or sharp boundary models.[2,17] These non-self-consistent derivations lead to growth rates of the form $\gamma = \sqrt{A_T kg} - \beta k V_a$, where $A_T = \left(\rho_h - \rho_l\right)/\left(\rho_h + \rho_l\right)$ is the Atwood number for flat profiles and $\beta = 1$ or 1.5. By setting $\gamma = 0$, the incompressible model yields a cutoff wave number $\epsilon_c = A_T/\left(\beta^2 Fr\right)$, quite different from the one satisfying Eq. (28).

Conclusions

The cutoff wave number of the ablative Rayleigh-Taylor instability is calculated self-consistently for an arbitrary power-law dependence of the thermal conductivity ($K \sim T^{\nu}$). The cutoff formula is valid for $\nu > 1$ and $Fr = V_a^2/gL_0 > 1$. Here V_a, g, and L_0 are the ablation velocity, the target acceleration, and the typical thickness of the ablation front, respectively. The derivation is carried out by expanding the eigenvalue equation in powers of $1/\nu$ and $\epsilon = kL_0$ and by performing a boundary layer analysis and asymptotic matching of the eigenfunction. The validity of the formula has been tested with the numerical solution of Ref. 6 up to values of ν close to 1, and the formula can be used for those equilibria (such as in indirect-drive ICF) that cannot be described by electronic heat conduction ($\nu = 2.5$ and $Fr \sim 5$).

ACKNOWLEDGMENT

This work was supported by the U.S. Department of Energy Office of Inertial Confinement Fusion under Cooperative Agreement No. DE-FC03-92SF19460, the University of Rochester, and the New York State Energy Research and Development Authority. The support of DOE does not constitute an endorsement by DOE of the views expressed in this article. Some of this work was carried out at the Institute for Theoretical Physics of the University of California at Santa Barbara, where the support of Prof. S. Cowley and the National Science Foundation (Grant No. PHY94-07194) is acknowledged.

REFERENCES

1. Lord Rayleigh, *Scientific Papers* (Cambridge University Press, Cambridge, England, 1900), Vol. II, pp. 200–207.

2. S. Bodner, Phys. Rev. Lett. **33**, 761 (1974).

3. C. P. Verdon, R. L. McCrory, R. L. Morse, G. R. Baker, D. I. Meiron, and S. A. Orszag, Phys. Fluids **25**, 1663 (1982).

4. H. Takabe, K. Mima, L. Montierth, and R. L. Morse, Phys. Fluids **28**, 3676 (1985).

5. H. J. Kull and S. I. Anisimov, Phys. Fluids **29**, 2067 (1986).

6. H. J. Kull, Phys. Fluids B **1**, 170 (1989).

7. A. B. Bud'ko and M. A. Liberman, Phys. Fluids B **4**, 3499 (1992).

8. R. Betti, V. Goncharov, R. L. McCrory, E. Turano, and C. P. Verdon, Phys. Rev. E **50**, 3968 (1994).

9. J. Sanz, Phys. Rev. Lett. **73**, 2700 (1994).

10. V. V. Bychkov, S. M. Golberg, and M. A. Liberman, Phys. Plasmas **1**, 2976 (1994).

11. J. G. Wouchuk and A. R. Piriz, Phys. Plasmas **2**, 493 (1995).

12. K. O. Mikaelian, Phys. Rev. A **46**, 6621 (1992).

13. Ya. B. Zel'dovich and Yu. P. Raizer, *Physics of Shock Waves and High-Temperature Hydrodynamic Phenomena* (Academic Press, NY, 1966), p. 152.

14. S. V. Weber, B. A. Remington, S. A. Haan, B. G. Wilson, and J. K. Nash, Phys. Plasmas **1**, 3652 (1994).

15. R. Betti, V. N. Goncharov, C. P. Verdon, and R. L. McCrory (in press).

16. G. B. Zimmerman and W. L. Kruer, Comments Plasma Phys. Controlled Fusion **11**, 51 (1975).

17. R. Betti, R. L. McCrory, and C. P. Verdon, Phys. Rev. Lett. **71**, 3131 (1993).

Distributed Phase Plates for Super-Gaussian Focal-Plane Irradiance Profiles

Various phase-plate designs have been investigated to provide different focal-plane irradiation profiles for laser-matter interaction studies. For many interaction experiments it is necessary to (1) achieve a nearly flat super-Gaussian irradiance distribution, (2) minimize scattering losses, and (3) ensure insensitivity to the laser wavefront nonuniformities. This article shows that these goals may be achieved using a distributed phase plate with a strictly continuous surface determined by a new phase-retrieval algorithm.

The first phase-plate designs intended for direct-drive spherical-implosion experiments were two-level plates consisting of an array of discrete rectangular or hexagonal subregions of either 0 or π phase within the region.[1,2] In this case the far-field envelope is defined by the Fourier transform of the subregions and does not conform to a super-Gaussian shape. The lenslet array[3] provides an efficient method of obtaining a flatter irradiation profile; however, it is difficult to control the two-dimensional shape and power spectrum of this profile. Previously designed distributed phase plates (DPP's) with a strictly continuous phase[4] have achieved 96% on-target efficiency but have yielded only a Gaussian[5] or a low-order super-Gaussian far-field distribution. None of these methods provides the desired high-order super-Gaussian shape (see Fig. 63.29) often required for applications in laser-matter interactions.

Phase-retrieval algorithms, developed by Gerchberg and Saxton[6] and Feinup,[7] have been used to synthesize phase plates yielding a higher-order super-Gaussian profile in the far field.[8] We shall refer to this method as phase retrieval with random start (PRRS), as explained below. PRRS is quite general and may be applied to the synthesis of essentially any type of far-field distribution, but we will consider only super-Gaussian distributions in this study. PRRS has no phase discontinuities of magnitude π but exhibits point singularities that cause scattering and line discontinuities of magnitude 2π that can cause scattering as a result of manufacturing errors.

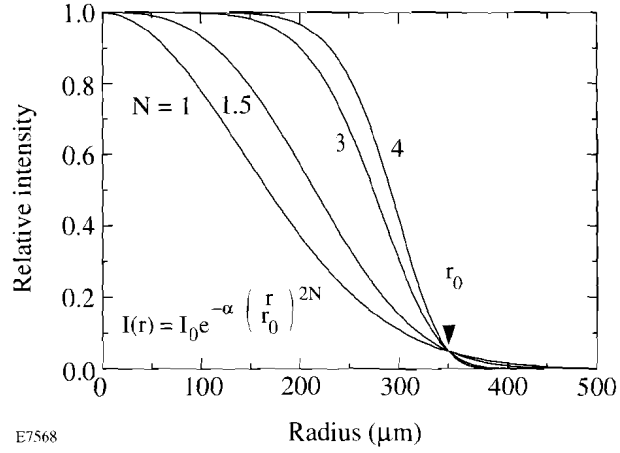

Fig. 63.29
Super-Gaussian irradiance profiles of the form $I(r) = I_0 \exp\left[-\alpha(r/r_0)^{2N}\right]$ for values of N from 1 to 4, plotted with normalized peak irradiances and with α chosen so that all curves pass through 5% of the peak irradiance at the same radius r_0. Energy-normalized profiles would emphasize differences in peak irradiance or beam size. These curves illustrate the relative flatness associated with the higher-order super-Gaussian profiles.

To design a phase plate with the PRRS algorithm, one begins with a random noise distribution (no correlation between neighboring points) in the pupil and then performs four steps iteratively.[7] Figure 63.30 illustrates this process. First, each point in the near-field complex amplitude is normalized to achieve the desired near-field intensity profile, leaving the phase unchanged. Second, the complex amplitude is propagated to the far field. Third, each point in the far-field complex amplitude is normalized to achieve the desired intensity profile while preserving the phase. Fourth, the complex amplitude is propagated back to the near field. These four steps are repeated until the solution converges or the desired level of performance is achieved.

Once the phase-retrieval iteration process is finished, the phase of the complex amplitude distribution in the near field at step 4 determines the surface profile of the phase plate. Synthe-

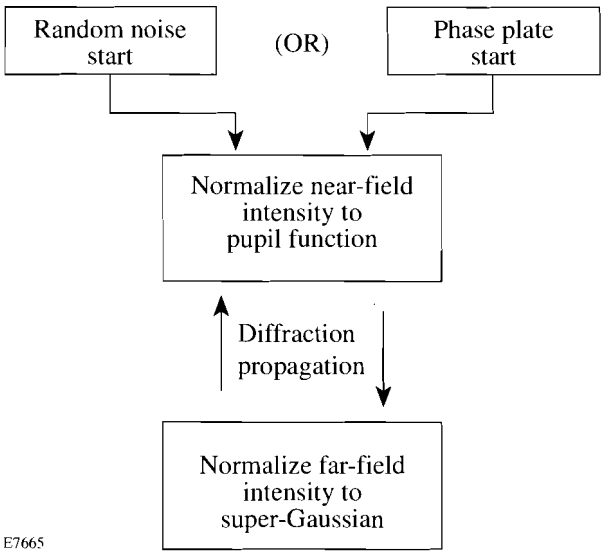

Fig. 63.30
Iterative procedure used to design phase plates according to the phase-retrieval method. Typically, random noise is used in the first pass through the process; however, other phase distributions can be used to reduce the total number of iterations required to achieve an accurate approximation to the desired far-field irradiance envelope.

sis of super-Gaussian far-field profiles by the phase-retrieval algorithm results in speckle-like phase patterns in both the near and far fields. Modulo 2π jumps arise if the range of the phase exceeds 2π because the arctangent function $\Psi = \tan^{-1}(\mathrm{Im/Re})$ maps the phase into the range $-\pi \le \Psi \le \pi$. The loci of modulo 2π jumps form closed curves. In a kinoform the modulo 2π jumps are left in place; however, phase-unwrapping algorithms can be used to remove these jumps.[9]

Branch cuts are discontinuities of magnitude 2π terminated at each end by a pair of phase poles. Branch cuts, unlike modulo 2π jumps, cannot be phase unwrapped by the elementary unwrapping algorithms because they are line segments rather than closed curves.[9] Figure 63.31 illustrates a positive-negative pole pair with a branch cut between the poles. Phase poles are phase singularities that occur at the point where the loci of real zeros and imaginary zeros cross.[10] Near a phase pole the phase Ψ is a helical function—one cycle of a screw—with a branch cut to constrain $-\pi \le \Psi \le \pi$. The approximate slope of the wavefront in the neighborhood of a circular pole is found by dividing the height of λ by the circumference $2\pi r$, where r is the distance from the pole, giving $\lambda/2\pi r$. This is the source of steep but smoothly varying wavefront slopes, which are a direct source of scattering. The association of wide-angle scattering with the location of poles has been numerically verified by blocking the on-target light in the far field, leaving only the wide-angle scattered light. The resulting distribution is backpropagated to the near field, in which high-intensity spots are found to be coincident with pole locations. Direct scattering occurs at the extreme slopes near poles and at non-2π discontinuities. The 2π line discontinuities should, in theory, cause no scattering; however, they can act as indirect sources of scatter because of finite widths produced by limitations in the manufacturing process.

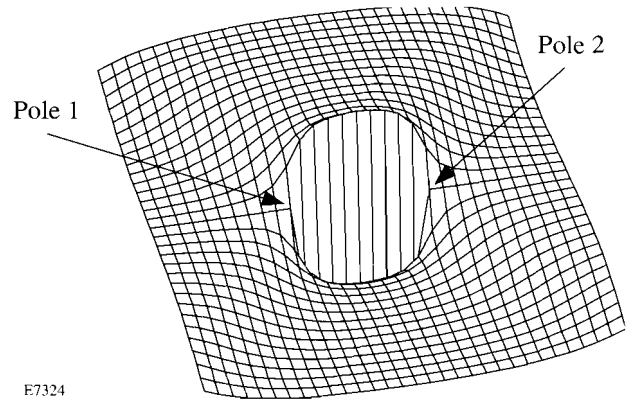

Fig. 63.31
Example of a horizontally oriented pair of positive (right) and negative (left) phase poles with a branch cut between the poles. The wavefront slope in the immediate region of each pole is approximately $\lambda/2\pi r$, where r is the distance from the pole, causing wide-angle vortex scattering. Theoretically the branch cut is a perfectly sharp discontinuity of height λ; however, manufacturing limitations can result in a finite slope to the branch cut, causing scattering loss.

When performing the numerical diffraction calculations of the phase-retrieval algorithm, only the direct source of wide-angle scattering owing to the smooth-surface effects of the vortex phase near poles is observed. The indirect scattering effects of 2π discontinuities are not observed in numerical calculations and may be minimized in the design process either by a reduction of the net length of the discontinuities through phase unwrapping and a reduction in the number of poles or by manufacturing methods that reduce the discontinuity width. For a 0.351-μm wavelength, a 28-cm near-field pupil, a 180-cm focal length, and a 350-μm target radius, PRRS generates ~10,000 poles. Scattering from the vortex surfaces caused a direct scattering loss of ~5%. In this example, wide-angle scattering can be defined as the energy outside a radius of 500 μm. In addition to the 5% scattering loss due to vortex

surfaces, there are additional losses due to the 2π discontinuities: both modulo 2π jumps and branch cuts. If the number of poles can be reduced, then the direct scattering due to vortex surfaces and the indirect scattering due to branch cuts will be reduced.

A strictly continuous phase plate will have negligible scattering loss. Recently a continuous DPP has been developed, using a two-dimensional Fourier grating with random phase to produce a low-order super-Gaussian profile in the far field.[4] For the 60-beam OMEGA laser system, the smallest target radius is 350 μm and the f number is ~6.4. A Fourier grating with a spatial period of 0.49 cm and an amplitude of 0.228 waves (at $\lambda = 351$ nm) was used to produce equal far-field modulation for the 0, +1, and −1 orders and generate approximately five major peaks in the far field to form a super-Gaussian envelope. A random phase with an rms value of 0.5 waves and autocorrelation diameter of 0.9 cm was added to the Fourier grating to fill in the gaps between the major peaks of the far field. Figure 63.32 illustrates the far-field patterns from (a) the Fourier grating and (b) a random phase distribution. The GLAD code[11] is used for the DPP design and analysis, in addition to various phase-retrieval algorithms.

The above hybrid DPP design, instead of random noise, was used as a starting point for the phase-retrieval algorithm for the design of the higher-order super-Gaussian DPP.[12] This algorithm is denoted as phase retrieval starting from the hybrid design (PRHD). As indicated in Table 63.I, only 1,400 poles were observed, compared with 10,000 poles for the PRRS. We used only two cycles of phase retrieval since more cycles did not improve the fit to the desired super-Gaussian and resulted in additional poles. Figure 63.33 compares the azimuthally averaged profiles of the desired fourth-order super-Gaussian profile with those produced by the starting hybrid DPP, PRRS, and PRHD, in which an ensemble average based on 100 different noise seeds was used for the random aspects of each design method. The azimuthal average provides strong noise smoothing for larger values of r but no smoothing at $r = 0$. The ensemble average provides additional noise smoothing to display better the shape of the curves at small values of r.

PRHD provides the widest flat region in the center of the target area. As summarized in Table 63.I, the PRRS design has ~5% direct scattering outside the 500-μm radius, compared with 2% for the PRHD design. It is also expected that the indirect scattering that is due to 2π discontinuities will be much lower for the PRHD than the PRRS because there are only 1,400 poles, compared with 10,000 poles, giving a much lower net length of 2π discontinuities, which become important when manufacturing limitations are included.

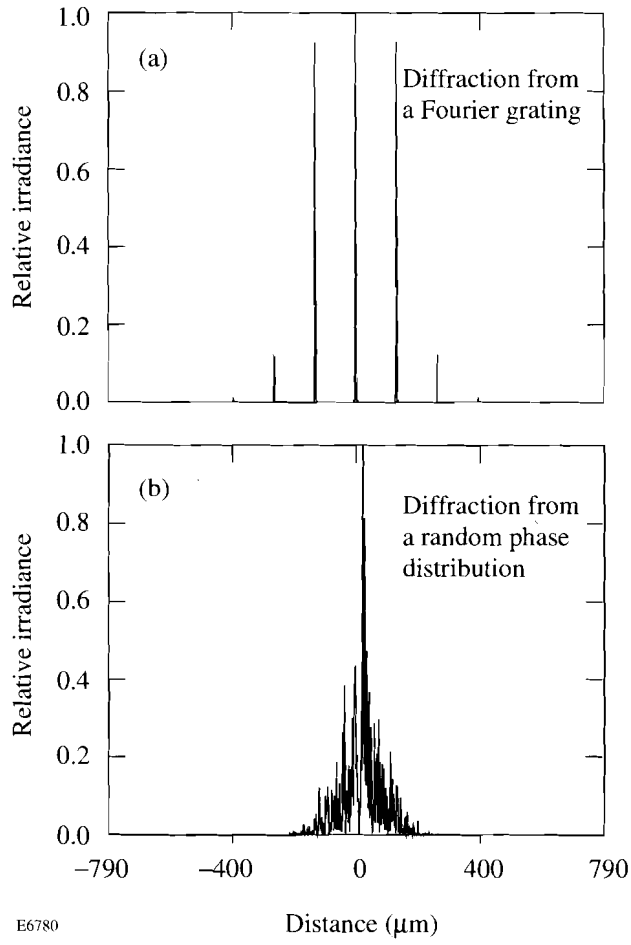

Fig. 63.32
Far-field patterns from (a) a Fourier grating and (b) a random phase distribution used as a starting point for the new phase-retrieval method of designing super-Gaussian DPP's. Since this hybrid DPP produces a far-field irradiance envelope closer to the desired envelope, fewer iterations are required for convergence to the desired super-Gaussian envelope.

Table 63.I: Pole counts and wide-angle scattering losses for the three design types.[(a)]

Phase-plate type	Number of poles	Direct scattering outside 500-μm radius (%)	Approximate super-Gaussian order
PRRS	10,000	5.0	4.0
Hybrid DPP	0	0.3	1.5
PRHD	1,400	2.0	4.0

[(a)] Only direct scattering due to vortices is included in the table.

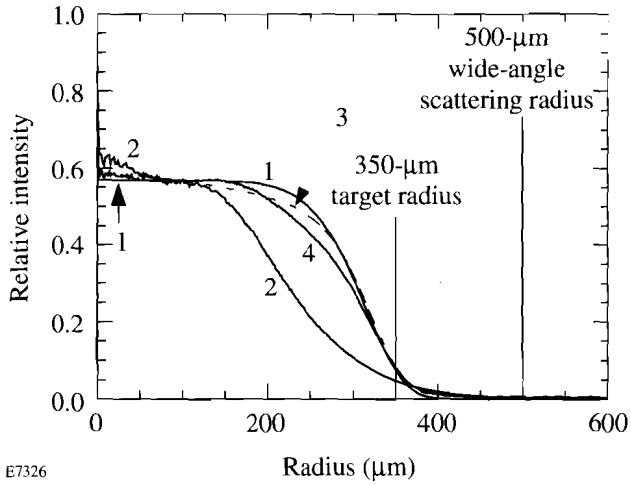

Fig. 63.33
Azimuthally averaged profiles of the fourth-order super-Gaussian function (curve 1), the hybrid DPP (curve 2), the PRRS (curve 3), and the PRHD (curve 4). The curves represent an ensemble average of 100 calculations done with different random seeds. Light that falls outside 500 μm is considered wide-angle scattering. The PRHD has a wider flat region in the center than does the PRRS.

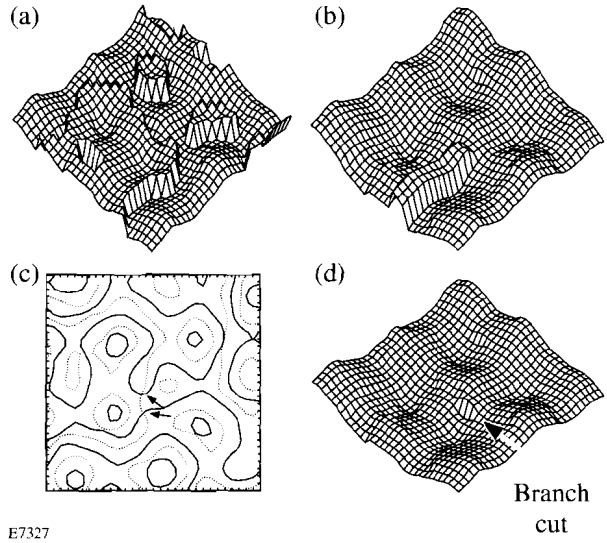

Fig. 63.34
(a) Phase plot of PRHD kinoform showing a 1.2-cm × 1.2-cm section of the 28-cm-diam beam. Islands and plateaus of height λ result in discontinuities of net length ~140 pixel lengths. (b) Conventional phase unwrapping, which ignores branch cuts, reduces the net length of the discontinuities. The phase-unwrapping algorithm fails at the branch cut between the vertically oriented pole pair near the center of the display, creating a spurious horizontal plateau of 28 pixel lengths. (c) Loci of real (solid lines) and imaginary (dotted lines) zeros. The two primary poles are marked. (d) Phase unwrapping with branch-cut recognition reduces the net discontinuity length to the length of the branch cut (approximately two pixel lengths).

Modulo 2π discontinuity scattering, unlike vortex surface scattering, may be reduced by phase unwrapping. Figure 63.34(a) shows a 1.2-cm × 1.2-cm section of the 28-cm-diam aperture with no phase unwrapping and represents the surface if the PRHD were to be implemented as a kinoform. The net discontinuity length for this small section is ~140 pixel lengths. Islands of 2π height are apparent. Figure 63.34(b) shows the result of a conventional phase-unwrapping algorithm that attempts to achieve continuity by first resolving the center column and then resolving the horizontal rows from the center to the left and from the center to the right.[9] The net scattering length is reduced to ~28 pixels. Figure 63.34(c) indicates the pole pair by the crossing of real and imaginary loci. The phase-unwrapping algorithm used in Fig. 63.34(b) did not recognize the branch cut and generated the 13-pixel-long plateau of high phase, seen in Fig. 63.34(c), as a spurious effect. Figure 63.34(d) shows the same small section after correction for the branch cut. The net discontinuity length has been reduced from approximately 140 to 2 pixel lengths.

Summary

A new distributed phase plate that achieves a good approximation to a fourth-order super-Gaussian with very low scattering losses has been designed. Low scattering is achieved because the new design is nearly continuous, having fewer phase poles and a lower net length of 2π phase discontinuities. The net length of 2π discontinuity lines, which in practice are an additional source of scattering because of finite width when manufactured, may be reduced to a low level by a phase-unwrapping algorithm capable of treating branch cuts. Preliminary investigations suggest that even-higher-order super-Gaussian far-field profiles can be generated with this technique.

ACKNOWLEDGMENT

Helpful discussions with Sham Dixit, David Freid, and James Feinup are acknowledged. This work was supported by the U.S. Department of Energy Office of Inertial Confinement Fusion under Cooperative Agreement No. DE-FC03-92SF19460, the University of Rochester, and the New York State Energy Research and Development Authority. The support of DOE does not constitute an endorsement by DOE of the views expressed in this article.

REFERENCES

1. Y. Kato *et al.*, Phys. Rev. Lett. **53**, 1057 (1984).
2. Laboratory for Laser Energetics LLE Review **33**, NTIS document No. DOE/DP40200-65, 1987 (unpublished), p. 1.
3. X. Deng *et al.*, Appl. Opt. **25**, 377 (1986).

4. T. J. Kessler, Y. Lin, J. J. Armstrong, and B. Velazquez, Proc. Soc. Photo-Opt. Instrum. Eng. **1870**, 95 (1993).

5. J. W. Goodman, in *Laser Speckle and Related Phenomena*, Springer Series in Applied Physics, Vol. 9, edited by J. C. Dainty (Springer-Verlag, Berlin, 1984), Chap. 2, p. 9.

6. R. W. Gerchberg and W. O. Saxton, OPTIK **35**, 237 (1972).

7. J. R. Fienup, Appl. Opt. **21**, 2758 (1982).

8. S. N. Dixit *et al.*, Opt. Lett. **19**, 417 (1994).

9. J. M. Huntley, Appl. Opt. **28**, 3268 (1989).

10. B. Ya. Zel'dovich, N. F. Pilipetsky, and V. V. Shkunov, in *Principles of Phase Conjugation*, Springer Series in Optical Sciences, Vol. 42, edited by T. Tamir (Springer-Verlag, Berlin, 1985), p. 79.

11. GLAD is a general purpose laser system and physical-optics computer program. It is a proprietary product of Applied Optics Research, Tucson, AZ.

12. Y. Lin, T. J. Kessler, and G. N. Lawrence, Opt. Lett. **20**, 764 (1995).

Electro-Optic Sampling of 1.5-ps Photoresponse Signals from $YBa_2Cu_3O_{7-\delta}$ Thin Films

Studies of the fast photoresponse of high-T_c thin films may reveal important information on scattering mechanisms or nonequilibrium processes in high-T_c materials. Optical pump-probe experiments on $YBa_2Cu_3O_{7-\delta}$ (YBCO) thin films have reported picosecond and subpicosecond time constants,[1,2] but the interpretation of the results is still controversial. Photoresponse experiments with current-biased samples may provide more direct information on nonequilibrium processes,[3–8] but the bandwidth of the oscilloscopes used in these experiments is usually the limiting factor in resolving fast voltage transients on the picosecond time scale. Photoresponse signals with widths ranging from 16 to 40 ps have been reported recently using fast oscilloscopes.[5,7,8] Electro-optic sampling,[9] on the other hand, offers improved time resolution in the subpicosecond regime and has been used to study superconducting electronics[10] and the propagation of picosecond pulses on superconducting coplanar transmission lines.[11] Electro-optic sampling has also been used recently to show that laser-induced switching of Pb transmission lines from the superconducting to the normal state occurs within 1 ps.[12]

This article describes experiments that, to the best of our knowledge, are the first to use electro-optic sampling to study the photoresponse of YBCO thin films. We have observed electrical transients as fast as 1.5-ps full-width at half-maximum (FWHM), which are the fastest photoresponse signals reported to date from a YBCO thin film. We have also found that picosecond transients can be seen in optically thick films (>100 nm), despite previous claims that fast transients can be seen only in ultrathin films with thicknesses of the order of 10 nm.

A schematic of the experimental setup is shown in Fig. 63.35. The *c*-axis YBCO films were grown epitaxially by laser ablation on 0.5-mm-thick $LaAlO_3$ substrates. Films with thicknesses of 100 and 200 nm were used. A coplanar transmission line structure[7] was patterned into the films using standard photolithographic techniques and a wet chemical etch. The center line of the coplanar waveguide (CPW) had a width of 130 μm, and the width of the gap to the ground lines was 336 μm. The length of the CPW was about 1.5 mm. A bias current could be applied to one end of the CPW, while the other end was terminated to the ground plane by a narrow bridge with a length of 100 μm. The bridge widths were 7 μm and 17 μm for the 100-nm film, and 10 μm for the 200-nm film.

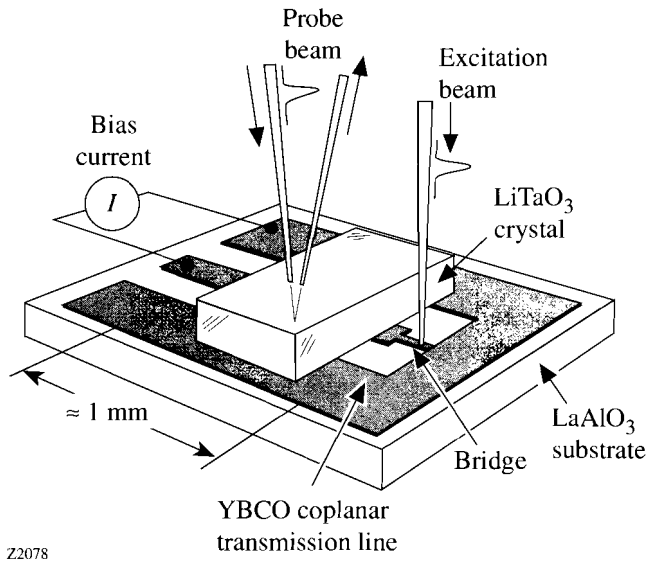

Fig. 63.35
Schematic of the experimental setup.

After processing, the 7-μm bridge of the 100-nm film had a zero-resistance critical temperature T_{c0} of 90.5 K and a transition width of about 0.8 K. The resistivity ρ at 100 K was 144 $\mu\Omega$ cm (R = 205 Ω), and the critical current J_c at 77 K was about 2×10^6 A/cm^2 (I_c = 12 mA) using a 10 μV/cm criterion for the onset of dissipation in the bridge. As described elsewhere,[7] the 10-μm bridge of the 200-nm film had T_{c0} = 89 K, ρ(100 K) = 124 $\mu\Omega$ cm (R = 62 Ω), and $J_c = 1.5 \times 10^6$ A/cm^2 (I_c = 29 mA).

A mode-locked Ti:sapphire laser operating at a repetition rate of 76 MHz was used to generate 150-fs pulses at a wavelength of 790 nm. To perform electro-optic sampling,[10] the pulses were split into two beams: an excitation beam for

inducing a photoreponse signal in the bridge, and a probe beam for monitoring the electric field from the resulting voltage transient in the $LiTaO_3$ crystal. Both beams were focused onto the sample by passing them through the same microscope objective, also used for viewing the illuminated region. The diameter of the spot size on the bridge was about 10 μm. The excitation beam was chopped by an acousto-optic modulator at a frequency of 1 MHz, and a translation stage provided the necessary time delay of the probe beam with respect to the excitation beam. The electric field in the electro-optic crystal was probed close to the edge of the center line of the CPW and about 400 to 500 μm from the position of the microbridge. A reflective dielectric coating on the bottom face of the 1-mm-thick $LiTaO_3$ crystal reflected the probe beam back out through the microscope objective to an analyzer that detected the change in polarization of the probe beam arising from the electric field of the photoresponse signal. Lock-in amplification techniques were then used to extract the electro-optic signal. After 30 averages for each waveform, a voltage resolution of about 0.5 mV for the photoresponse signals could be obtained. Due to large reflections from the end of the short transmission line, time delays beyond 40 to 50 ps could not be studied.

As described elsewhere,[7] the samples were mounted in vacuum on a cold finger cooled with liquid nitrogen. All the experiments discussed here were therefore carried out at a base temperature of 78.6 K, as measured by a temperature diode placed near the sample. It is important to note that increasing the average power P_{av} of the excitation beam raised the average temperature of the film at the laser spot. It was estimated that the average temperature increase of the portion of the bridge illuminated by the beam was about 3 K/mW. Thus, for $P_{av} = 0.4$ mW incident on the bridge, the base temperature would increase to 79.8 K.

Figure 63.36 shows a 1.5-ps-wide voltage transient observed from the 7-μm bridge of the 100-nm film. The slow rise time and the faster fall time of the transient followed by oscillations suggest that the original photoresponse signal generated at the bridge has experienced some dispersion by the time it reaches the sampling point in the electro-optic crystal.[11] The inset of Fig. 63.36 shows a 1.8-ps-wide photoresponse signal from the 10-μm bridge of the 200-nm film. Figure 63.37 shows the dependence of the photoresponse signal on the bias current for the 7-μm bridge of the 100-nm film at a fixed fluence of 15 $\mu J/cm^2$. At high bias currents, as shown in Fig. 63.37(a), there is a fast transient less than 2 ps wide followed by a fast tail with a fall time of about 10 ps. At later

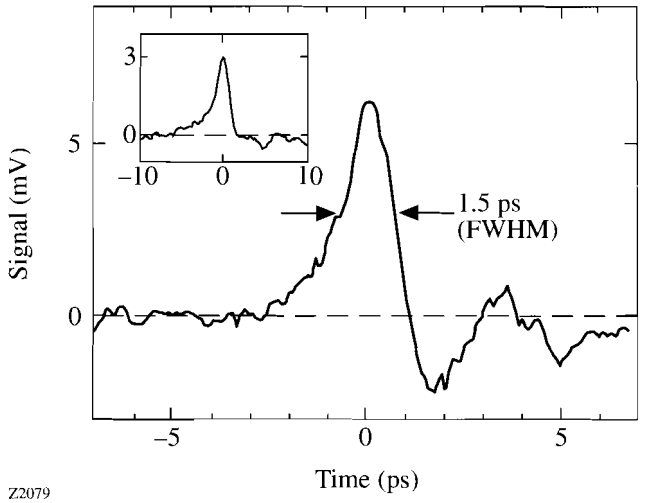

Fig. 63.36
Photoresponse signal from a 7-μm-wide bridge of a 100-nm-thick YBCO film at a bias current of 15 mA and a fluence of 15 $\mu J/cm^2$ ($P_{av} = 0.4$ mW). The full-width at half-maximum (FWHM) of the voltage transient is 1.5 ps. The inset shows a photoresponse signal from a 10-μm-wide bridge of a 200-nm-thick film at the same fluence but at a bias current of 60 mA. The width of the signal in the inset is about 1.8-ps FWHM.

times, a much slower component develops due to a resistive bolometric response of the film.[6,7] As the bias current is decreased, as in Fig. 63.37(b), the amplitude of the fast tail becomes much smaller with respect to that of the initial fast transient, and only a small amount of the resistive component remains. At lower bias currents, the fast tail and resistive component disappear completely, as shown in Fig. 63.37(c) and in the 15-mA case of Fig. 63.36, and only the picosecond transient remains, followed by a negative component in the signal with a decay time of about 15 ps.

We believe that the picosecond photoresponse transient (FWHM < 2 ps) is due to a kinetic inductive response given by $V = I\, dL/dt$, where V is the voltage, I is the bias current, and L is the kinetic inductance of the bridge.[3,5–8] Figure 63.38 confirms the linear behavior of the amplitude of the picosecond photoresponse signal with the bias current, as predicted by a kinetic inductive response. The kinetic inductance of a superconducting bridge is inversely proportional to the superfluid density. In a purely kinetic inductive response, a positive voltage transient represents a net breaking of Cooper pairs, and a negative transient signifies a net recombination of excited quasiparticles back into Cooper pairs.[3] The negative response seen in Fig. 63.37(c) may be evidence for an effective nonequilibrium recombination time of about 15 ps in YBCO. Negative transients with durations of about 30 ps have been

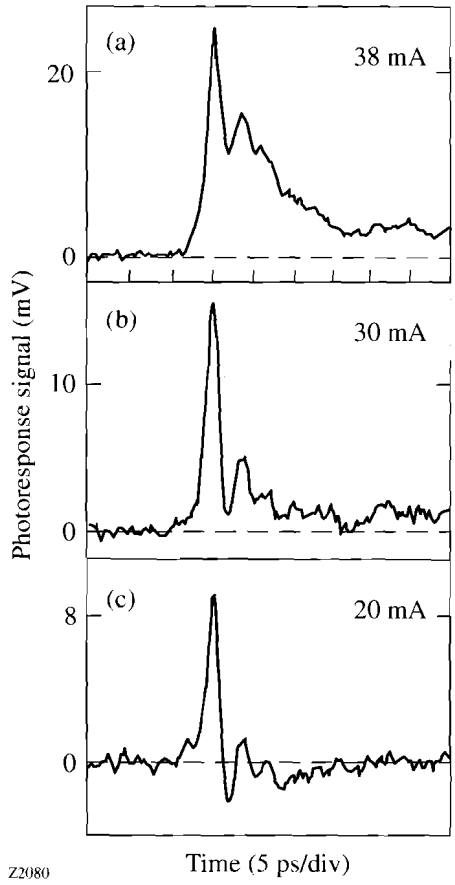

Fig. 63.37
Photoresponse signals from the 7-μm bridge of the 100-nm film for bias currents of (a) 38 mA, (b) 30 mA, and (c) 20 mA. The fluence was 15 μJ/cm^2 (P_{av} = 0.4 mW). Aside from the different bias currents, conditions were identical to those of the 15-mA case of Fig. 63.36. Notice the fast tail at high bias currents in (a) and (b), which then disappears at lower bias currents in (c). Also notice the negative component to the signal in (c).

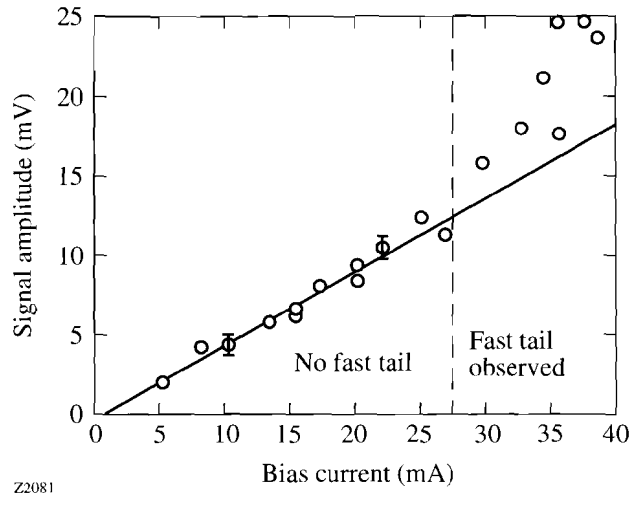

Fig. 63.38
Amplitude of the photoresponse signal (open circles) as a function of bias current for the 7-μm bridge of the 100-nm film at a fluence of 15 μJ/cm^2 (P_{av} = 0.4 mW). Above 28 mA, a fast tail is present, and the amplitude of the signal is not linear with the bias current. Below 28 mA, the fast tail disappears, and the response becomes linear with bias current. The solid line is a least-squares fit to the data below 28 mA. Error bars of ±0.5 mV are shown on two of the data points.

reported recently in photoresponse experiments on YBCO thin films using fast oscilloscopes.[7,8] The area under the negative part of the response in Fig. 63.37(c) is also approximately equal to the area under the faster positive component. This suggests that the positive transient arises mainly from a nonequilibrium (or nonbolometric) kinetic inductive mechanism,[3,5,8] as opposed to a change in the kinetic inductance arising from a purely thermal (or bolometric) response, which would not account for the observed negative transient.[6,7]

A kinetic inductive bolometric model,[6,7] however, predicts a voltage transient with an amplitude of about 30 mV and a width of 0.15-ps FWHM for the conditions given in Fig. 63.37(c). This would give a 3-mV signal after broadening to 1.5-ps FWHM, which is the same order of magnitude as the observed transient of about 9 mV. In a two-temperature nonequilibrium heating model with a ratio of phonon to electronic heat capacities of $C_{ph}/C_e = 40$ and an electron-phonon relaxation time of 1.5 ps,[13] the change in temperature ΔT_e of the electronic system is about 32 K. The electronic temperature would therefore exceed T_c, which might induce a transition in the bridge to the normal state. The resistance of the 7-μm × 100-μm × 100-nm bridge at 110 K is around 220 Ω, or about 22 Ω for a 10-μm section. At a bias current of 20 mA, this would give a voltage transient with an amplitude of 400 mV for a superconducting-to-normal-state transition, which is much larger than the observed signals.

The origin of the fast tail may be due to several mechanisms. At high bias currents (Fig. 63.37) or large fluences (not shown), where the fast tail is seen in the photoresponse signal, the time over which net pair breaking occurs may be extended, which would widen the positive response of the signal. The fast tail may also be due to fast vortex motion across the width of the bridge. Studies of flux-flow transistors have revealed vortex velocities as high as 6×10^7 cm/s.[14] The transit time across a 7-μm-wide bridge would therefore be about 12 ps, which is close to the observed fall time of about 10 ps for the fast tail. Recent studies on switching instabilities in current-biased YBCO thin films have reported lower vortex velocities

of the order of 2×10^5 cm/s,[15] which would not account for a 10-ps duration of the fast tail. Furthermore, the duration of the fast tail did not increase when a wider bridge with a width of 17 μm was used with a 10-μm laser focus. Experiments with larger beam focuses on wider bridges may be necessary to study this effect.

In conclusion, we have observed for the first time photoresponse signals less than 2 ps in duration from YBCO thin films using electro-optic sampling techniques. The picosecond transients were seen in optically thick films and at a repetition rate of 76 MHz. We believe that the fast picosecond response is due to a kinetic inductive mechanism, and that the fast tail may be due to ballistic vortex motion across the bridge. The fast response shown in this work makes YBCO films suitable for high-speed applications, e.g., as photodetectors operating above 100 GHz.

ACKNOWLEDGMENT

This work was supported by the Ontario Centre for Materials Research and the Natural Sciences and Engineering Research Council of Canada and made use of the facilities of the Centre for Electrophotonic Materials and Devices. Research in Rochester was partially supported by the Army Research Office grant DAAH04-93-G-0211. Additional support was received from the Frank Horton Graduate Fellowship Program.

REFERENCES

1. S. G. Han *et al.*, Phys. Rev. Lett. **65**, 2708 (1990); S. G. Han *et al.*, IEEE Trans. Magn. **27**, 1548 (1991).
2. T. Gong, L. X. Zheng, W. Xiong, W. Kula, Y. Kostoulas, R. Sobolewski, and P. M. Fauchet, Phys. Rev. B **47**, 14,495 (1993).
3. N. Bluzer, Phys. Rev. B **44**, 10,222 (1991); N. Bluzer, J. Appl. Phys. **71**, 1336 (1992); N. Bluzer, IEEE Trans. Appl. Supercond. **3**, 2869 (1993).
4. A. D. Semenov *et al.*, Appl. Phys. Lett. **63**, 681 (1993).
5. A. Ghis *et al.*, Appl. Phys. Lett. **63**, 551 (1993).
6. F. A. Hegmann and J. S. Preston, Phys. Rev. B **48**, 16,023 (1993).
7. F. A. Hegmann, R. A. Hughes, and J. S. Preston, Appl. Phys. Lett. **64**, 3172 (1994); F. A. Hegmann, R. A. Hughes, and J. S. Preston, in *High-Temperature Superconducting Detectors: Bolometric and Non-bolometric*, edited by M. Nahum and J.-C. Villegier (SPIE, Bellingham, WA, 1994), Vol. 2159, pp. 88–97.
8. M. A. Heusinger *et al.*, IEEE Trans. Appl. Supercond. **5**, 2595 (1995).
9. J. A. Valdmanis, G. Mourou, and C. W. Gabel, Appl. Phys. Lett. **41**, 211 (1982).
10. M. Currie, C.-C. Wang, D. Jacobs-Perkins, R. Sobolewski, and T. Y. Hsiang, IEEE Trans. Appl. Supercond. **5**, 2849 (1995).
11. D. R. Dykaar, R. Sobolewski, J. M. Chwalek, J. F. Whitaker, T. Y. Hsiang, G. A. Mourou, D. K. Lathrop, S. E. Russek, and R. A. Buhrman, Appl. Phys. Lett. **52**, 1444 (1988); M. C. Nuss *et al.*, Appl. Phys. Lett. **54**, 2265 (1989).
12. X.-H. Hu, T. Juhasz, and W. E. Bron, Appl. Phys. Lett. **59**, 3333 (1991).
13. G. N. Gol'tsman *et al.*, J. Supercond. **7**, 751 (1994); M. Lindgren *et al.*, Appl. Phys. Lett. **64**, 3036 (1994).
14. P. Bernstein *et al.*, J. Appl. Phys. **76**, 2929 (1994).
15. S. G. Doettinger *et al.*, Phys. Rev. Lett. **73**, 1691 (1994).

Magnetorheological Finishing—A Deterministic Process for Optics Manufacturing

Finish polishing of optics with magnetic media has evolved extensively over the past decade. Of the approaches conceived during this time, the most recently developed process is called magnetorheological finishing (MRF). In MRF, a magnetic field stiffens a fluid suspension in contact with a workpiece. The workpiece is mounted on the rotating spindle of a computer-numerically-controlled (CNC) machine. Driven by an algorithm for machine control that contains information about the MRF process, the machine deterministically polishes out the workpiece by removing microns of subsurface damage, smoothing the surface to a microroughness of 10 Å rms, and correcting surface figure errors to less than 0.1 μm peak-to-valley (p-v). Spheres and aspheres can be processed with the same machine setup using the appropriate machine program. This article describes MRF and gives examples that illustrate the capabilities of a pre-prototype machine located at the Center for Optics Manufacturing (COM).

Background

Finish polishing of optics is defined here to be the production of a surface to within 0.25 μm p-v of the specified figure, accompanied by sufficient material removal to eliminate subsurface damage and to achieve a microroughness of 10 Å rms. Classical finishing processes employ precisely shaped, viscoelastic pitch or polyurethane foam-faced laps to transfer pressure and velocity through an abrasive slurry to the workpiece. Material is removed by chemical and mechanical interactions among the abrasive (typically micron- to submicron-size cerium oxide or aluminum oxide), the carrier fluid (water), and the workpiece.

Strong technical and economic incentives exist for developing alternative finishing processes that use laps whose shapes are not permanently fixed, but can be controlled and changed with the application of an external field. The cost for design, manufacture, and storage of numerous fixed laps, each with a different surface curvature, would be eliminated. It would also be easy to create unique lap shapes for finishing aspheric and other nonstandard surfaces. Innovative work has been done by several research groups throughout the world to introduce magnetic media to the optics finishing process.

Magnetic media-assisted finishing has been studied in Japan for many years. In 1984, Y. Tani and K. Kawata[1] reported experiments with the geometry shown in Fig. 63.39. The principal of operation was the creation of magnetobuoyant forces that acted on nonmagnetic abrasives (silicon carbide, 4-μm diam, 40 vol.%) in a magnetic fluid (a ferrocolloid-magnetite, Fe_3O_4, 100- to 150-Å diam in eicosyl naphthalene), placed in a nonuniform magnetic field (1-kG approximate field strength). The magnetic field gradients created by a flat lap array of permanent magnets caused the abrasive grains to levitate upward into contact with the work. Motor-driven rotation of the main spindle caused the work (a set of three acrylic plates, 20 mm in diameter) to move over the abrasives that were localized in the regions of minimum magnetic field.

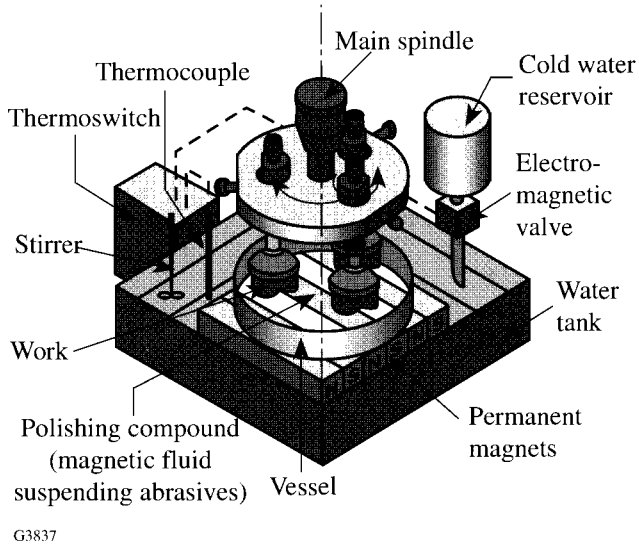

Fig. 63.39
Polishing of acrylic plates with SiC abrasives in a magnetic fluid composed of 150-Å-diam magnetite particles. The pole pieces serve as the reference lapping surface for the workpiece. (From Ref. 1.)

Material was removed at the rate of 2 μm/min across the entire part, and a 10× reduction in surface roughness to 400-Å Rmax was observed after 1 h. (Rmax denotes peak-to-valley roughness.) The authors noted significant thermal control problems in the slurry.

Related work was reported by Y. Saito *et al.* in 1987, again for acrylic plates in an aqueous-based ferrocolloid slurry.[2] Confinement of polishing abrasives to the work zone was a problem. The pressures generated by these two approaches were inadequate to polish glass, and there was no possibility for surface figure control.

Based upon work of Kurobe,[3] Suzuki *et al.*[4] made significant advances with the machine geometry shown in Fig. 63.40. By sealing the ferrocolloidal media in a brass trough with a flexible, polyurethane-rubber cover, they could direct considerably more pressure (10–25 kPa for 8–10 kG) to a colloidal silica slurry in contact with the work. It was possible to finish hard materials against a magnetically shaped polyurethane lap. Nonplanar surfaces could be polished by suitably contouring the magnet pole cap. In 1989, they reported smoothing a lithium niobate surface of 50-mm radius of curvature from 1500-Å to 100-Å Rmax (17 Å rms) in 30 min. The spherical surface figure error was reduced from 0.4 to 0.3 μm p-v.

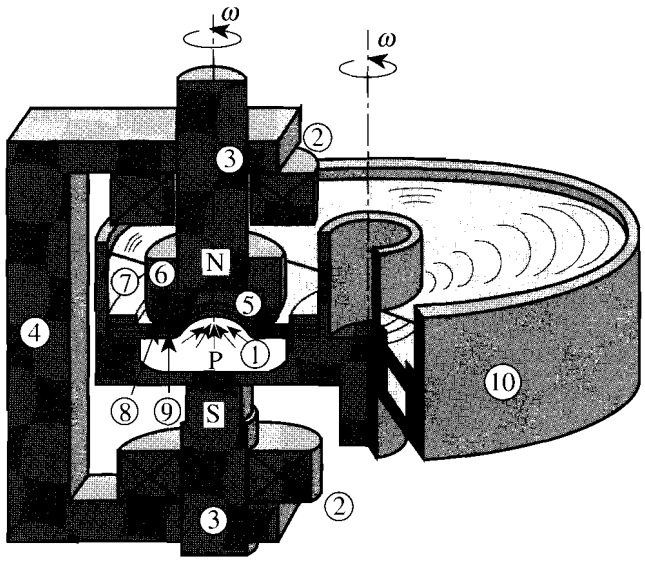

1. Magnetic fluid
2. Coil
3. Iron pole
4. Yoke
5. Workpiece
6. Jig or chuck
7. Polishing abrasive
8. Polyurethane pad
9. Rubber sheet
10. Brass vessel

G3838

Fig. 63.40
Apparatus for polishing with a pad whose shape is defined by a magnetic field acting on a confined magnetic fluid. (From Ref. 2.)

More recently, in 1993, these researchers demonstrated the ability to polish aspheric surfaces on 40-mm-diam Pyrex® glass parts with removal rates of 2 to 4 μm/h.[5] One drawback to this approach was a lack of edge control. Another serious impediment to commercialization was the need for an inventory of customized pole caps, uniquely shaped to each desired surface form.

Introduction to Magnetorheological Finishing (MRF)

The most recent approach to processing optics with magnetic fluids is magnetorheological finishing (MRF). This technology was initiated in Minsk, Belarus by Kordonski, Prokhorov, and coworkers,[6,7] as an outgrowth of work with intelligent fluids for clutches, shock absorbers, and vibration isolators. The concept of MRF is shown in Fig. 63.41. A suspension of noncolloidal magnetic particles and polishing abrasives is contained in a vessel, or trough. Rotation of the trough delivers the suspension to the surface of a spindle-mounted workpiece. With the application of a dc magnetic field in the vicinity of the workpiece, the suspension stiffens to form a small pressure spot that contacts and conforms to the workpiece. The magnetic-field-stiffened suspension constitutes a lap, and the constant flow of magnetic particles and

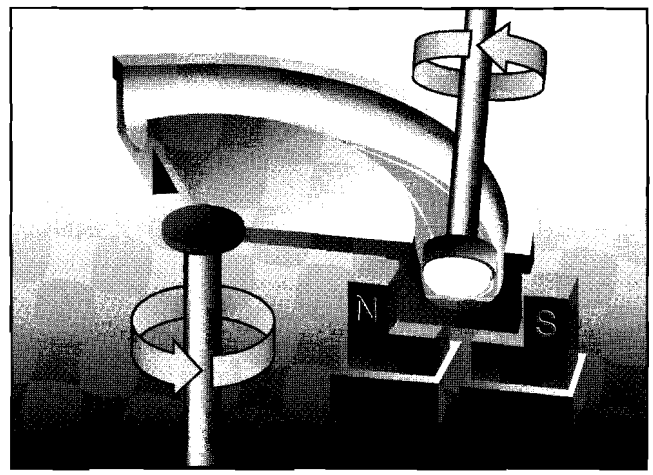

G3839

Fig. 63.41
The MRF concept. A workpiece is immersed directly into the magnetorheological suspension for processing against a magnetic-field-stiffened, fluid lap.

polishing abrasives through the region of high pressure causes material removal at the workpiece surface. A key difference between the MRF process and that of Fig. 63.40 is that in MRF material removal takes place only in the vicinity of the small pressure spot rather than simultaneously over the whole surface of the workpiece. Other unique features of the MRF process are the controllable and conformal nature of the lap, the constant replenishment of the polishing zone with fresh suspension, and the continual removal of glass particles and heat generated in the polishing process.

A workpiece is polished by sweeping its surface through the zone of high pressure. Dwell time determines the amount of material that is removed. The illustration in Fig. 63.42 gives a cut-away view of the finishing process, where a spherical surface is shown in three orientations. The lens center is polished with the spindle normal to the bottom of the trough. Rotation of the spindle about the lens center of curvature causes annular regions of increasing diameter to come into the zone of high pressure for finishing. A key to the areal removal of subsurface damage, areal smoothing, and areal figure correction is the machine program that drives spindle motion at predetermined velocities through both positive and negative angles. Spherical or aspheric surfaces can be finished with the same machine setup, using customized machine programs.

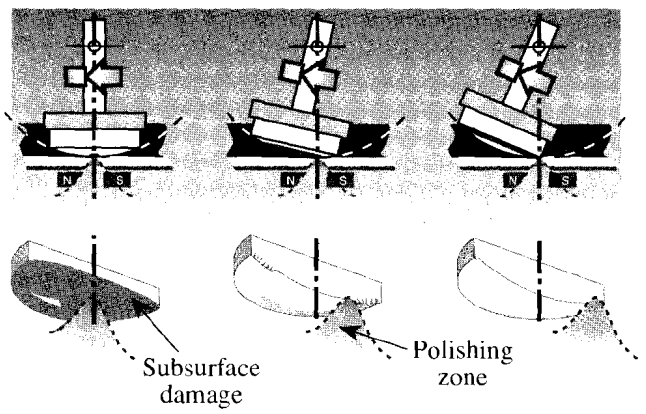

Fig. 63.42
Polishing out a workpiece with the MRF process. Dwell time determines the ultimate surface shape and smoothness.

Magnetic Suspension, Polishing "Spot," and Parameter Studies

The MR suspension consists of noncolloidal magnetic particles, ~4.5 μm in diameter, mixed in an aqueous slurry with nonmagnetic polishing abrasives (see Fig. 63.43). When circulating suspension passes into the high magnetic field (~4 kG) created by an electromagnet, the magnetic particles form chain-like structures. The result is an increase in the viscosity and yield (shear) stress of the suspension by two orders of magnitude. A localized pressure spot is formed against the surface of the workpiece, and material removal occurs as a result of chemomechanical interactions.

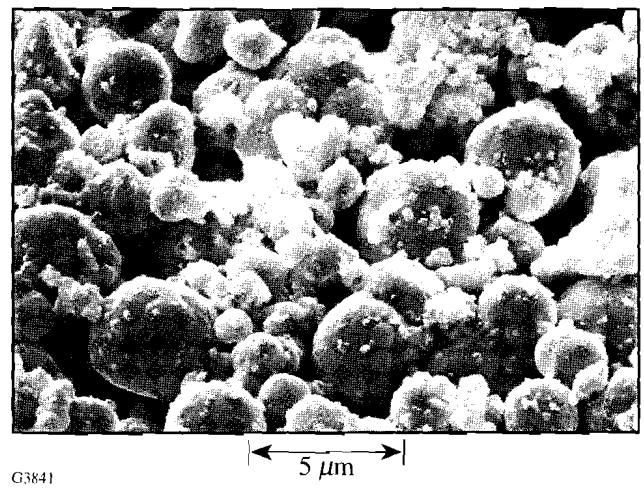

Fig. 63.43
Scanning electron micrograph of an MR suspension containing 4.5-μm (initial median size) spherical magnetic particles and 3.5-μm (initial median size) CeO_2 particles. The sample was analyzed after one week of use.

The MRF removal function in the zone of high pressure is specific to the machine platform, the magnetic field strength, the workpiece geometry, and the properties of the material being finished. All experimental results reported in this paper were obtained on a pre-prototype MRF machine whose configuration resembles that shown in Fig. 63.41. Figure 63.44 shows the fluid flow direction and removal "spot" for a 40-mm-diam BK7 glass lens with an 84-mm radius of curvature, immersed in the MR suspension for 5 s. The spindle arm was oriented at an angle of $\theta = 2°$ and was locked to prevent workpiece rotation. Interferometrically derived depth profiles show that the removal function has a backward "D" shape, with a region of peak removal at the point of deepest penetration of the lens surface into the suspension. The peak removal rate is 4.6 μm/min, and the volumetric removal rate is 0.48 mm^3/min.

Several parameter studies have been conducted to evaluate the sensitivity of the polishing spot to process parameters. There is a significant dependence upon material type. Fig-

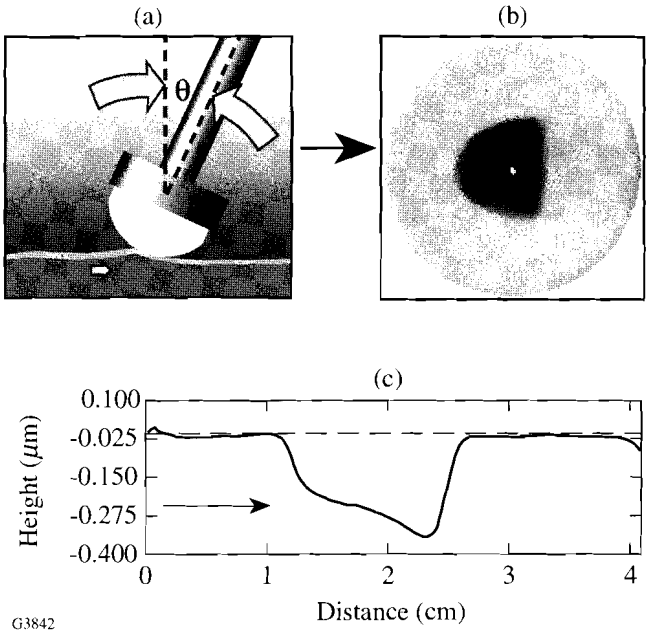

Fig. 63.44
MRF removal function on BK7 glass after 5 s. The "spot" areal size is approximately 2 × 2 cm for the conditions described in the text.

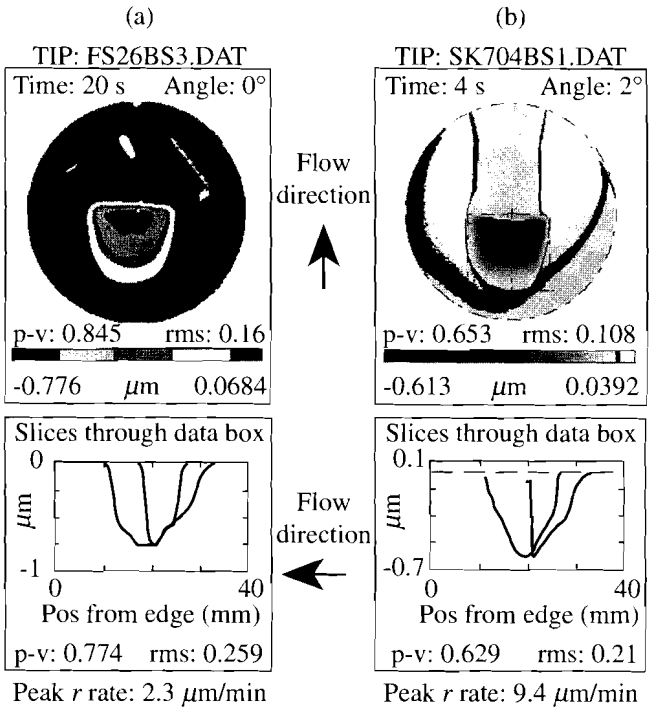

Fig. 63.45
Interferograms of removal "spots" for two different glass types under identical MR processing conditions. Depth-profile line scans shown below the spots are similar in shape.

ure 63.45 shows interferograms of spots taken on two different glass types. For the fused silica part, the spot is acquired by lowering the part into the suspension at normal incidence, turning the magnetic field on for 20 s, turning the field off, and raising the spindle-mounted part up and out of the suspension. Depth profile line scans, taken in orthogonal directions through the interferogram and displayed below the spot, give a peak removal rate of 2.3 μm/min for this glass. For the SK7 part, a spot is acquired by first turning on the magnetic field. The spindle-mounted part is then swept through an angle to the near-normal-incidence orientation in the suspension. It is kept there for a period of 4 s and then swept back out. Because of its composition and physical properties, SK7 polishes faster than fused silica. The measured peak removal rate is 9.4 μm/min. The spot shapes for these glasses are very similar. This is a characteristic of the MR process.

Figure 63.46 displays the peak and volumetric removal rates for a selection of seven optical glass types, measured under identical MR process conditions. There is a factor of nearly 4 increase in removal rate for F7 compared with fused silica (FS). The trend toward higher removal rates generally correlates with a decrease in silica content (change in chemistry of removal) and a drop in glass hardness (Knoop, Vickers, or lapping—change in mechanics of removal).

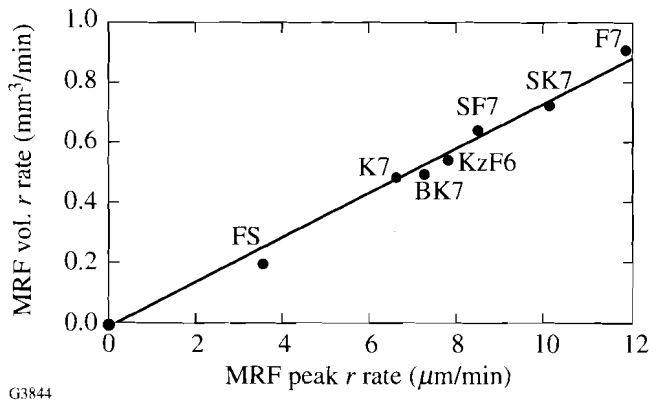

Fig. 63.46
Removal rates for several glass types under identical MR processing conditions. Softer glasses are generally seen to polish more rapidly.

Another parameter that has been studied is the sensitivity of final surface microroughness to glass type and to initial surface

microroughness. Areal polishing experiments, conducted on spherical parts generated with deterministic grinding processes[8] at COM, show that the smoothing process is more sensitive to the initial condition of the surface than to the glass type. Figure 63.47 gives the time evolution of surface microroughness for the same set of seven optical glasses (40-mm diam), measured with two different types of optical profilers. Both sets of data show that the final rms surface microroughness, independent of glass type, is ~10 Å. If the initial rms surface microroughness is less than a few hundred angstroms, smoothing occurs in 5 to 10 min. The rate of smoothing drops for rougher surface conditions.

Deterministic MR Finishing of Convex Spherical and Aspheric Surfaces

Since 1993 a pre-prototype MRF machine has been used as a testbed for the development of software that enables technical personnel (not necessarily opticians) to deterministically finish optics.[9] The software is being developed for COM by Prof. Greg Forbes, Macquarie University, Sydney, Australia, and his graduate student, Mr. Paul Dumas of The Institute of Optics, University of Rochester. Most test parts for polishing experiments are prepared primarily on Opticam® CNC ring-tool generating machines at COM, although parts have also been provided by selected companies in the U.S. and elsewhere.

The Forbes/Dumas code requires three items as input: the shape and magnitude of the MRF removal function or "spot," the initial surface shape, and the processing objectives. The first item is obtained by generating a spot on a test piece of the same material type and shape to be finished. An interferogram of the removal spot, recorded by a Zygo Mark IV xp® interferometer, is acquired and loaded into the code. Alternatively, a previously recorded and stored spot profile may be called up from a database. The second input is the initial shape of the surface to be finished, which for a spherical surface is another interferogram showing initial deviation from a best-fit sphere. For an aspheric surface the input could be a surface profile obtained with a stylus instrument like the Rank Taylor Hobsen Form Talysurf®. The third input is the processing objective, which could be dc removal to eliminate subsurface damage, figure correction, or a combination of the two.

The Forbes/Dumas code runs on a PC. Using a series of complex algorithms, the code convolves the removal function with the initial surface shape to derive an operating program for the spindle-arm angular controller on the MRF machine. The code specifies angles and accelerations for the controller, the number of sweeps required between positive and negative angles, and the total estimated processing time. Finally, the code predicts the figure expected from the process cycle. The Forbes/Dumas code and the pre-prototype MRF machine controller are best understood with several examples.

1. Convex Spherical Parts from Fused Silica

One of several convex fused-silica parts (40-mm diam, 58-mm radius of curvature), generated on the Opticam® SX, was polished in three cycles to illustrate dc removal, figure correction, and surface smoothing. Results are given in Table 63.II. The first cycle lasted 32 min, removing 3 μm uniformly from the surface and reducing the areal surface roughness from 40 Å to 8 Å p-v (unfiltered, Zygo Maxim® 3D optical profiler). Symmetric surface wavefront error was held to an increase of 0.1 μm for 3 μm of material removed. (The configuration of MRF implemented in the pre-prototype machine does not permit efficient removal of any asymmetric features.) The second cycle (see below) brought figure error down from 0.42 μm to 0.14 μm. This was accomplished in 6 min with the (radially) selective removal of ~0.7 μm of material. A third cycle was implemented to remove an additional 3 μm of material while further reducing symmetric

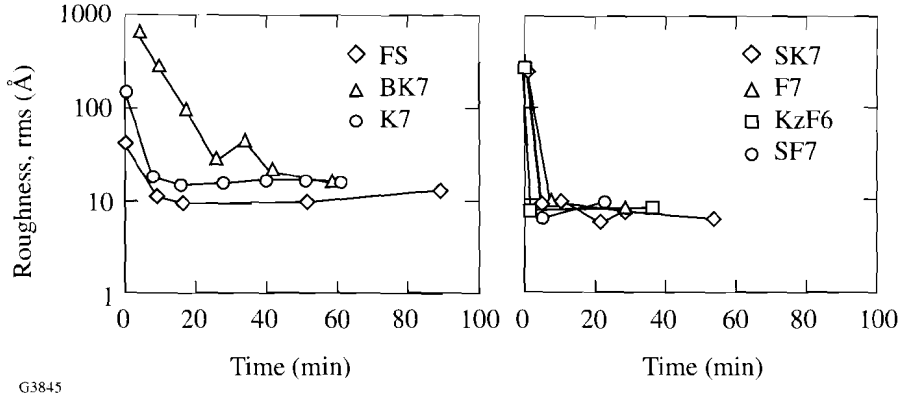

Fig. 63.47
Surface smoothing for a variety of 40-mm-diam glass parts with the same MRF process conditions. Final rms microroughness is ~10 Å. The smoothing time is 5–10 min for surfaces whose initial rms microroughness is under a few hundred angstroms.

figure error to 0.09 μm. The areal roughness remained at 8 Å rms. This is a good example of deterministic finishing.

A portion of the Forbes/Dumas user interface for cycle #2 is shown in Fig. 63.48. Interferograms for the initial, predicted, and actual surface-figure errors are shown at the top of the figure. Below each interferogram is a line scan (radial section) depicting the symmetric wavefront error compared with a best-fit sphere. This cycle removed a hole at the center of the surface.

2. Convex Spherical Parts from SK7 Glass

Other aspects of the interaction between the Forbes/Dumas code and the machine program are illustrated by the example given in Fig. 63.49. Here, a convex SK7 lens surface (40-mm diam, 58-mm radius of curvature) is processed in a figure

Table 63.II: Summary of results for MR finishing of a convex fused silica part in three process cycles.

Cycle	Amount removed (μm)	Duration (min)	Figure error* (μm p-v)	Areal roughness** (Å rms)
Initial	—	—	0.31	40
#1: dc removal/smoothing	3.0	32	0.42	8
#2: figure correction	0.7	6	0.14	7
#3: dc removal/figure correction	3.0	42	0.09	8
*Symmetric **0.25 mm^2, unfiltered				

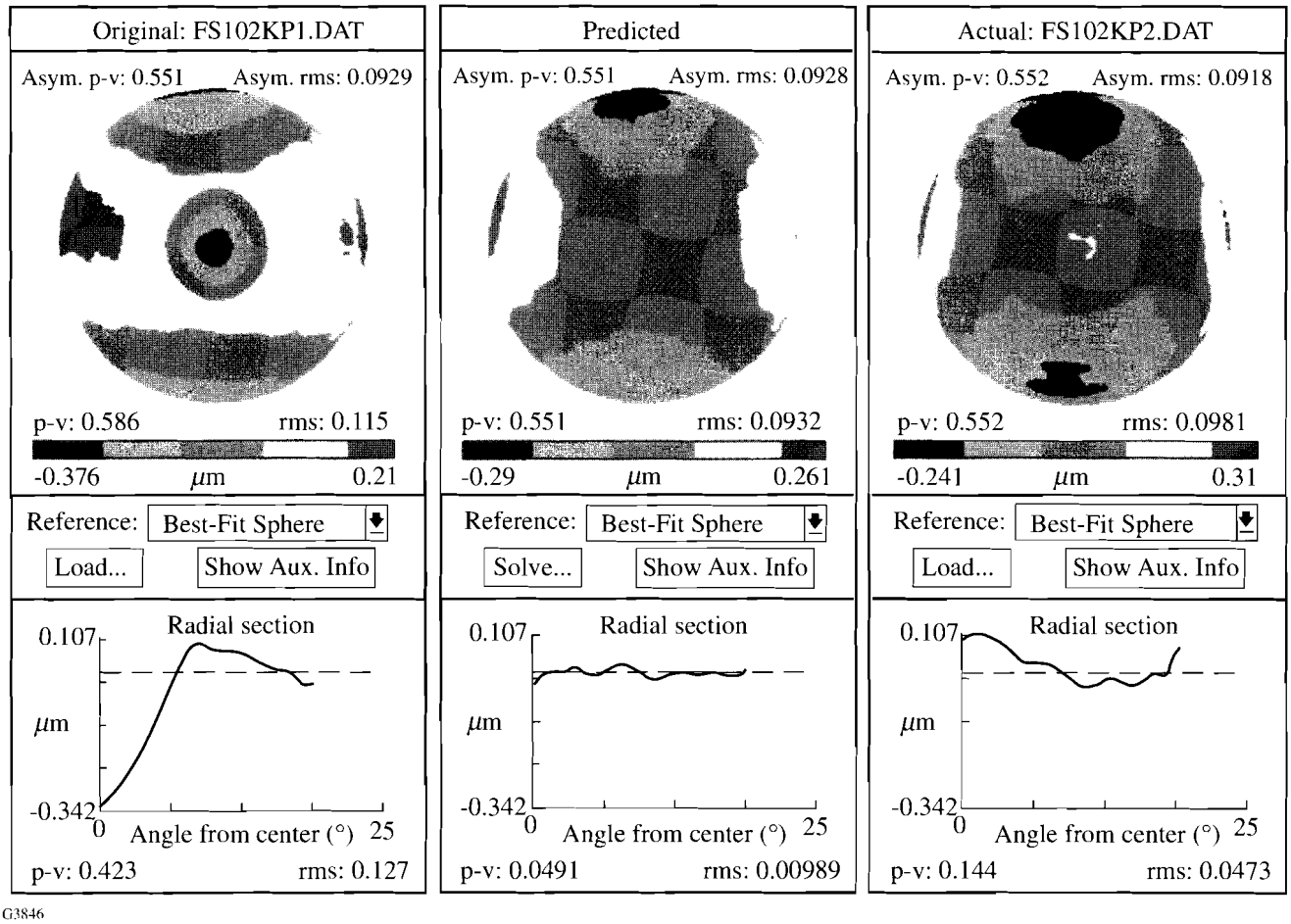

G3846

Fig. 63.48
Initial, predicted, and actual results for a ~6-min figure-correction cycle. The central hole was removed.

correction cycle. The left column shows a (symmetric) radial section of the initial surface, indicating a hill or bump in the part relative to the best-fit sphere. Directly below is a (symmetric) radial removal contour, calculated by the code, for correcting the figure error. It indicates that approximately 0.6 μm of material must be removed, primarily at the center of the part, in order to reduce the p-v wavefront error (0.334 μm) to that shown in the prediction at the top of the middle column (0.052 μm). The machine control program required to perform this operation is shown graphically at the bottom of the middle column. The curve indicates the angular velocities (1 mrfs = 0.01°/s) to be programmed into the MRF machine spindle controller for one sweep of the part through the suspension. Information is provided at the bottom of the right column on the duration of the correction run (1.2 min) and the number of angular sweeps or scans (2). Actual results from this cycle are shown at the top of the right column. Results (0.07 μm) agree well with the prediction, both in amplitude and shape. This is another good example of deterministic finishing with MRF.

3. Asphere Polishing Experiment

COM and Texas Instruments (TI) are collaborating to demonstrate deterministic manufacturing of aspheric optical elements. In a recent experiment ten BK7 lenses were manufactured using the Opticam® SM at TI for generating and the pre-prototype MRF machine at the COM for finishing. The test parts were plano-convex aspheres (hyperboloids), 47 mm in diameter, with 140 μm of aspheric departure (see Fig. 63.50). The aspheric surface figure requirement was 0.93 μm p-v, with a 0.1% tolerance on base radius. Machined parts received at COM had residual form errors ranging from 4 μm to 20 μm p-v. Initial surface roughness values were as high as 10,000 Å rms.

Finishing the parts to final figure was accomplished in two MRF cycles. Subsurface damage was removed and smoothing was performed in the first cycle. Remaining figure errors were usually corrected in a second cycle. Results for one lens are given in Fig. 63.51. Process conditions/results for each cycle

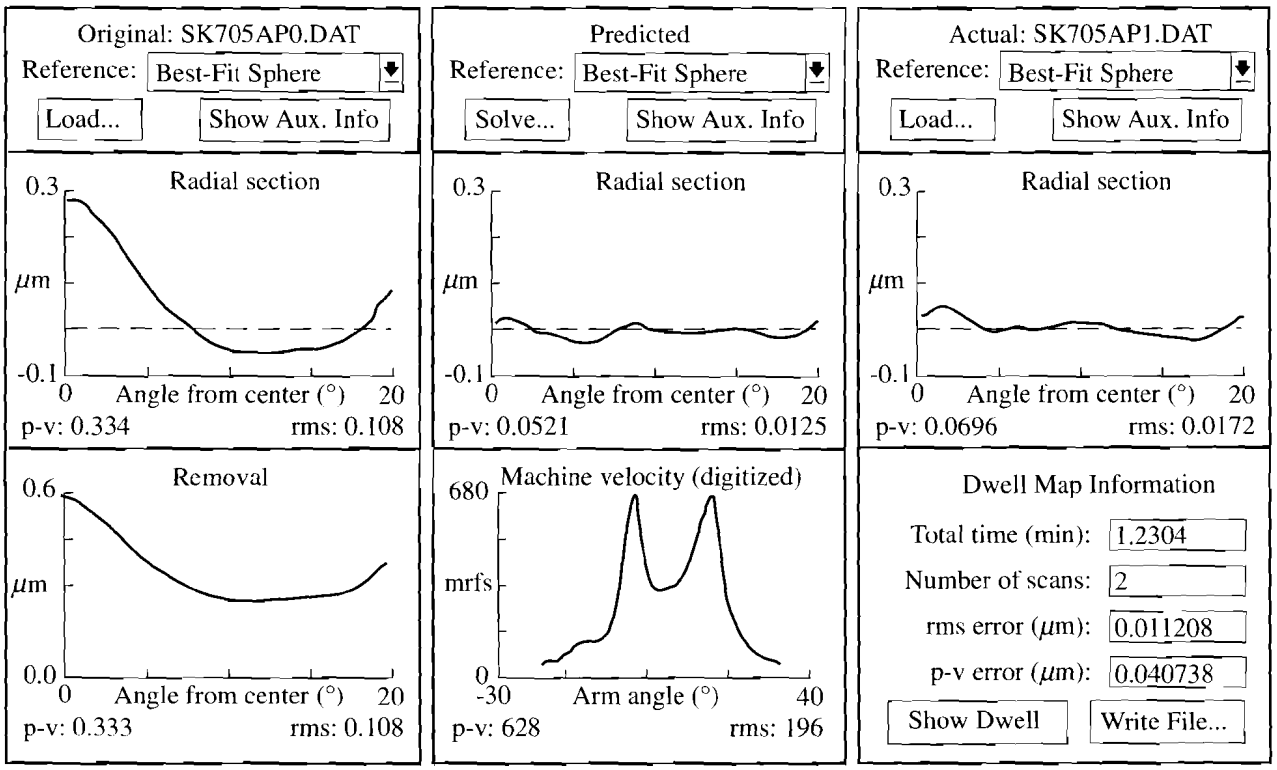

Fig. 63.49
Details of Forbes/Dumas code for spherical figure correction. An MRF machine control program is generated along with the prediction for surface shape errors. After a 1.2-min running cycle, the actual p-v figure error of 0.07 μm shows excellent agreement with the prediction of 0.05 μm, both in form and amplitude.

are indicated on the left and relevant Form Talysurf® scans on the right. In the first MRF cycle, 12 μm of material were removed over a period of 100 min. The rms roughness was reduced from 9400 Å to 10 Å. All subsurface damage was eliminated. (HF acid etching on identical parts confirms that MRF does not introduce new subsurface damage.) The second figure correction run required 40 min of polishing time; 4 μm of material were removed. At the conclusion of this cycle the form error was reduced to 0.86 μm. These BK7 lenses were returned to TI and judged acceptable for inclusion in a breadboard of their deformable mirror device assembly, an integral part of TI's digital imaging technology.

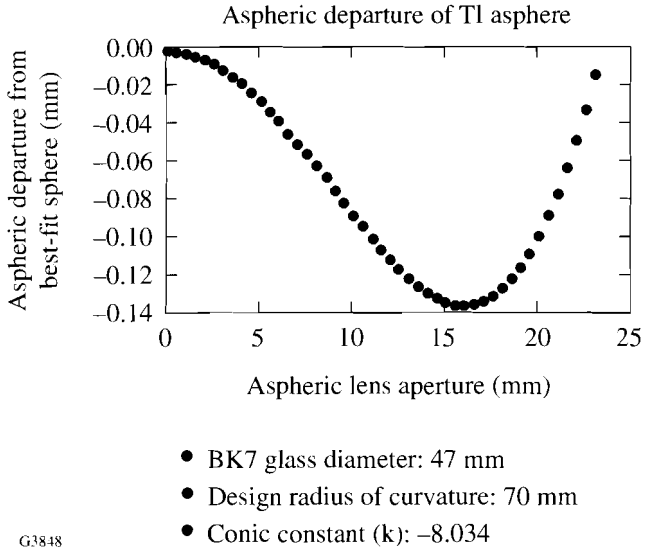

Fig. 63.50
Aspheric shape required for a collaborative deterministic manufacturing experiment with Texas Instruments.

Summary

MRF is a promising new optics manufacturing technology. Fundamental to this technology is an environmentally safe, aqueous suspension of magnetic particles and polishing abrasives, whose viscosity is increased by orders of magnitude in a magnetic field. The stiffened suspension acts as a "spot" lap that conforms to and polishes out the surface of a workpiece immersed in it. In initial trials on a pre-prototype machine, MRF has shown an excellent capability for smoothing ground glass surfaces, correcting figure errors, and eliminating subsurface damage. Experiments have demonstrated that, with machine-control programs generated by a computer algorithm, both spheres and aspheres can be finished with the same machine setup, for a variety of optical glasses.

ACKNOWLEDGMENTS

This work was carried out in collaboration with D. Golini and Y. Hsu of COM and with W. I. Kordonski, I. V. Prokhorov, E. Fess, D. Pietrowski, and V. W. Kordonski of Byelocorp Scientific, Inc. The authors acknowledge the expertise, dedication, and teamwork of Chris Dewever, Paul Dumas, Greg Forbes, Gennady Gorodkin, John Schaefer, Alan Tittle, and John Vakiner. Support for this effort was provided by Byelocorp Scientific, Inc. and the U.S. Army Materiel Command. Additional support was received from the Frank J. Horton Fellowship Program at the Laboratory for Laser Energetics. The pre-prototype MRF machine was manufactured for COM by CNC Systems, Inc., Ontario, NY.

Cycle	Amount removed (μm)	Cycle time (min)	rms* roughness (Å)	p-v fig. (μm)
Initial	---	---	9400	6.42
#1: dc ssd removal/ smoothing	12	100	10	4.40
#2: figure correction	4	40	10	0.86

*Zygo New View®, 20x Mirau

G3849

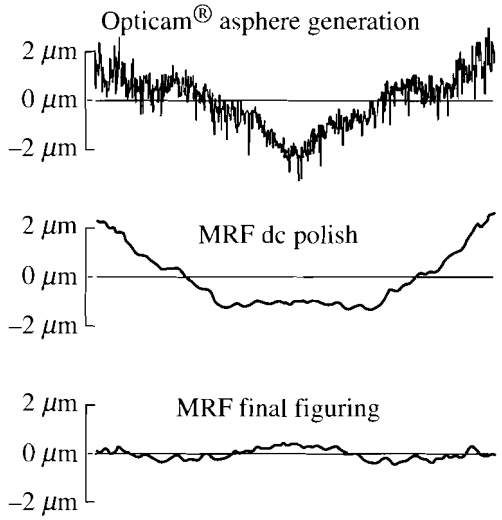

Fig. 63.51
Finishing of a 47-mm-diam asphere in two MR processing cycles. The entire polishing and figuring operation required 140 min of machine time.

REFERENCES

1. Y. Tani and K. Kawata, CIRP Annals **33**, 217 (1984).
2. Y. Saito *et al.*, in the *Proceedings of the 6th International Conference on Production Engineering Osaka* (1987), pp. 335–340.
3. T. Kurobe, O. Imanaka, and S. Tachibana, Bull. Jpn. Soc. Precis. Eng. **17**, 49 (1983).
4. H. Suzuki *et al.*, Prec. Eng. **4**, 197 (1989).
5. H. Suzuki *et al.*, J. Jpn. Soc. Precis. Eng. **59**, 1883 (1993).
6. W. I. Kordonsky, in the *Third International Conference on Adaptive Structures*, edited by B. Wada, M. Natori, and E. Breitbach (Technomic, Lancaster, PA, 1993), pp. 13–27.
7. I. V. Prokhorov, W. I. Kordonsky, L. K. Gleb, G. R. Gorodkin, and M. L. Levin, in *OSA Optical Fabrication and Testing Workshop*, 1992 Technical Digest Series, Vol. 24 (Optical Society of America, Washington, DC, 1992), pp.134–136.
8. D. Golini and W. Czajkowski, *Laser Focus World*, July 1992, 146.
9. W. I. Kordonsky, I. V. Prokhorov, B. E. Kashevsky, S. D. Jacobs, B. E. Puchebner, Y. Hsu, D. Pietrowski, D. Strafford, and E. Fess, in *OSA Optical Fabrication and Testing Workshop*, 1994 Technical Digest Series, Vol. 13 (Optical Society of America, Washington, DC, 1994), pp.104–109.

Publications and Conference Presentations

Publications

T. R. Boehly, R. S. Craxton, T. H. Hinterman, J. H. Kelly, T. J. Kessler, S. A. Kumpan, S. A. Letzring, R. L. McCrory, S. F. B. Morse, W. Seka, S. Skupsky, J. M. Soures, and C. P. Verdon, "The Upgrade to the OMEGA Laser System," Rev. Sci. Instrum. **66**, 508 (1995).

X. D. Cao, L. Zheng, and D. D. Meyerhofer, "Measurement of Group-Velocity Walk-Off of Short Pulses in Nonlinear Crystals: A Novel Method," Opt. Lett. **20**, 392 (1995).

M. J. Cumbo, D. Fairhurst, S. D. Jacobs, and B. E. Puchebner, "The Effect of Chemically Modulated Surface Charge in the Polishing of Optical Glass," in *Optical Fabrication and Testing Workshop*, Vol. 13, 1994 OSA Technical Digest Series (Optical Society of America, Washington, DC, 1994), pp. 134–137.

M. Currie, C.-C. Wang, D. Jacobs-Perkins, R. Sobolewski, and T. Y. Hsiang, "An Optoelectronic Testing System of Rapid, Single-Flux Quantum Circuits," IEEE Trans. Appl. Supercond. **5**, 2849 (1995).

J. D. B. Featherstone, N. A. Barrett-Vespone, D. Fried, Z. Kantorowitz, J. Lofthouse, and W. Seka, "Rational Choice of Laser Conditions for Inhibition of Caries Progression," in *Lasers in Dentistry* (SPIE, Bellingham, WA, 1995), Vol. 2394, pp. 57–67.

D. Fried, R. E. Glena, J. D. B. Featherstone, and W. Seka, "Multiple Pulse Irradiation of Dental Hard Tissues at CO_2 Laser Wavelengths," in *Lasers in Dentistry* (SPIE, Bellingham, WA, 1995), Vol. 2394, pp. 41–50.

P. D. Funkenbusch, Y. Y. Zhou, C. Lohnes, D. J. Quesnel, S. D. Jacobs, B. E. Puchebner, D. Golini, and A. Lindquist, "Deterministic Microgrinding of Glass with Polycrystalline Diamond Tools," in *Optical Fabrication and Testing Workshop*, Vol. 13, 1994 OSA Technical Digest Series (Optical Society of America, Washington, DC, 1994), pp. 36–39.

D. Gupta, W. R. Donaldson, and A. M. Kadin, "Transient Flux Dynamics in Optically Irradiated YBCO Thin-Film Switches," IEEE Trans. Appl. Supercond. **5**, 1371 (1995).

S. D. Jacobs, "Finish Polishing of Optics with Magnetic Media," in *International Progress in Precision Engineering*, edited by M. Bonis *et al.* (Elsevier, 1995), pp. 357–360 (invited).

S. D. Jacobs, D. Golini, Y. Hsu, B. E. Puchebner, D. Strafford, W. I. Kordonsky, I. V. Prokhorov, E. Fess, D. Pietrowski, and V. W. Kordonsky, "Magnetorheological Finishing: Toward Cylinders, Toroids, and Aspheric Optics," in *International Progress in Precision Engineering*, edited by M. Bonis *et al.* (Elsevier, 1995), pp. 371–374.

W. I. Kordonsky, I. V. Prokhorov, B. E. Kashevsky, S. D. Jacobs, B. E. Puchebner, Y. Hsu, D. Pietrowski, and D. Stafford, "Basic Properties of Magnetorheological Fluids for Optical Finishing," in *Optical Fabrication and Testing Workshop*, Vol. 13, 1994 OSA Technical Digest Series (Optical Society of America, Washington, DC, 1994), pp. 104–106.

W. I. Kordonsky, I. V. Prokhorov, S. D. Jacobs, B. E. Puchebner, Y. Hsu, D. Pietrowski, and D. Stafford, "Glass Polishing Experiments Using Magnetorheological Fluids," in *Optical Fabrication and Testing Workshop*, Vol. 13, 1994 OSA Technical Digest Series (Optical Society of America, Washington, DC, 1994), pp. 107–109.

W. Kula, W. Xiong, R. Sobolewski, and J. Talvacchio, "Laser Patterning of $YBa_2Cu_3O_x$ Thin Films Protected by *In-Situ* Grown $SrTiO_3$ Cap Layers," IEEE Trans. Appl. Supercond. **5**, 1177 (1995).

W. Lang, G. Heine, W. Kula, and R. Sobolewski, "Superconducting Fluctuations in $Bi_2Sr_2Ca_2Cu_3O_x$ Thin Films: Paraconductivity, Excess Hall Effect, and Magnetoconductivity," Phys. Rev. B **51,** 9180 (1995).

Y. Lin, T. J. Kessler, and G. Lawrence, "Distributed Phase Plates for Supergaussian Focal-Plane Irradiance Profiles," Opt. Lett. **20**, 764 (1995).

J. C. Mastrangelo, T. N. Blanton, and S.-H. Chen, "Crystallization upon Thermal Annealing of a Glass-Forming Liquid Crystal in the Nematic Regime," Appl. Phys. Lett. **66**, 2212 (1995).

C. J. McKinstrie, R. Betti, R. E. Giacone, T. Kolber, and E. J. Turano, "Two-Dimensional Stimulated Raman Scattering of Short Laser Pulses," Phys Rev. E **51**, 3752 (1995).

W. Ng, B. E. Puchebner, and S. D. Jacobs, "Evaluation of Bound Abrasive Media for Fabrication of Ring Tool Polishers," in *Optical Fabrication and Testing Workshop,* Vol. 13, 1994 OSA Technical Digest Series (Optical Society of America, Washington, DC, 1994), pp. 114–116.

B. E. Puchebner, A. Feltz, W. Ng, and S. D. Jacobs, "Coolant Performance in Bound Diamond Ring Tool Grinding of K7 Optical Glass," in *Optical Fabrication and Testing Workshop,* Vol. 13, 1994 OSA Technical Digest Series (Optical Society of America, Washington, DC, 1994), pp. 40–43.

B. E. Puchebner, A. Feltz, and S. Patterson, "The Effect of Additives in a Commercial Coolant on the Glass Grinding Process," in *Optical Fabrication and Testing Workshop,* Vol. 13, 1994 OSA Technical Digest Series (Optical Society of America, Washington, DC, 1994), p. 44.

W. Seka, D. Fried, J. D. B. Featherstone, and S. F. Borzillary, "Light Deposition in Dental Hard Tissue and Simulated Thermal Response," J. Dent. Res. **74**, 1086 (1995).

W. Seka, D. Fried, J. D. B. Featherstone, and R. E. Glena, "Time-Dependent Reflection and Surface Temperatures during CO_2 Laser Irradiation of Dental Hard Tissues with 100-Microsecond Pulses," in *Proceedings of Lasers in Dentistry* (SPIE, Bellingham, WA, 1995), Vol. 2394, pp. 51–56.

H. Shi and S.-H. Chen, "Novel Glass-Forming Liquid Crystals. II. Systems Containing 1-phenyl-2-(6-cyanonaphth-2-yl) ethyne as a High Optical Birefringence Moiety," Liq. Cryst. **18**, 733 (1995).

M. D. Skeldon, "Transverse Modulational Instabilities in the Presence of Stimulated Rotational Raman Scattering with a High-Energy Laser," Opt. Lett. **20**, 828 (1995).

R. Sobolewski and T. Y. Hsiang, "Progress in Ultrafast Superconducting Electronics," in *Superconductivity and Particle Detection,* edited by T. A. Girard, A. Morales, and G. Waysand (World Scientific, Singapore, 1995), pp. 279–289 (invited).

C.-C. Wang, M. Currie, and T. Y. Hsiang, "Ultrafast, Integrable, Optics-Based Interface between Superconducting and Room-Temperature Electronics," IEEE Trans. Appl. Supercond. **5**, 3156 (1995).

C.-C. Wang, M. Currie, D. Jacobs-Perkins, M. J. Feldman, R. Sobolewski, and T. Y. Hsiang, "Optoelectronic Generation and Detection of Single-Flux-Quantum Pulses," Appl. Phys. Lett. **66**, 3325 (1995).

M. Yu, G. P. Agrawal, and C. J. McKinstrie, "Pump-Wave Effects on the Propagation of Noisy Signals in Nonlinear Dispersive Media," J. Opt. Soc. Am. B **12**, 1126 (1995).

L. Zheng and D. D. Meyerhofer, "Cross-Correlation Technique for Single-Shot Measurements of Weak Light Pulses," Opt. Lett. **20**, 407 (1995).

Forthcoming Publications

R. Adam, W. Kula, and R. Sobolewski, "Laser-Induced Modification of Transport Properties of Y-Ba-Cu-O Step-Edge Weak Links," to be published in Applied Physics Letters.

M. S. Adams, M. V. Fedorov, V. P. Krainov, and D. D. Meyerhofer, "Comparison of Quasiclassical and Exact Dipole Moments for Bound-Free Transitions in Hydrogen," to be published in Physical Review A.

R. Betti, V. N. Goncharov, R. L. McCrory, and C. P. Verdon, "Self-Consistent Cutoff Wave Number of the Ablative Rayleigh-Taylor Instability," to be published in Physics of Plasmas.

T. R. Boehly, R. S. Craxton, T. H. Hinterman, P. A. Jaanimagi, J. H. Kelly, T. J. Kessler, R. L. Kremens, S. A. Kumpan, S. A. Letzring, R. L. McCrory, S. F. B. Morse, W. Seka, S. Skupsky, J. M. Soures, and C. P. Verdon, "The Upgrade to the OMEGA Laser System," to be published in the Proceedings of the American Nuclear Society and the Proceedings of IAEA, Paris, France, 14–18 November 1994.

X. D. Cao and D. D. Meyerhofer, "Optimization of Pulse Shaping Using Nonlinear Polarization Rotation," to be published in Optics Communications.

S.-H. Chen, J. C. Mastrangelo, H. Shi, A. Bashir-Hashemi, J. Li, and N. Gelber, "Novel Glass-Forming Materials Based on Adamantane with Pendant Cholesteryl, Disperse Red 1, and Nematogenic Groups," to be published in Macromolecules.

S.-H. Chen, H. Shi, J. C. Mastrangelo, and T. N. Blanton, "Design, Synthesis, and Stability of Organic Glasses for Advanced Optical Applications," to be published in Polymer Preprints, American Chemical Society.

C. T. Cotton, "The Design of an All-Spherical, Three-Mirror, Off-Axis Telescope Objective," to be published in the OSA Proceedings of the International Optical Design Conference '94, Rochester, NY.

M. J. Cumbo, D. Fairhurst, S. D. Jacobs, and B. E. Puchebner, "Slurry Particle Size Evolution during the Polishing of Optical Glass," to be published in Applied Optics.

P. M. Fauchet, L. Tsybeskov, C. Peng, S. P. Duttagupta, J. von Behren, Y. Kostoulas, J. V. Vandyshev, and K. D. Hirshman, "Light-Emitting Porous Silicon: Materials Science, Properties, and Device Applications," to be published in IEEE Journal of Selected Topics in Quantum Electronics.

D. Fried, R. E. Glena, J. D. B. Featherstone, and W. Seka, "Permanent and Transient Changes in the Reflectance of CO_2 Laser-Irradiated Dental Hard Tissues at λ = 9.3, 9.6, 10.3, and 10.6 μm and at Fluences between 1–20 J/cm^2," to be published in Lasers in Surgery and Medicine.

R. E. Giacone, C. J. McKinstrie, and R. Betti, "Angular Dependence of Stimulated Brillouin Scattering in Homogeneous Plasma," to be published in Physics of Plasmas.

V. N. Goncharov and R. Betti, "Growth Rate of the Ablative Rayleigh-Taylor Instability for Indirect-Drive ICF," to be published in Physics of Plasmas.

D. Gupta, W. R. Donaldson, and A. M. Kadin, "Rapid Flux Motion and Critical State Dynamics in a Superconducting Disk," to be published in the Journal of Applied Physics.

J. Hecht, D. Ofer, U. Alon, D. Shvarts, S. A. Orszag, and R. L. McCrory, "Three-Dimensional Simulations and Analysis of the Nonlinear Stage of the Rayleigh-Taylor Instability," to be published in Laser and Particle Beams.

F. A. Hegmann, D. Jacobs-Perkins, S. H. Moffat, C.-C. Wang, R. A. Hughes, M. Currie, P. M. Fauchet, T. Y. Hsiang, J. S. Preston, and R. Sobolewski, "Electro-Optic Sampling of Picosecond Photoresponse Signals from $YBa_2Cu_3O_{7-\delta}$ Thin Films," to be published in Applied Physics Letters.

S. D. Jacobs, D. Golini, Y. Hsu, B. E. Puchebner, D. Strafford, W. I. Kordonsky, I. V. Prokhorov, E. Fess, D. Pietrowski, and V. W. Kordonsky, "Magnetorheological Finishing: A Deterministic Process for Optics Manufacturing," to be published in the Proceedings of the International Conference on Optical Fabrication and Testing (SPIE Vol. 2576) (invited).

E. M. Korenic, S. D. Jacobs, S. M. Faris, and L. Li, "Cholesteric Liquid Crystal Inks and Paints," to be published in Research Highlights of the Army Research Office Physics Division.

Y. Kostoulas, K. B. Ucer, L. Waxer, G. W. Wicks, I. A. Walmsley, and P. M. Fauchet, "Ultrafast Carrier Lifetime in Low-Temperature-Grown GaAs, InP, and InGaP," to be published in the Proceedings of LEOS '94 7th Annual Meeting, Boston, MA, 31 October–3 November 1994.

W. Kula, R. Adam, and R. Sobolewski, "Y-Ba-Cu-O Thin-Film Structures with a Nonuniform In-Depth Oxygen Concentration Profile," to be published in the Institute of Physics Conference Series.

W. Lang, W. Göb, W. Kula, and R. Sobolewski, "Anisotropic Magnetoresistance in the Normal State of Oxygen-Deficient $YBa_2Cu_3O_{7-\delta}$ Thin Films Induced by Superconducting Fluctuations," to be published in Zeitschrift Für Physik B.

R. S. Marjoribanks, F. W. Budnik, H. Chen, and D. D. Meyerhofer, "Plasma Electron Temperature in Picosecond Laser Plasmas from Quasi-Steady Ratio of Isoelectronic Lines," to be published in the Journal of the Optical Society of America B.

K. L. Marshall, S. D. Jacobs, and J. E. Miller, "Midinfrared Modulation through the Use of Field-Induced Scattering in Ferroelectric Liquid Crystals," to be published in Applied Optics.

J. C. Mastrangelo, T. N. Blanton, and S.-H. Chen, "Morphology and Its Stability of Cyclohexane and Biocyclooctene Rings Containing Pendant Disperse Red 1," to be published in Chemistry of Materials.

R. L. McCrory, "Progress Toward Ignition with Direct-Drive," to be published in Concerning Major Systems in Science and Technology.

R. L. McCrory, J. M. Soures, C. P. Verdon, T. R. Boehly, D. K. Bradley, R. S. Craxton, J. A. Delettrez, R. Epstein, P. A. Jaanimagi, S. D. Jacobs, R. L. Keck, J. H. Kelly, T. J. Kessler, H. Kim, J. P. Knauer, R. L. Kremens, S. A. Kumpan, S. A. Letzring, F. J. Marshall, P. J. McKenty, S. F. B. Morse, A. Okishev, W. Seka, R. W. Short, M. D. Skeldon, S. Skupsky, M. Tracy, and B. Yaakobi, "Direct-Drive Laser Fusion Experimental Program at the University of Rochester Laboratory for Laser Energetics," to be published in the Proceedings of the Conference on Plasma Physics and Controlled Nuclear Fusion Research, Madrid, Spain, September 1994.

C. J. McKinstrie and E. A. Startsev, "Wave Propagation in a Drifting Plasma," to be published in Physics of Plasmas.

D. D. Meyerhofer, J. P. Knauer, S. J. McNaught, and C. I. Moore, "Observation of Relativistic Quiver Effects during High-Intensity Laser-Electron Interactions," to be published in the Journal of the Optical Society of America B.

S. S. Papernov and A. W. Schmid, "A Comparison of Laser-Induced Damage Morphology in Three Model Thin-Film Systems: HfO_2, Y_2O_3, and Ta_2O_5," to be published in the Proceedings of the XXVI Annual Symposium on Optical Materials for High Power Lasers, Boulder, CO, October 1994.

J. Peatross and D. D. Meyerhofer, "Intensity-Dependent Atomic-Phase Effects in High-Order Harmonic Generation," to be published in Physical Review A.

J. Z. Roach, A. Ninkov, S. W. Swales, and T. Morris, "Design and Evaluation of a Screen CCD Imaging System," to be published in Optical Engineering.

H. Shi and S.-H. Chen, "Dynamic Mechanical Properties of Cyclohexane-Based Glass-Forming Liquid Crystals and a Linear Side-Chain Polymer Analogue," to be published in Liquid Crystals.

H. Shi and S.-H. Chen, "Effects of Stereochemistry, Mesogenic Core, and Space Length on Crystallization from Nematic and Isotropic Melts of Cyclohexane-Based, Glass-Forming Liquid Crystals," to be published in Liquid Crystals.

H. Shi and S.-H. Chen, "Novel Glass-Forming Liquid Crystals. III. Helical Sense and Twisting Power in Chiral Nematic Systems," to be published in Liquid Crystals.

D. Shvarts, U. Alon, D. Ofer, R. L. McCrory, and C. P. Verdon, "Nonlinear Evolution of Multimode Rayleigh-Taylor Instability in Two and Three Dimensions," to be published in Physics of Plasmas.

A. Simon, "Parametric Excitation of Bernstein Modes in Laser-Produced Plasma," to be published in Physics of Plasmas.

C. J. Twomey, T. N. Blanton, K. L. Marshall, S. H. Chen, and S. D. Jacobs, "Some Dynamic Features of the Preparation of

Liquid Crystalline Elastomers," to be published in Liquid Crystals.

C. P. Verdon and R. L. McCrory, "Direct-Drive Capsule Physics," to be published in the Proceedings of ECLIM '94, Oxford, England, September 1994.

C.-C. Wang, M. Currie, D. Jacobs-Perkins, L. Shi, and T. Y. Hsiang, "Picosecond Cryogenic Nb/Si/Nb Metal-Semiconductor-Metal (MSM) Photodiode on Superconducting Microstrip Transmission Lines," to be published in IEEE Transactions on Applied Superconductivity.

C.-C. Wang, M. Currie, D. Jacobs-Perkins, R. Sobolewski, T. Y. Hsiang, and M. J. Feldman, "Electro-Optic Measurements of Single-Flux Quantum Pulses," to be published in the Institute of Physics Conference Series.

C.-C. Wang, M. Currie, R. Sobolewski, and T. Y. Hsiang, "Subpicosecond Electrical Pulse Generation by Edge Illumination of Silicon and Indium Phosphide Photoconductive Switches," to be published in Applied Physics Letters.

M. D. Wittman, R. Q. Gram, H. Kim, C. K. Immesoete, S. G. Noyes, and S. Scarantino, "Increased Retention Time for Hydrogen and Other Gases by Polymer Shells Using Optically Transparent Aluminum Layers," to be published in the Journal of Vacuum Science and Technology.

W. Xiong, Y. Kostoulas, X. Weng, P. M. Fauchet, and R. Sobolewski, "Femtosecond Study of the Electronic Structure in Semiconducting Y-Ba-Cu-O," to be published in Physical Review B.

B. Yaakobi, D. Shvarts, R. Epstein, and Q. Qu, "X-Ray Backlighting Imaging of Mixed Imploded Targets," to be published in the Journal of Applied Physics.

M. Yu, G. P. Agrawal, and C. J. McKinstrie, "Effects of the Residual Dispersion in the Phase-Conjugation Fiber on Dispersion Compensation in Optical Communication Systems," to be published in IEEE Photonics Technology Letters.

M. Yu, C. J. McKinstrie, and G. P. Agrawal, "Modulational Instabilities in Dispersion-Flattened Fibers," to be published in Physical Review E.

X. Zhou, S. Alexandrou, and T. Y. Hsiang, "Monte Carlo Investigation of the Mechanism of Subpicosecond Pulse Generation by Nonuniform Gap Illumination," to be published in Applied Physics Letters.

J. D. Zuegel and W. Seka, "Direct Measurement of $^4I_{11/2}$ Terminal-Level Lifetime in Nd:YLF," to be published in the IEEE Journal of Quantum Electronics.

J. D. Zuegel and W. Seka, "Direct Measurements of Lower-Level Lifetime in Nd:YLF," to be published in the Bulletin of the American Physical Society.

Conference Presentations

P. M. Fauchet, J. von Behren, K. B. Ucer, and Y. Kostoulas, "Ultrafast Carrier Dynamics in Porous Silicon," QELS '95, Baltimore, MD, 21–26 May 1995.

R. L. McCrory, J. M. Soures, C. P. Verdon, T. R. Boehly, D. K. Bradley, R. S. Craxton, J. A. Delettrez, R. Epstein, P. A. Jaanimagi, S. D. Jacobs, R. L. Keck, J. H. Kelly, T. J. Kessler, H. Kim, J. P. Knauer, R. L. Kremens, S. A. Kumpan, S. A. Letzring, F. J. Marshall, P. W. McKenty, S. F. B. Morse, A. Okishev, W. Seka, R. W. Short, M. D. Skeldon, S. Skupsky, M. Tracy, and B. Yaakobi, "Experiments on the OMEGA to Validate High-Gain, Direct-Drive Performance on the National Ignition Facility," 12th International Conference on Laser Interaction and Related Plasma Phenomena, Osaka, Japan, 24–28 April 1995.

The following presentations were made at the 8th International Precision Engineering Seminar, Compiegne, France, 15–19 May 1995:

S. D. Jacobs, D. Golini, Y. Hsu, B. E. Puchebner, D. Strafford, W. I. Kordonsky, I. V. Prokhorov, E. Fess, D. Pietrowski, and V. W. Kordonsky, "Magnetorheological Finishing: Toward Cylinders, Toroids, and Aspheric Optics."

S. D. Jacobs, "Finish Polishing of Optics with Magnetic Media" (invited).

The following presentations were made at CLEO '95, Baltimore, MD, 21–26 May 1995:

J. J. Armstrong, T. J. Kessler, L. S. Iwan, W. P. Castle, A. W. Schmid, C. Kellogg, J. Barone, and R. Stewart, "Fabrication of Large-Aperture Diffractive and Refractive UV Optical Components Using Continuous-Mask Photolithography and Replication."

T. R. Boehly, R. S. Craxton, P. A. Jaanimagi, R. L. Keck, J. H. Kelly, T. J. Kessler, R. L. Kremens, S. A. Letzring, S. J. Loucks, R. L. McCrory, S. F. B. Morse, W. Seka, S. Skupsky, J. M. Soures, M. D. Tracy, and C. P. Verdon, "Initial Performance Results from the Upgraded OMEGA Laser."

R. Boni, R. L. Keck, O. R. Lopez-Raffo, S. A. Letzring, and S. Scarantino, "The Design of an Energy Balance Measurement Diagnostic for the Upgraded OMEGA Laser System."

R. L. Keck, R. E. Bahr, R. Boni, S. A. Letzring, W. Seka, and J. M. Soures, "Initial Energy Measurements of the Upgraded OMEGA Laser."

O. A. Konoplev, Y. Fisher, and D. D. Meyerhofer, "Pedestal Suppression Technique for Chirped Pulse Amplification Laser Using Optical Pulse Cleaning and a Fast Saturable Absorber."

R. L. Kremens, D. L. Brown, J. T. Canosa, S. A. Letzring, M. Litchfield, R. G. Roides, and M. Thomas, "A Precision Electronic Timing System for the OMEGA Upgrade Inertial Fusion Laser System."

Y. Lin, T. J. Kessler, and G. N. Lawrence, "Distributed Phase Plates with Low Scattering Loss for Supergaussian Focal Plane Irradiance Profiles."

R. L. McCrory, "Direct and Indirect Laser Fusion" (invited).

A. Okishev, M. D. Skeldon, S. A. Letzring, W. R. Donaldson, K. Green, W. Seka, and L. Fuller, "Complex Multigigahertz Electrical Waveform Generation for Optical Pulse Shaping on the OMEGA Laser."

M. D. Skeldon, A. Okishev, S. A. Letzring, W. R. Donaldson, A. Babushkin, and W. Seka, "Progress on Amplification of Optically Shaped Pulses to the Multijoule Level."

Z. Xu, P. M. Fauchet, C. W. Rella, B. A. Richman, H. A. Schwettman, and G. W. Wicks, "Direct Mid-Infrared Spectroscopic Measurements of Hole Relaxation in InGaAs/AlGaAs Quantum Wells."

M. Yu, G. P. Agrawal, and C. J. McKinstrie, "Effects of Residual Dispersion in the Phase-Conjugation Fiber on Dispersion Compensation in Optical Communication Systems."

L. Zheng, D. D. Meyerhofer, and R. S. Craxton, "Polarization Rotation in Harmonic Generation of Ultra-Intense Laser Pulses."

The following presentations were made at the 25th Annual Anomalous Absorption Conference, Aspen, CO, 27 May–1 June 1995:

R. Betti, V. Goncharov, R. L. McCrory, and C. P. Verdon, "Growth Rate of the Rayleigh-Taylor Instability for Indirect-Drive ICF."

T. R. Boehly, R. S. Craxton, P. A. Jaanimagi, R. L. Keck, J. H. Kelly, T. J. Kessler, R. L. Kremens, S. A. Letzring, S. J. Loucks, R. L. McCrory, S. F. B. Morse, W. Seka, S. Skupsky, J. M. Soures, M. D. Tracy, and C. P. Verdon, "Initial Performance Results from the Upgraded OMEGA Laser."

R. S. Craxton, "Prospects for Direct- and Indirect-Drive ICF on the OMEGA Laser" (invited).

S. Cremer, S. Skupsky, C. P. Verdon, and J. A. Delettrez, "The Knock-On's Diagnostic in Laser ICF Targets Revisited."

J. Delettrez, D. K. Bradley, C. P. Verdon, and B. Yaakobi, "A Mix Model in *LILAC* for the Linear and Weakly Nonlinear Regime of the Rayleigh-Taylor Instability."

R. Epstein, J. A. Delettrez, C. P. Verdon, D. Shvarts, and B. Yaakobi, "Simulations of Time-Dependent Spectral Signatures of Fuel-Pusher Mixing in Laser-Driven Implosions."

V. Goncharov, R. Betti, R. L. McCrory, and C. P. Verdon, "The Effect of Finite Thermal Conduction on the Ablative Rayleigh-Taylor Instability."

R. Grobe and R. W. Short, "Diffractive Irradiation Patterns Inside the Plasma Corona."

T. Kolber, C. J. McKinstrie, S. J. McNaught, and C. I. Moore, "Numerical Simulations of Two-Dimensional Stimulated Raman Scattering in an Inhomogeneous Plasma."

J. S. Li, C. J. McKinstrie, C. Joshi, and K. Marsh, "Thermal Filamentation of Laser Beams."

C. J. McKinstrie and J. S. Li, "Effects of the Anti-Stokes Wave on Stimulated Brillouin Scattering."

D. D. Meyerhofer, J. P. Knauer, S. J. McNaught, and C. I. Moore, "Observation of Relativistic Quiver Effects and Multiphoton Compton Scattering during High-Intensity Laser-Electron Interactions."

J. D. Schnittman and R. S. Craxton, "Tetrahedral Hohlraums for the OMEGA Upgrade and the National Ignition Facility."

R. W. Short, "Phase-Conjugated SBS in Laser-Produced Plasmas."

A. Simon, "Parametric Excitation of Electron Bernstein Waves in Laser-Produced Plasma."

E. J. Turano, C. J. McKinstrie, and R. E. Giacone, "Two-Dimensional Stimulated Raman Scattering of Short Laser Pulses."

The following presentations were made at the 1st Annual International Conference on Solid-State Lasers for Application to Inertial Confinement Fusion (ICF), Monterey, CA, 30 May–2 June 1995:

K. Green, W. R. Donaldson, R. Sobolewski, M. D. Skeldon, W. Seka, A. Okishev, and S. A. Letzring, "Transient Microwave Bandwidth Measurements of Illuminated Silicon Switches for Optical Pulse-Shape Control of Laser-Fusion Drivers."

J. H. Kelly, T. R. Boehly, J. M. Soures, D. L. Brown, R. Boni, R. S. Craxton, R. L. Keck, T. J. Kessler, R. L. Kremens, S. A. Kumpan, S. A. Letzring, S. J. Loucks, R. L. McCrory, S. F. B. Morse, W. Seka, S. Skupsky, and C. P. Verdon, "The Activation of the Upgraded OMEGA Laser at the University of Rochester."

R. L. McCrory, J. M. Soures, C. P. Verdon, A. Babushkin, T. R. Boehly, D. K. Bradley, R. S. Craxton, J. A. Delettrez, R. Epstein, P. A. Jaanimagi, S. D. Jacobs, R. L. Keck, J. H. Kelly, T. J. Kessler, H. Kim, J. P. Knauer, R. L. Kremens, S. A. Letzring, S. J. Loucks, F. J. Marshall, P. W. McKenty, S. F. B. Morse, A. Okishev, W. Seka, R. W. Short, M. D. Skeldon, S. Skupsky, and B. Yaakobi, "OMEGA Upgrade Laser System" (invited).

M. D. Skeldon, A. Okishev, A. Babushkin, and W. Seka, "Transient Stimulated Brillouin Scattering Pulse Compression for Photoconductive Switch Activation."

S. D. Jacobs, D. Golini, Y. Hsu, B. E. Puchebner, D. Strafford, W. I. Kordonsky, I. V. Prokhorov, E. Fess, D. Pietrowski, and V. W. Kordonsky, "Magnetorheological Finishing: A Deterministic Process for Optics Manufacturing," SPIE Japan Chapter International Joint Conference on Optical Fabrication

and Testing and Applications of Optical Holography, Tokyo, Japan, 5-7 June 1995 (invited).

The following presentations were made at the Optical Interference Coatings Topical Meeting, Tucson, AZ, 5–9 June 1995:

J. F. Anzellotti, D. J. Smith, and Z. R. Chrzan, "The Improvement of Evaporated Dielectric Polarizer and Beam Splitter Coatings through the Use of Multiple Crystal Monitoring."

A. L. Rigatti, D. J. Smith, L. D. Lund, P. Glenn, and J. Glenn, "Characterization of Surface Particulate on Large Optics for Laser Fusion."

R. J. Sczupak and D. J. Smith, "A Single-Pass Laser Reflectometer: Conceptual Goals and Physical Results."

A. R. Staley and D. J. Smith, "Applications and Processes for High-Damage-Threshold Sol-Gel Coatings."

S. J. VanKerkhove and D. J. Smith, "Induced Stresses to Optical Substrates Due to High-Energy-Laser HR Thin Film Coatings."

S. Papernov, A. W. Schmid, D. J. Smith, A. Anzelotti, J. P. Knauer, P. W. McKenty, and M. D. Wittman, "Atomic Force Microscopy in Support of the Laser-Driven ICF Program," Scanning Microscopy 1995 Meeting, Houston, TX, 6–11 May 1995.

The following presentations were made at The 1995 International Workshop on Superconductivity, Maui, HI, 18–21 June 1995:

R. Adam, W. Kula, R. Sobolewski, J. M. Murduck, and C. Patiette-Hall, "Photo-Induced Changes of the Transport Properties in Y-Ba-Cu-O Step-Edge Josephson Junctions."

W. Kula, R. Adam, and R. Sobolewski, "Y-Ba-Cu-O Thin Films with a Controlled, Oxygen In-Depth Profile for Hybrid Superconducting/Semiconducting Device Applications."

W. Kula, W. Xiong, B. McIntyre, R. Sobolewski, D. B. Dukes, and A. D. Caplin, "Characterization of Y-Ba-Cu-O Thin Films Containing Regions of Different Oxygen Content and Superconducting/Semiconducting Interfaces."

The following presentations were made at the Laser Optics '95 Conference, St. Petersburg, Russia, 27 June–1 July 1995:

J. H. Kelly, T. R. Boehly, J. M. Soures, D. L. Brown, R. Boni, R. S. Craxton, R. L. Keck, T. J. Kessler, R. Kremens, S. A. Kumpan, S. A. Letzring, S. J. Loucks, R. L. McCrory, S. F. B. Morse, W. Seka, S. Skupsky, and C. P. Verdon, "The Activation of the Upgraded OMEGA Laser at the University of Rochester."

A. Okishev, M. D. Skeldon, S. A. Letzring, W. R. Donaldson, A. Babushkin, and W. Seka, "Pulse-Shaping System for 60-Beam, 30-kJ (UV) OMEGA Laser."

UNIVERSITY OF
ROCHESTER